Dynamic and Thermal Control of an Electromagnetic Formation Flight Testbed

By

Matthew D. Neave

S.B. Aerospace Engineering
Massachusetts Institute of Technology, 2003

SUBMITTED TO THE DEPARTMENT OF AERONAUTICAL AND ASTRONAUTICAL ENGINEERING IN PARTIAL FULLFILLMENT OF THE DEGREE OF

MASTER OF SCIENCE IN AERONAUTICS AND ASTRONAUTICS
AT THE
MASSACHUSETTS INSTITUTE OF TECHNOLOGY

JUNE 2005

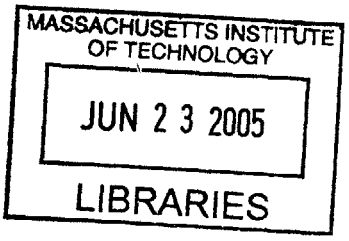

Signature of Author.....
Department of Aeronautics and Astronautics
May 20, 2005

Certified by.....
Dr. Raymond J. Sedwick
Principal Research Scientist of Aeronautics and Astronautics
Thesis Supervisor

Accepted by.....
Jaime Peraire
Professor of Aeronautics and Astronautics
Chair, Committee on Graduate Students

Dynamic and Thermal Control of an Electromagnetic Formation Flight Testbed

By

Matthew D. Neave

Submitted to the Department of Aeronautics and Astronautics
on May 20, 2005 in Partial Fulfillment of the
Requirements for the Degree of Master of Science
in Aeronautics and Astronautics

ABSTRACT

Formation flight of multiple spacecraft is an emerging method for completing complex space missions in an efficient manner. A limitation found in maintaining such formations is the need for precise control at all times. Using traditional thruster propulsion systems can be costly and life-limiting since the propellant is consumed during the mission. An alternative method for providing this relative position control is to use electromagnetic interaction between the vehicles of the formation to provide forces and torques. This method uses electricity alone, which is a renewable resource in space, to provide all actuation to control the formation.

The Space Systems Laboratory at MIT is developing this concept with a project called Electromagnetic Formation Flight (EMFF). A two-dimensional testbed has been developed to demonstrate the ability to control vehicle position and attitude using only electromagnetic forces and reaction wheels. A thorough description of this system is given, focusing on the development of its thermal and dynamic control. Innovations to the thermal system, used to cool the superconducting wire of the electromagnet, are described. All systems involved with dynamic control of an EMFF vehicle are identified and the methods used to develop control algorithms are explained. Simulations demonstrating the stability achieved by these controllers are presented and successful experimental results from the testbed are examined. Finally, the test results are used to refine the parameters used in the simulation and a more accurate dynamic model of the system is determined.

Thesis Supervisor: Dr. Raymond J. Sedwick
Title: Principal Research Scientist of Aeronautics and Astronautics

ACKNOWLEDGMENTS

The research described in this thesis was funded in part by NASA Institute for Advanced Concepts (NIAC) and NASA Jet Propulsion Laboratory (JPL). I would like to thank my advisor, Dr. Ray Sedwick, for his insight and assistance in completing this research. I am also grateful for the wonderful EMFF team that I had the privilege of working with. Special thanks to my wife, Pam, for her tireless support and encouragement. Finally, I'd like to thank Jesus Christ, the creator of magnetic fields and the sustainer of my soul, for "... in him all things hold together."

TABLE OF CONTENTS

LIST OF FIGURES

LIST OF TABLES

Chapter 1

Introduction

1.1 Motivation

Electromagnetic Formation Flight (EMFF) provides an attractive alternative to traditional satellite systems. It takes advantage of the fact that formation flight requires precision control with respect to the other spacecraft in the formation, but not of the formation as a whole. This technology provides potential for significant fuel savings, longer mission life, and increased versatility in spacecraft control. This thesis describes the Space System Laboratory's (SSL) efforts to prove the concept of EMFF in a two-dimensional environment.

1.1.1 Motivation for Formation Flight

Multiple spacecraft flown in formation provide many significant advantages to traditional, large satellites for many space missions. A formation of small space vehicles can gather more and better data than one spacecraft in orbit.[1] Multiple spacecraft can be used for space-based interferometery without the size constraints imposed by physical structures. This freedom allows for the creation of large sensor apertures for increased angular resolution. Small spacecraft also provide cost savings in manufacturing, packaging and launching. A mission executed by many small spacecraft can be easily upgraded or repaired by replacing the necessary spacecraft instead of replacing the whole system. There is also opportunity for modular design in formation flight that could lead to more effective and less expensive missions.

The space community is actively researching the topic of spacecraft formation flight. The Air Force Research Laboratory and NASA are both considering many Earth and space science missions using formation flight. One example of such a mission is the Terrestrial Planet Finder (TPF), which aims to discover Earth-like planets around Sun-like stars. One proposed architecture for TPF is an infrared interferometer made up of formation flown spacecraft.[2]

The Space Systems Laboratory at MIT has developed a formation flight testbed called SPHERES. This system is used to conduct ground testing with soccer-ball sized vehicles in two dimensions and has successfully demonstrated formation flight maneuvers including tracking and docking. Tests have also been conducted in a zero-gravity environment on NASA's KC-135 aircraft and will be conducted on the International Space Station in the near future.[3]

1.1.2 Motivation for Electromagnetic Actuation

Although formations of spacecraft have many advantages, one challenge is maintaining precise control over each element in the array. Many optical applications require controlling individual vehicle positions with very small error. Using traditional thrusters, this level of precision could use large amounts of fuel as mission life increases. Since formations of spacecraft rely on relative positions of their elements, savings could be made by using interaction forces between the vehicles. One option is to use electrostatic forces. By building up charge on the various vehicles, attraction and repulsion forces can be created. However, a more attractive alternative is to use magnetic forces. Two magnetic dipoles are able to produce shear forces in addition to attraction and repulsion forces. This phenomenon is depicted below, in Figure 1.1.

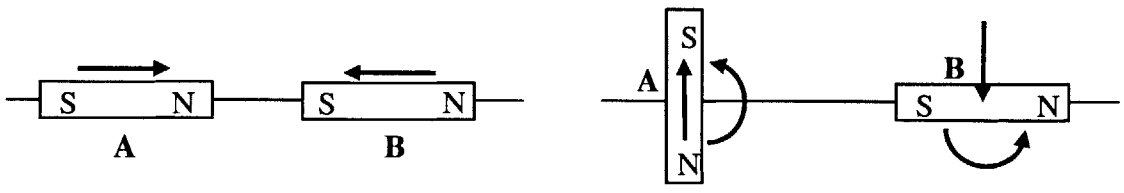

Figure 1.1: Forces and torques between two dipoles

Electromagnets provide the ability to vary the strength of the magnetic field and introduce a control input. The magnetic interaction of electromagnets made by coils of wire with current flowing through them can be approximated, at large distances as compared to their size, as the interaction of magnetic dipoles through their centers. Multiple magnetic dipoles through one point add to give a new resultant dipole. With three orthogonal coils of wire each, the effective dipole through the center of the vehicle can be steered, and two vehicles can move to any position with appropriate control. However, when magnetic dipoles are not aligned they introduce torques on each other. These torques can be counteracted by reaction wheels. With the addition of three orthogonal reaction wheels, all relative degrees of freedom can be controlled. The limitation of electromagnetic control is that it can only control relative position of the spacecraft in an array and cannot control the position of the center of mass of the formation.

The largest advantage of electromagnetic control over propellant-based thruster control is that it does not rely on a consumable resource. Electromagnetic forces can be produced with the correct use of electric current, which can be harvested from the sun's energy using solar panels. This allows the spacecraft's lifetime to be limited by its hardware life instead of by the amount of fuel on board. Another disadvantage of control with thrusters is that propellant can cause damage. Many optical experiments can be degraded by propellant contaminating sensitive instruments or by thruster plumes obstructing the view of the spacecraft. Docking procedures are also safer without the possibility of firing a thruster at another spacecraft.

The use of electromagnetism to introduce significant forces that are able to control spacecraft is enabled by superconducting technology. Conventional wire is not able to carry the current necessary to produce magnetic moments capable of controlling spacecraft motion to a reasonable level. However, high temperature superconducting (HTS) wire has been developed that is capable of carrying 140 times the current of copper wires of the same size. HTS wire must be cooled to temperatures below 115K to be superconductive.[4] In this state the wire has zero resistance, which increases the

efficiency of this method. The challenge in implementing superconducting electromagnetism is cooling the wire coils to superconducting levels. Immersion in liquid nitrogen is effective in accomplishing this task and further investigation is being conducted into other methods of regulating cryogenic wire temperatures.

1.2 Testbed Description

A testbed has been developed at the MIT Space Systems Lab (SSL) to investigate the feasibility of the Electromagnetic Formation Flight (EMFF) concept. Two vehicles have been built to test control algorithms using electromagnetic forces. Tests are conducted on a flat surface using pressurized CO_2 to float the vehicles, simulating a frictionless environment in two dimensions and giving each vehicle three degrees of freedom. The vehicles each have two orthogonal coils of superconducting wire and a vertical axis reaction wheel to provide full control authority. A liquid nitrogen containment system maintains a superconducting temperature for the wire. An infrared and ultra-sound metrology system provides position measurements and computation is executed by a C6701 processor.

1.3 Thesis Overview

This thesis will describe the work done to implement reliable thermal and dynamic control of an Electromagnetic Formation Flight testbed. The next chapter will focus on the previous work done to develop EMFF. First we will look at the original design for thermal control that was pursued by a class at MIT. We will review the requirements used to come to this initial design, describe the architecture of the system, and investigate problems encountered. We will also give a description of the initial avionics design and reasons for its upgrade. We will next discuss the dynamic modeling and control work of Dr. Laila Elias. Finally, we will see results of implementing control both in simulation and using hardware experiments.

The third chapter will outline the new design for thermal control. First, we will describe the process of selecting materials for the system. Next, we will take a detailed look at the design of the thermal system. A simple, but innovative approach to pressure regulation

that is used for thermal control will also be explained. We will also look at problems that were encountered in the re-design of the thermal system and how they were fixed.

The fourth chapter will describe the EMFF system and its subsystems. These systems include the avionics, which handles all information and is used to program control algorithms, the metrology system, which uses information from multiple sensors to find the state of the vehicle at all times, and the actuators, which provide the forces and torques to manipulate the vehicles. The physical properties of the vehicle, which are used to develop control for the system, will also be identified.

In the fifth chapter we will describe the magnetic field models used to simulate the vehicle's dynamics and develop proper control. Next, various methods of control that are relevant to the EMFF system will be explained and the simulation developed to evaluate these controllers will presented. We will also look at the simulations behavior in rejecting disturbances and following trajectories.

The control algorithms developed in Chapter 5 were implemented on the EMFF testbed to prove the ability to control an actual vehicle using electromagnetic forces. The results from these tests will be presented and compared to the predicted results from the simulation. A method will be introduced that was used to match the simulation model with what was observed in tests. A new model will be presented and its simulation predictions will be compared to the experimental results. Finally, we will conclude the thesis with a summary and highlight the contributions of this research.

Chapter 2

Previous Work

2.1 Thermal Control

Superconducting wire is an enabling technology for the EMFF concept. Conventional copper wire cannot carry the required current to create magnetic fields capable of controlling a formation of satellites and would put far too great a demand on the power subsystem to make it advantageous. However, along with this technology comes the challenge of keeping the wire at temperatures needed to enable superconducting. This section describes the design pursued by the MIT Department of Aeronautics and Astronautics Junior/Senior Capstone Design Class (CDIO) to provide this thermal control.

2.1.1 Requirements

The superconducting wire, purchased from American Superconductor, must be kept below 115K to exhibit superconductive characteristics. Below this temperature, the wire has zero resistance, but as temperature drops the amount of current that can be carried by the wire increases.[4] If a cryogenic fluid is used to provide cooling of the coils, the wire must be completely submerged by that fluid. The cooling fluid must also be insulated from the environment, which is at a much higher temperature. The containment system for the superconducting coils must fulfill these requirements.

The class also set specifications for what kind of maneuvers the system should be able to execute. To show its potential for use with interferometers, a formation of two EMFF vehicles must be able to spin-up to a rate of one rotation per minute. This requirement

directly feeds the sizing of the superconducting coils because they must be large enough to provide a magnetic moment capable of accelerating the formation to the required rate.

A final requirement of the thermal control for EMFF is that it be completely self-contained on each vehicle. It must be structurally connected to the rest of the vehicle and not require connection to any other components while testing. Although the thermal control system can be refilled between tests, the system must be designed to be completely autonomous during tests. Tests are to run for twenty minutes without the vehicles needing additional cooling fluid.

2.1.2 Previous Design Description

The CDIO class designed a superconducting wire and thermal control system to meet the requirements outlined for the EMFF system. A detailed description can be found in the design appendix created by the class.[5] To provide the forces and torques necessary to spin-up a two-vehicle array to one rotation per minute, each electromagnet must provide a maximum magnetic moment of $\mu = 4723$ [A-m^2]. Magnetic moment of a coil of current-carrying wire is the product of the number of turns of wire, the amount of current, and the area enclosed by the coil, or $\mu = nIA$. The superconducting wire used can carry up to 100 amps without reaching its critical current, which leaves the number of turns and size of the coil to be chosen. The team decided on coils of diameter close to one meter.

The outside coil was designed to have a diameter of .835 meters and 99 turns of wire. The inside coil had a diameter of .670 meters and 120 turns of wire. Each superconducting coil was made up of three coils in series. This design allowed the entire coil cross-section to take a more geometrically efficient, square shape. Kapton insulation was applied between the turns of the wire to prevent any electric shorting across the wires. The dimensions of the coils are depicted in Figure 2.1.

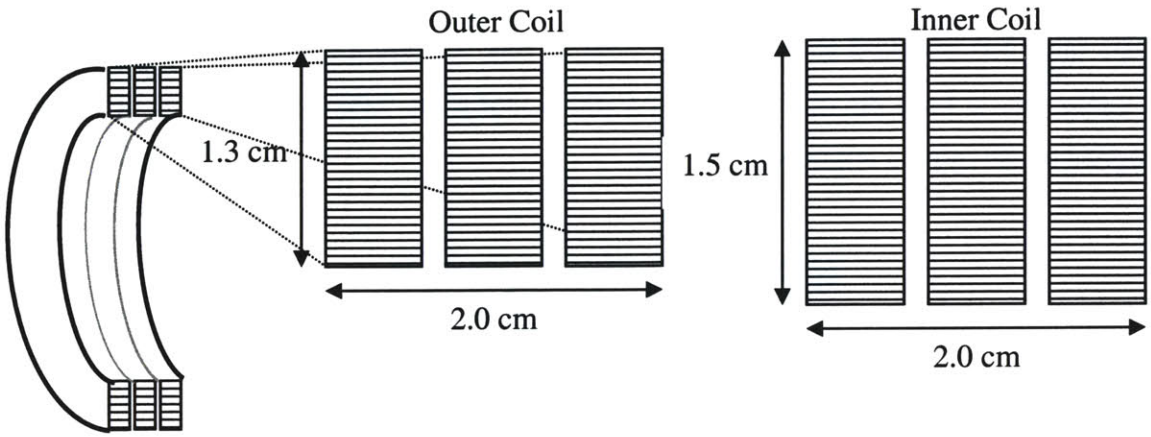

Figure 2.1: Original Coil Size[5]

The casing for the superconducting coils was made of STYROFOAM, extruded polystyrene insulation, milled in a toroidal shape. This casing provided the structure to hold the coils and liquid nitrogen as well as the insulation to isolate it from the environment. Spacers were cut into the foam to hold the superconducting wire and allow room for liquid nitrogen to pass freely. The containment system was made so the entire smaller container fit inside the larger one (Figure 2.4). The foam pieces were attached to each other using epoxy, and fiberglass tape was wrapped around the containers and sealed with epoxy to provide leak-proofing.

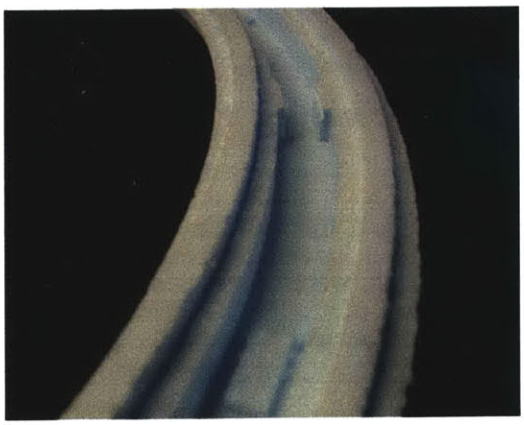

Figure 2.2: Milled Foam Container[5]

To provide a sufficient test duration, a tank was designed to supply the system with liquid nitrogen as it boiled off. A simple gravity-fed system was implemented. The 12-inch square tank was installed above the two coils so that the liquid nitrogen would fall into the containers to keep the coils submerged and at cryogenic temperatures. The tank was designed to provide 10 minutes of cooling.

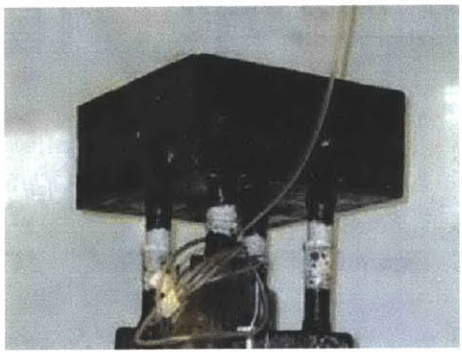

Figure 2.3: Original LN2 Tank[5]

2.1.3 Problems with Initial Design

Thermal cycling from repeated cooling to cryogenic temperatures and returning to room temperature created cracks in the foam containment system. Fiberglass tape and epoxy were used to seal these leaks. It was thought that after multiple thermal cycles, the stress in the foam would be relieved and no additional cracks would form. However, with nearly every filling of the containment system, new leaks would form. After most tests, the leaks would need to be marked and then the vehicle would have to warm to room temperature and dry out completely. The next day fiberglass tape and epoxy would be wrapped around the leaking area and the vehicle would be ready for tests in the next couple days. Several successful tests were conducted under these circumstances, but the constant leaks were disruptive to the test schedule. Frequent re-patching also added weight to the vehicle.

The LN2 tank placement also presented problems. Filling the containment system was difficult since the top of the tank was not visible or reachable from ground level. Pipes were used to pump the liquid nitrogen to the top of the vehicles and into the tank. The tank also made the EMFF vehicle top-heavy and added unnecessary height to the vehicle. The containment system also lacked secure mounts to the vehicle base permitting the coils to lean to the side.

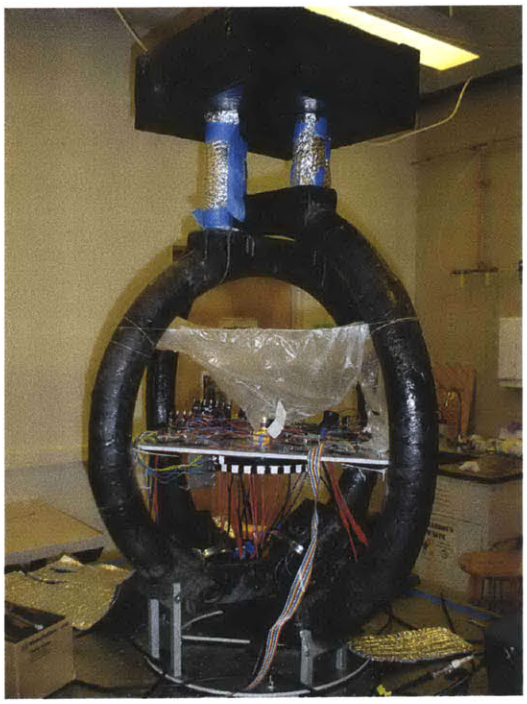

Figure 2.4: Original EMFF Vehicle

2.2 Avionics

The CDIO class also identified the interfaces of the avionics/electronics subsystem needed for the EMFF vehicle. "The primary role of the avionics subsystem is to integrate all hardware and software of the system".[5] The core of the initial avionics was the Tattletale Model 8 computer. The Tattletale Model 8 computer (TT8), with Motorola CPU (Central Processing Unit) and TPU (Time Processing Unit) was chosen because it was thought to suit the project processing needs and it was readily available in the Space Systems Laboratory. The computer interfaced directly with four other pieces of

hardware: The Metrology computer, the voltage regulator, the Communications board, and a series of mosfets used for power amplification purposes. This hardware conceptual layout is shown below, in Figure 2.5.

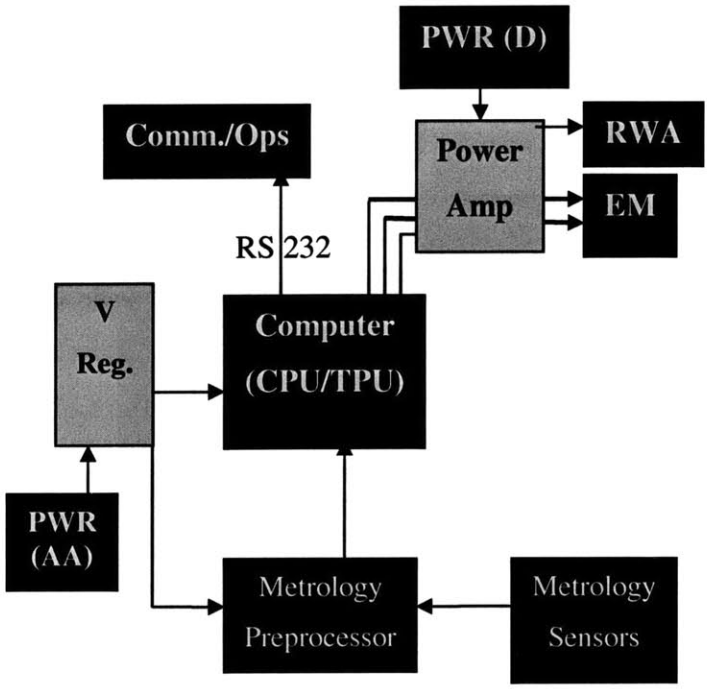

Figure 2.5 Avionics Data-flow Diagram[5]

The Metrology computer was an additional Tattletale Model 8 computer. The avionics subsystem was designed to allow the sending of the vehicle's state information using Primary Vehicle Array (PVA) updates through a serial channel from the Metrology TT8 to the main Avionics TT8 computer. The power subsystem was designed to supply steady 5V power from the AA batteries to the Tattletale computers and the Avionics board. The communications/operations hardware was designed to send and receive all data being transmitted and received from the immediate vehicle system to the avionics TT8 and vice versa. The communications board interfaced with the avionics TT8 through a serial RS232 cable connection.

Although the initial avionics design allowed for functionality of the testbed, there were limitations that were found. Since the electronics were integrated by hand, some connections were not reliable and signals were occasionally corrupted, resulting in bad

data. The integration of wireless communications was also found to be quite difficult and would have required extensive work to complete. Successful tests were completed using tethers between the vehicles and ground station for communications, but the tethers introduced external forces that disturbed the dynamics of the system. Finally, there was not enough computational speed in the TT8 to perform complex control algorithms.

2.3 Dynamics and Control

Previous work has been completed to model the dynamics of the EMFF system. Dr. Laila Elias conducted research in the Space Systems Lab to develop a full 3-dimensional model of EMFF using dipole approximations for the interactions between electromagnets. She also analyzed the stability and controllability of such a system, as well as performing relevant experiments to improve confidence in the technology of EMFF.[6]

2.3.1 Three-Dimensional Dynamics Model

The interaction forces and torques between current carrying coils of wire can be approximated by treating the coil as a magnetic dipole through the coil center along its axis. This approximation is valid at separation distances much larger than the coil's radius. The dipole has an effective magnetic moment equal to the product of the number of turns of wire, the amount of current, and the area enclosed by the coil, or $\mu = nIA$. The forces and torques created from the interaction of magnetic dipoles depend nonlinearly on their positions. Other nonlinear dynamics occur in the EMFF system due to the effects of gyroscopic stiffening from spinning reaction wheels. These inherent nonlinearities require a nonlinear model to describe the dynamics.

Nonlinear equations of motion were developed for a multi-spacecraft array using EMFF technology. The geometry of such an array was defined with multiple coordinate systems and a standardized notation was introduced. The dynamic model included the nonlinear dynamics of the reaction wheels and also accounted for external disturbances to the system. The general form of these equations is valuable because it can be adapted to describe any more specific situation. By eliminating degrees of freedom and only using

two vehicles, the dynamic model can be changed to describe the two-dimensional testbed that is functioning in the lab.

In Elias' thesis, the general dynamic model was then simplified to two vehicles. The system dynamics were linearized about a nominal trajectory, a steady-state spin. This trajectory is significant because it is a maneuver needed by interferometer configurations. In a steady-state spin, the spacecraft need a constant attractive force to counter the centrifugal accelerations pulling them apart. Additional control is needed to reject disturbances and remain on the nominal trajectory.

The linearized dynamics of the nominal trajectory were then analyzed for stability. They were found to be unstable with a pole in the right half plane. It was found that instability grew with increased nominal spin rate. However, controllability analysis shows that the system is stabilizable. It was shown that an EMFF system with three orthogonal coils and three reaction wheels is fully controllable in three dimensions. A two dimensional system is also fully controllable with two orthogonal coils and one reaction wheel. This validates the design of the two dimensional EMFF testbed.

An optimal controller was then designed to stabilize the linearized dynamics of the nominal trajectory. A linear quadratic regulator was developed to minimize a weighted sum of state errors and control use. A large part of this work was in determining appropriate penalties for state errors and actuator use.

The optimal controller was used in a closed-loop simulation to evaluate its effectiveness. This simulation used the nonlinear equations of motion describing the system to model its behavior. State feedback from this model was used by the LQR controller to calculate the appropriate control to apply to the nonlinear model, completing the control loop. The simulations used various Matlab differential equation solvers.

Closed-loop control simulations tested the system's ability to arrive at the nominal trajectory after starting at off-nominal initial conditions. Analyzing the behavior of the

free response to these non-zero conditions gives similar information as investigating the system's response to disturbances. The results of these simulations showed that the EMFF system is indeed stabilizable. The controller was able to bring the behavior of the system to its nominal trajectory with feasible magnitudes of control. The simulations also showed that a limiting factor in controlling the EMFF system could be the torque capabilities of the reaction wheel motor.

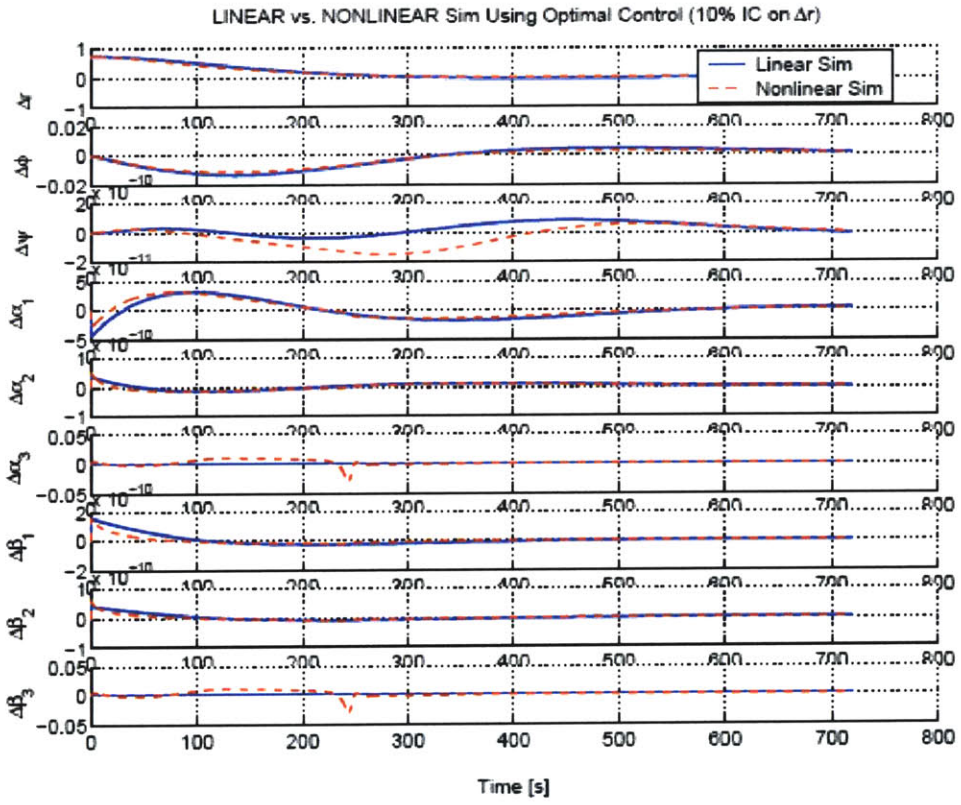

Figure 2.6: Dynamic Simulation, 10% Initial Condition on Δr: State Responses[6]

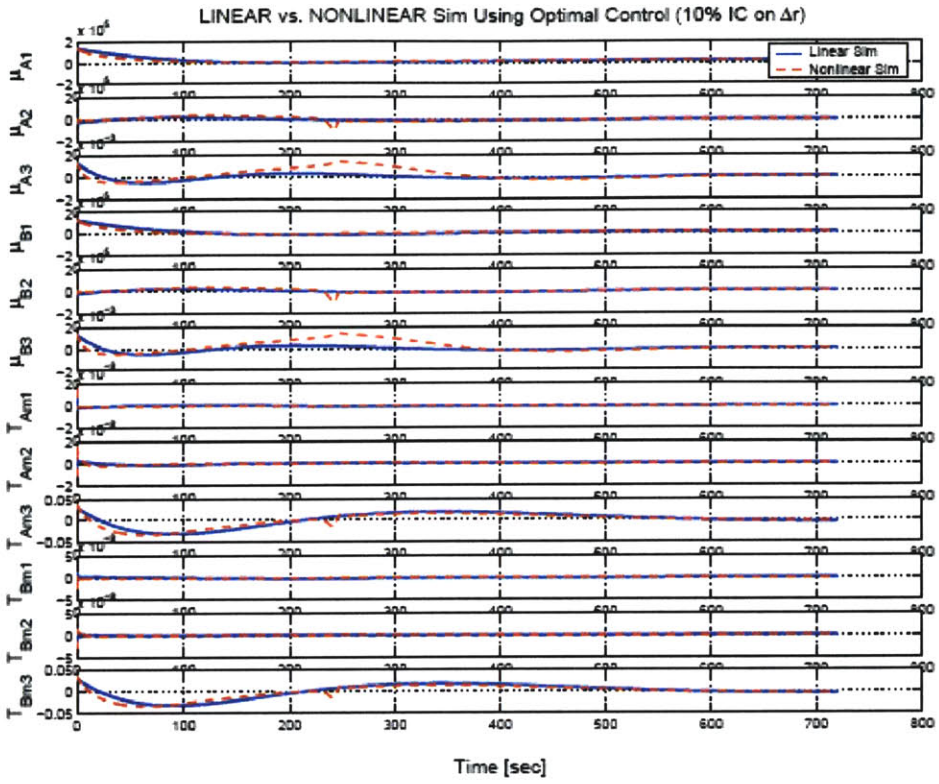

Figure 2.7: Dynamic Simulation, 10% Initial Condition on Δr: Actuator Signals[6]

2.3.2 Hardware Experiments

Previous work has also been done in experimentally testing the feasibility of electromagnetic control. Elias' thesis describes experiments conducted in a one-dimensional environment using an airtrack as well as initial work on the two-dimensional EMFF testbed. This work has provided positive results encouraging further investigation into the effectiveness of this technology.

The linear airtrack consisted of an electromagnet fixed to one end of a track and a permanent magnet that was free to slide on the track. The current flowing through the electromagnet could be adjusted in real time to provide control authority. Compressed air was fed through small holes in the track to enable the permanent magnet to slide freely. An ultrasonic displacement sensor was used to determine the position of the sliding magnet in real time. This feedback information was used to develop controllers to

regulate the position of the free magnet. Experiments were conducted in both a stable and an unstable configuration.

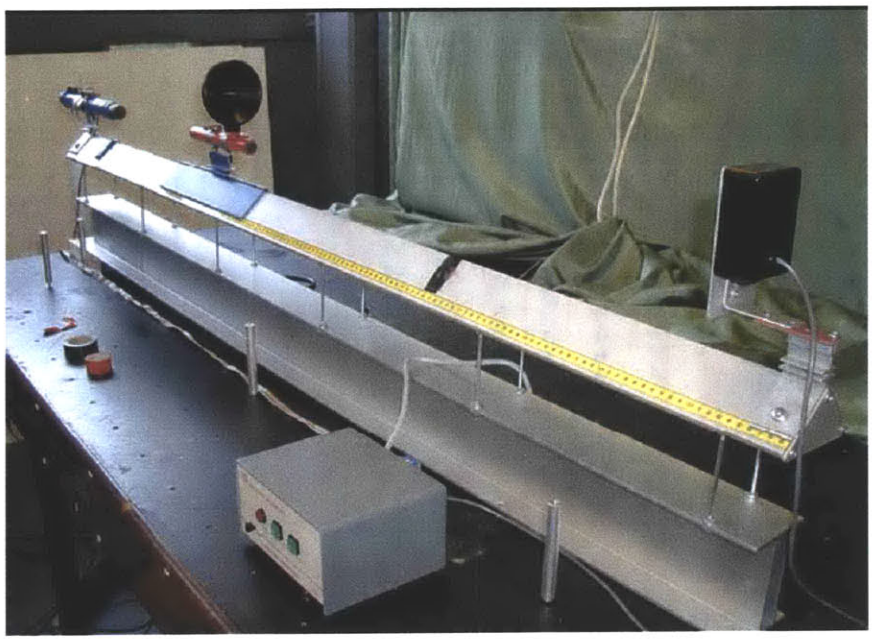

Figure 2.8: Linear Airtrack[6]

The air track was configured to be stable by slightly tilting the track so the free magnet tended to slide towards the electromagnet. Although stable, the step response of this system was highly oscillatory. By implementing a feedback controller, the behavior was significantly improved.

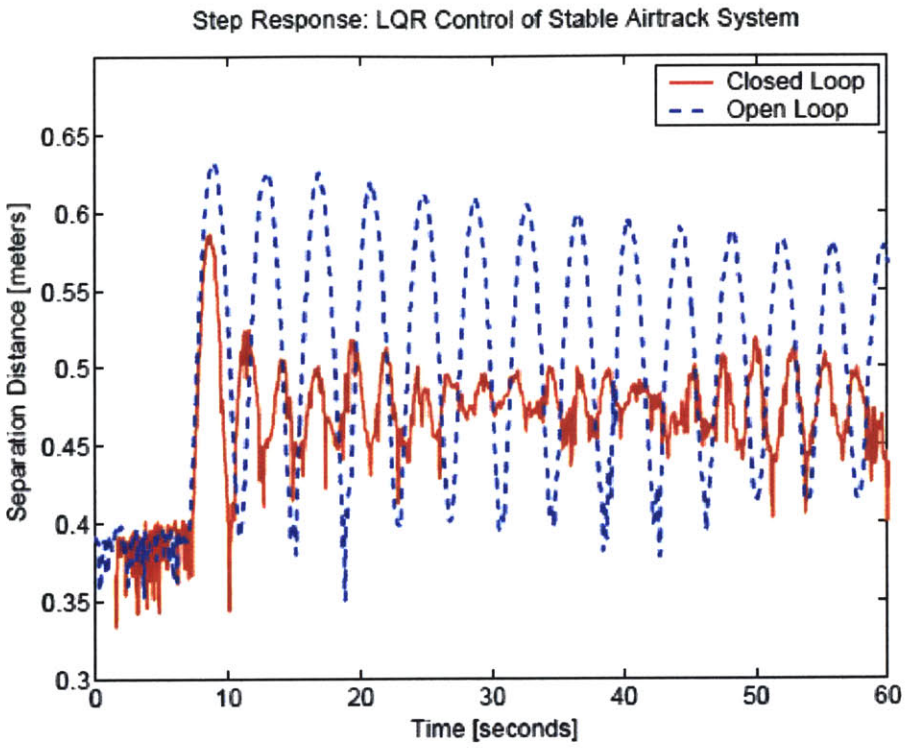

Figure 2.9: Open- and Closed-Loop Step Responses of Stable Airtrack[6]

Experiments were also conducted with the track tilted so the sliding magnet fell away from the electromagnet. This unstable configuration of the air track is of more interest because its dynamics are very similar to those of a steady-state spin of a spacecraft array. In both situations a constant force is required to oppose the forces pulling the two magnets apart. If the force between them is slightly too large, the magnets will crash into each other and if it is slightly too small they will drift apart. For this reason, feedback control is needed to maintain constant separation distance. Experimental results showed that this unstable system can be controlled.

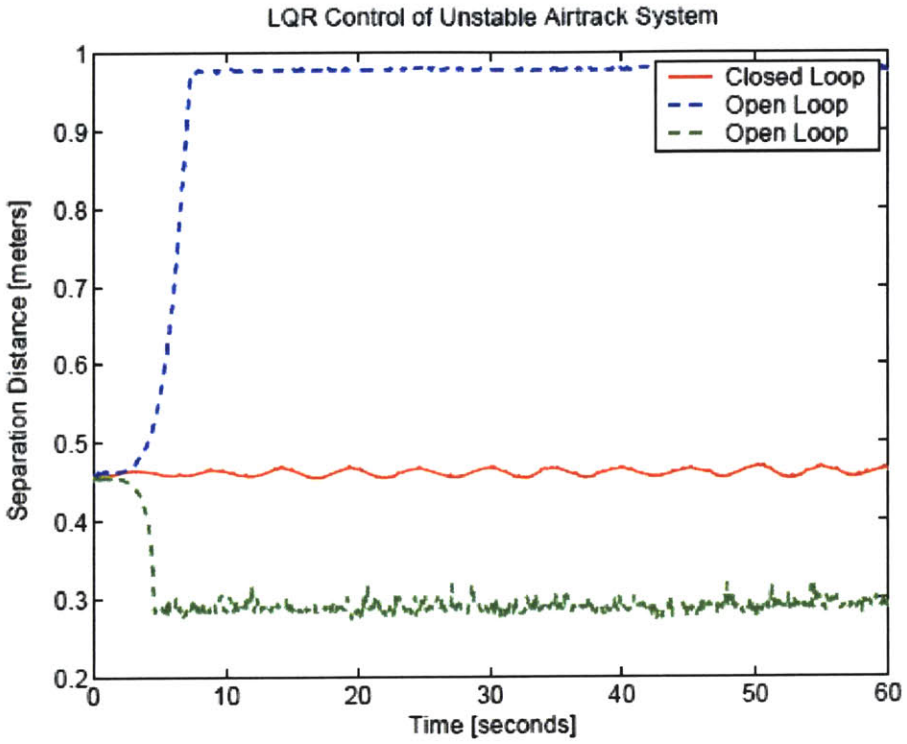

Figure 2.10: Open- and Closed-Loop Responses of Unstable Airtrack[6]

Successful results on the linear air track imply that the proposed control of two and three dimensional systems are also likely possible. At the time of Elias' thesis the two-dimensional EMFF testbed was not fully functional because the metrology system was not working. However, reaction wheel control was successfully implemented to regulate the attitude of the spacecraft. The results are shown below.

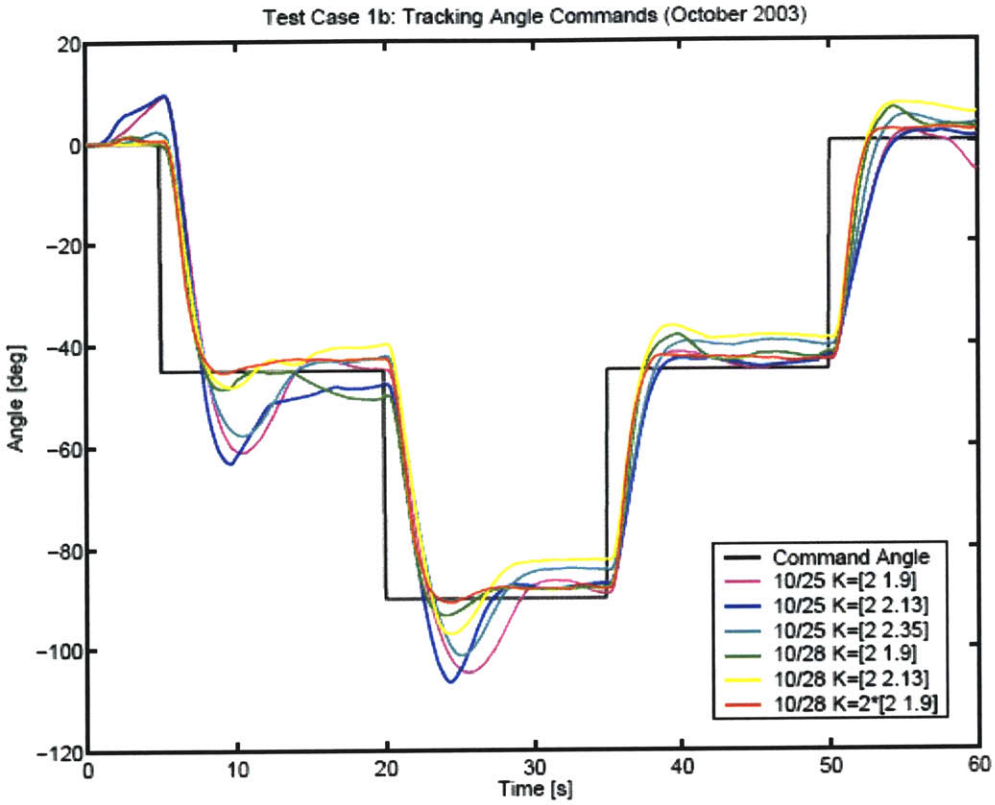

Figure 2.11: Angle-Tracking Results Using One Vehicle on the Planar Testbed[6]

Chapter 3

New Thermal Design

The problems faced with the original thermal design could not be permanently fixed with repair, so a new design was needed. The new thermal system needed to be leak-proof, lightweight, and professional in appearance. This section outlines the process of designing this new thermal control system for the EMFF testbed vehicles.

3.1 Material Selection

Styrofoam has many qualities that made it attractive as a material for the first containment system. It is easy to shape with a lathe or by carving with a knife. It is also a good insulator, which helps isolate the liquid nitrogen from the environment, and it is not magnetic. Foam is also very light-weight, yet strong enough to hold the wire coils. Unfortunately, it also cracks easily so it could not handle the thermal deformations caused by cryogenic temperatures.

Most of these characteristics were looked for in a new material. Plastic seemed like a good option, but it could not handle the thermal extremes induced by liquid nitrogen. Next, metals were investigated. Since the containment system is in the shape of a torus, the metal would need to be ductile. We chose to test copper because it is not magnetic, it can be soldered at its joints, and as a sheet it can be bent easily.

A system made of copper would depend on strong, leak-proof solder joints. A test piece of copper soldered into a ring was procured and inspected for strength. It was thermally cycled from room temperature to liquid nitrogen temperatures multiple times. The joint

showed no sign of cracking and maintained its strength. A box channel made of thin copper sheet was made to test for rigidity and strength. It was found that in a box formation, very thin copper could be used to make a strong structure.

Figure 3.1: Copper Test Pieces

Another requirement of the containment system is imposed by the superconducting wire. The wire can delaminate at temperatures above 300° F and be destroyed. When installing the superconducting coil, the containment system would have to be soldered closed at high temperatures. A test was set up to determine the internal temperature of a channel as a lid was soldered onto it. Temperature readings were recorded throughout the soldering process, both with and without air flowing through the channel. Tests were conducted using both a torch to solder and a soldering iron. The soldering iron kept the internal temperatures lower and was easier to use. Tests using a soldering iron reached a maximum temperature of 110° F with airflow cooling, and 180° F without. These results show that a soldering iron can be used to heat the copper container without damaging the superconductor inside.

Figure 3.2: Solder Heat Test

3.2 Design Description

A toroid shaped container was designed for the EMFF vehicles using copper. The containers were designed to provide ¼" of space between the walls and the coil to allow the liquid nitrogen to pass freely around the coil. The container was designed as a rectangular channel with a flange at the top as shown below. The lid is flat and can be placed on top and soldered to seal the container.

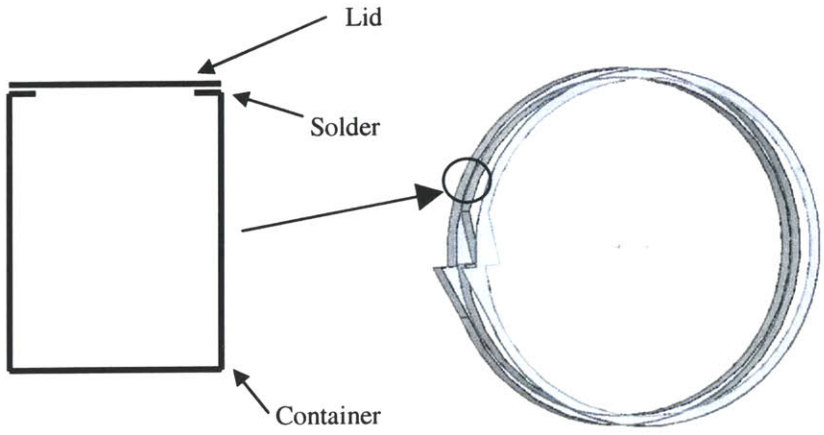

Figure 3.3: New Container Design

The large coil set the size for the first container. It was designed to fit the three coils of superconductor inside with approximately ¼" of space around each coil. The superconducting wire is 0.24 inches wide. The large container holds three coils of wire each with a diameter of 32.87 inches and 99 turns. Since the copper containers are much smaller than the previous foam containers, the inner coil was re-wrapped to a larger diameter. It now is 30.62 inches in diameter and each coil has 103 turns. The container designs are shown below. The lid is the same size and shape as the container, but only a single sheet of copper.

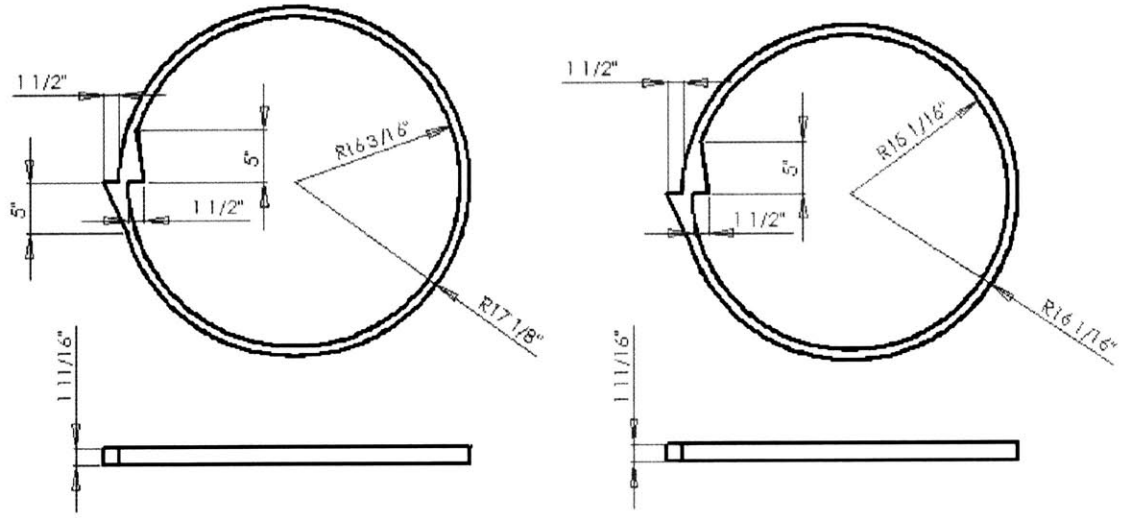

Figure 3.4: Container Dimensions

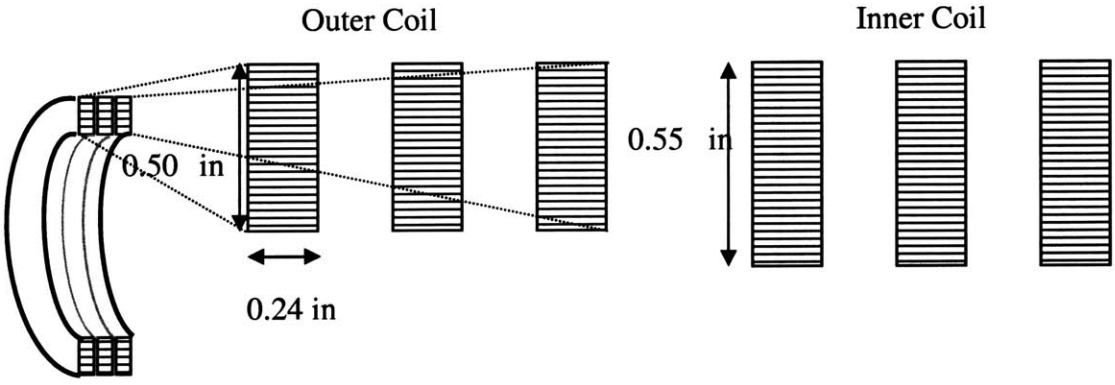

Figure 3.5: New Coil Dimensions

The coil is held away from the wall of the container with spacers made of fiberglass. The spacers are cut by a water jet so the coil of wire fits into them snuggly. The fiberglass provides electrical insulation between the wires and the container, as well as thermal insulation from the copper walls. The spacers are attached to the coil on alternating sides with additional spacers at the bottom and top of the container.

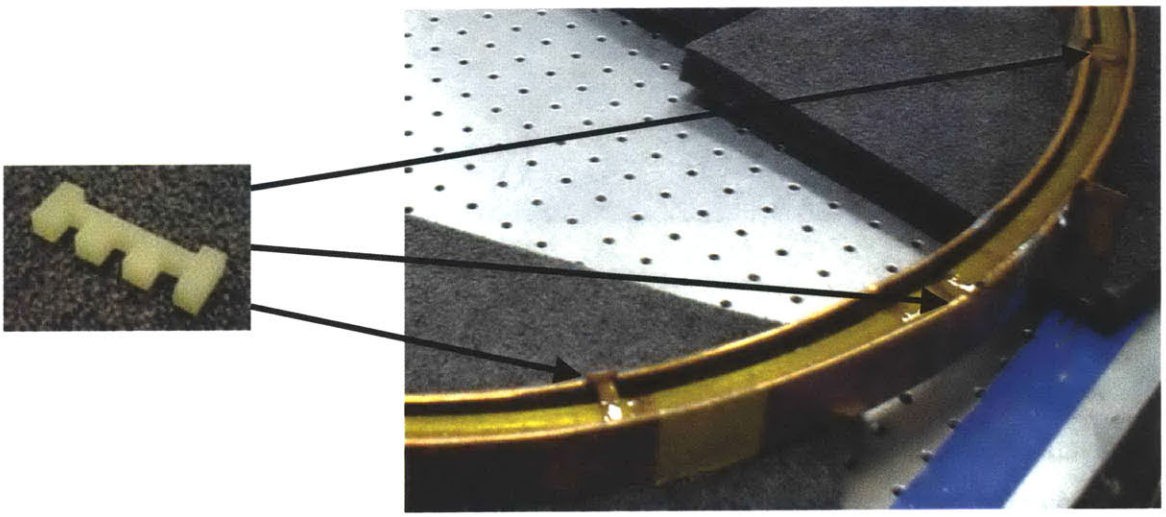

Figure 3.6: Fiberglass Spacers

To keep the container leak-proof, a special electrical connection had to be designed for passing current to the coils. The containers were designed with protruding connection ports to make room for attaching the superconducting wire to the connector. A 3/16 inch diameter copper rod is used to pass current through the container. Teflon shrink tubing surrounds the copper rod to provide electrical insulation from the container. The connector uses a pipe compression fitting to create a leak-tight seal around the conductor.

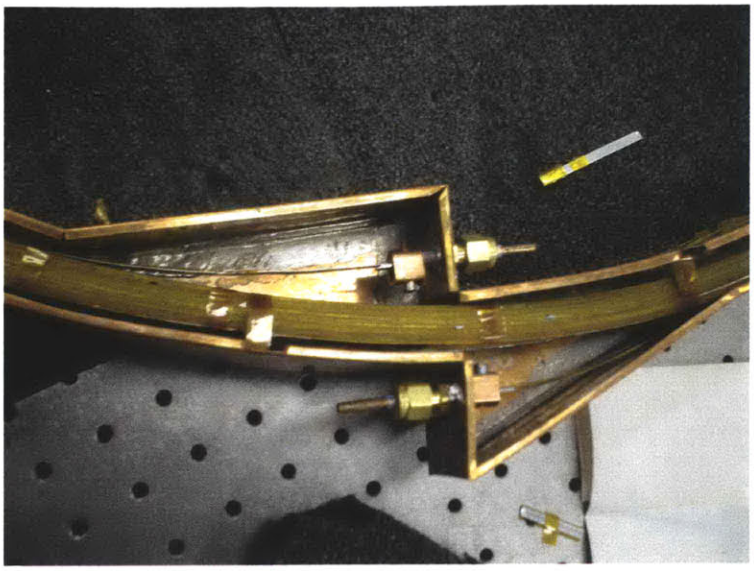

Figure 3.7: Wire Connection Port

An advantage of using copper for the containment system is that connecting pieces can be easily soldered onto the container. Tabs were soldered to the top and bottom of each container for alignment. The bottom tabs were fastened to a mount on the vehicle base. The mounts are made of fiberglass screwed into aluminum blocks. They provide a secure, rigid connection for the container.

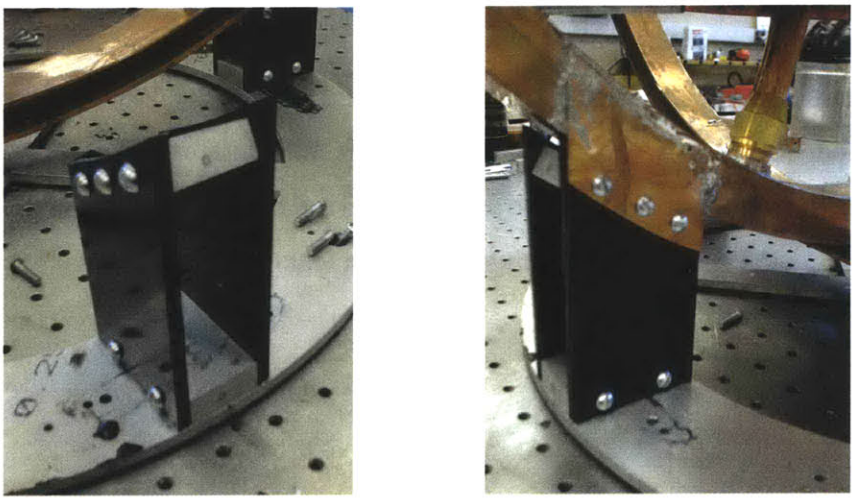

Figure 3.8: Container Mounts

Reflective aluminum foil insulation was chosen to wrap around the containment system and provide a barrier between the warm air of the laboratory and the cryogenic temperatures of the containment system. The insulation is constructed of two layers of thin aluminum sheet separated by a 5/16 inch dead air space. This type of insulation was chosen because it can be easily wrapped around the containment system without greatly increasing the size of the vehicle.

3.3 Pressurized System

In order to make the vehicles less top-heavy and more compact, it was decided to put the liquid nitrogen tank inside the coils. Placing the tank below the top of the containers necessitates a pressurized cooling system. One option would be to constantly pump liquid nitrogen through the containers. This would require an expensive and heavy cryogenic pump. Instead, a simple concept, resembling a pressure cooker, was investigated.

3.3.1 Concept Evaluation

To fill the containers with liquid nitrogen there must be enough pressure in the tank to lift the liquid nitrogen to the top of the containers. A constant pressure will cause a constant height difference between the liquid surfaces in the tank and in the containers. The difference in pressure at the two surfaces determines the vertical distance between them, which depends on the density of the fluid.

$$\Delta P = \rho g h \tag{3.1}$$

As liquid nitrogen sits in the tank it evaporates slowly. As it changes from liquid to gas it expands to 694 times its volume. This expansion creates a high pressure inside the tank. To maintain a constant pressure, a valve is needed that releases excess gas when the internal pressure is higher than desired. Pressure is a ratio of force to area, so by creating a pressure regulator with a weight sitting on a hole with the correct weight to area ratio, the desired pressure can be regulated. When the pressure inside the tank reaches the ratio

of the weight to the area of the opening, the weight will lift and allow gas to escape until the pressure falls to the desired level. This concept is illustrated below.

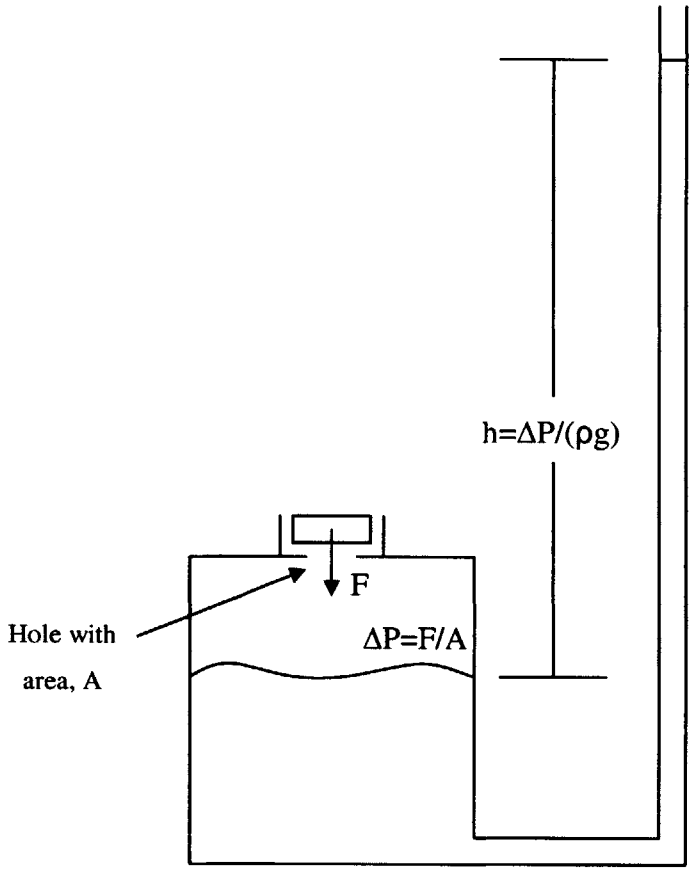

Figure 3.9: Pressure Regulator Concept

A simple version of this kind of valve is a ball sitting on a hole in the tank. The pressure will build in the tank until it reaches the ratio of the ball's weight to the area of the hole. Then the ball will lift and release pressure until the ball can fall back onto the hole. An experiment was set up to test this concept. A clear tube was connected to the bottom of a tank and then hung vertically next to it. The tank was filled with water and the level in the tank was the same as the level in the clear tube. A metal ball was placed on top of a fitting in the top of the tank and pressurized air was fed into the top of the tank. After the pressure built up inside the tank, the ball lifted and floated on the escaping air. The water level in the tube was recorded. This procedure was repeated for balls of various masses.

Figure 3.10: Pressure Regulator Test with Water

Two metal balls were used for testing, one weighing 1.6 ounces and the other 0.3 ounces. Two fittings, of different diameters, were used for the experiments. The larger fitting had a diameter of 0.455 inches and an area of 0.1626 in^2. The opening on the smaller fitting was 0.359 inches across with an area of 0.1012 in^2. Shown below are the pressures that were expected to be regulated by placing the ball on the fitting and pressurizing the tank. The pressures are shown in both pounds per square inch (psi) and in the height in inches that they should lift a column of water. The tests gave results very close to the calculated values. The maximum error was three percent. This showed that the proposed method of pressure regulation was promising.

Table 3.1: Water Test Results

		Large Ball	Small Ball
Large Hole	Calculated	0.615 psi 17.0 in. H2O	0.115 psi 3.2 in. H2O
	Measured	16.5 in. H2O	3.1 in. H2O
	Error	2.9%	3.1%
Small Hole	Calculated	0.988 psi 27.6 in. H2O	0.185 psi 5.1 in. H2O
	Measured	26.9 in. H2O	5.0 in. H2O
	Error	2.5%	2.3%

This experimental setup was adapted to allow for testing with liquid nitrogen. Instead of a plastic tube, a large copper pipe was attached to the bottom of the tank. A Styrofoam float with a wooden rod was used to check the level of liquid nitrogen in the pipe. The same experiment that was done with water was not as successful with liquid nitrogen. When a ball was placed on a fitting the level of LN2 would quickly rise to a level slightly higher than what was expected. Then the level would slowly increase much higher than expected. It was thought that the nitrogen gas could not escape quickly enough through the fitting, so a new regulator was built. A weight was designed to slide freely in a large pipe, but to completely cover a hole of slightly smaller diameter. A plug with a hole of this diameter was soldered into a pipe to create the regulator shown below. The larger hole allowed gas to escape more freely and allowed better pressure regulation.

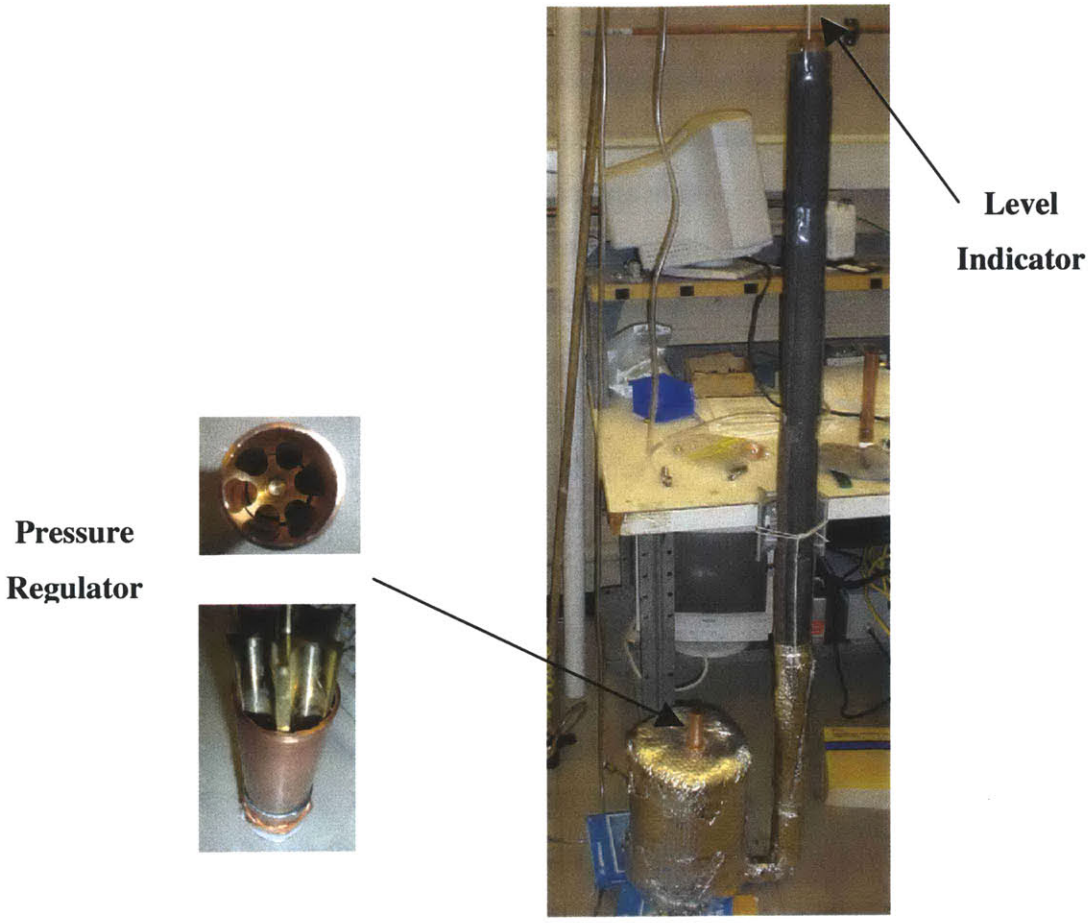

Figure 3.11: Pressure Regulator Test with Liquid Nitrogen

Small rings were added to the weight shown above to investigate the liquid level response to increasing weight. The initial weight was 2.3 oz and each ring added 0.2 ounces. The tests showed that the level of liquid nitrogen could be controlled reliably to within 5% error using a regulator similar to the one used in our experiment.

Table 3.2: Experimental Results with Liquid Nitrogen

Weight	2.3 oz	2.5 oz	2.7 oz
Calculated	25.0 in. LN2	27.3 in. LN2	29.4 in. LN2
Actual Average	24.2 in. LN2	26.0 in. LN2	29.3 in. LN2
% Error	3.2	4.8	0.34

3.3.2 Implementation

The first element in the pressure regulation system is the tank. The tank was designed to hold twice the amount of liquid required to fill the containment system. The volume of the tank was set at 550 in^3. With appropriate insulation this should provide twenty minutes of cooling. It was also decided that the tank would be a cylinder because of the ease of manufacturing this shape. Using a constant volume, the size and placement of the tank were optimized, constrained by the size of the smaller container. The goal was to find the optimal geometry and placement of the tank between the extremes of a tall, narrow column in the center of the vehicle and a short, wide disc in the middle of the vehicle.

Since electronics, the reaction wheel, and other components needed to fit in the middle of the vehicle, the tank was designed to sit as low as possible inside the containers. The tank width was constrained to fit inside the smaller ring, with margin for the insulation that would be applied. Below is the optimization that yielded the most efficient placement and size of the tank. As the position of the bottom of the tank is lowered (shown as an increasing d), the calculated location for the top of the tank also decreases to a point. After this point, the tank starts to look like a tall cylinder, which would take up most of the space inside the vehicle.

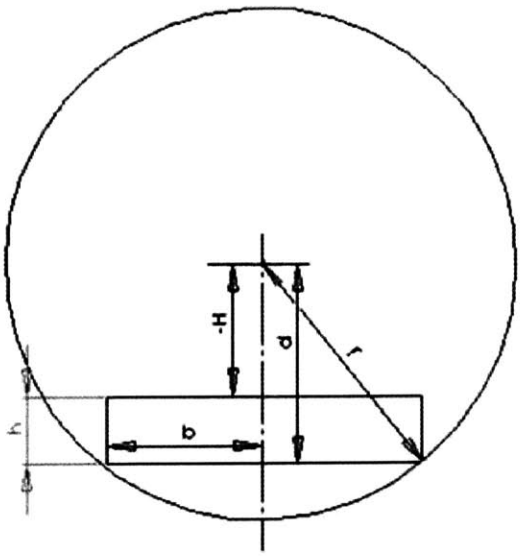

$$V = \pi b^2 h \qquad h = \frac{V}{\pi b^2}$$

$$b = \sqrt{r^2 - d^2} \qquad H = h - d$$

Figure 3.12: Tank Placement Assumptions

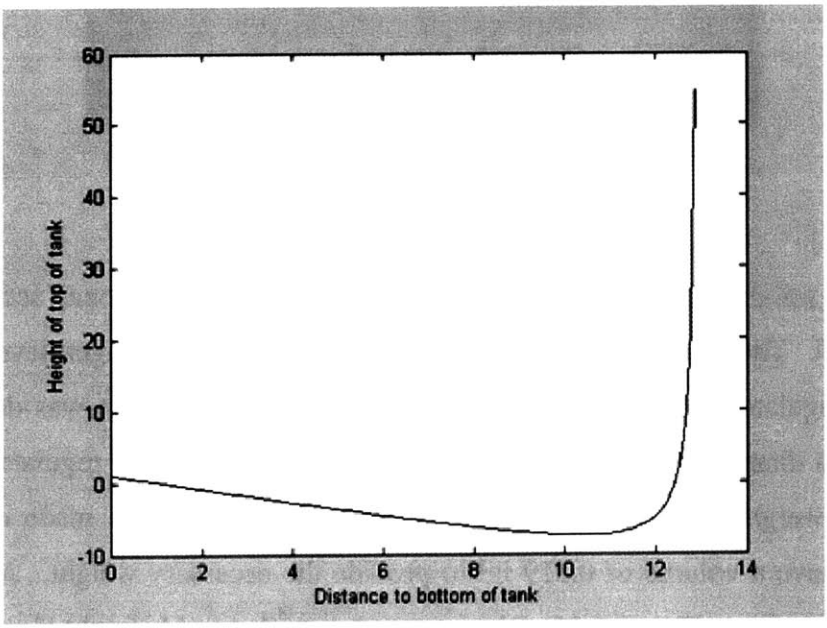

Figure 3.13: Tank Placement Optimization

The top of the tank is lowest when the distance to the bottom of the tank from the center of the vehicle is 10.4 inches. This yields a tank that has a diameter of 15.56 inches and a height of 2.88 inches. This puts the bottom of the tank 28 inches below the top of the

large container. The pressure regulator must be designed to lift the liquid nitrogen level in the containers to at least 28 inches.

The tank was made by bending a strip of copper into a cylinder shape and soldering it to a circle of copper on the top and bottom. It was attached to the containers with pipes that connected to compression fittings. This allows the tank to be easily removed from the containers and maintains the system's modularity.

Figure 3.14: Tank Connection Pipes

The specific weight of liquid nitrogen, or density times gravitational acceleration, is 0.02919 lb/in^3. Therefore 0.82 psi is needed to raise the liquid nitrogen level 28 inches. A pressure regulator similar to the one used in proving the concept was designed. Its opening has a diameter of 0.50 inches and an area of 0.20 in^2. To regulate the desired pressure the weight needed to be 2.568 ounces. The weight was made of brass and designed to have a volume of 0.519 in^3 to provide the necessary weight. A drawing of the weight is shown in Figure 3.15. Rings were also made to add weight if needed.

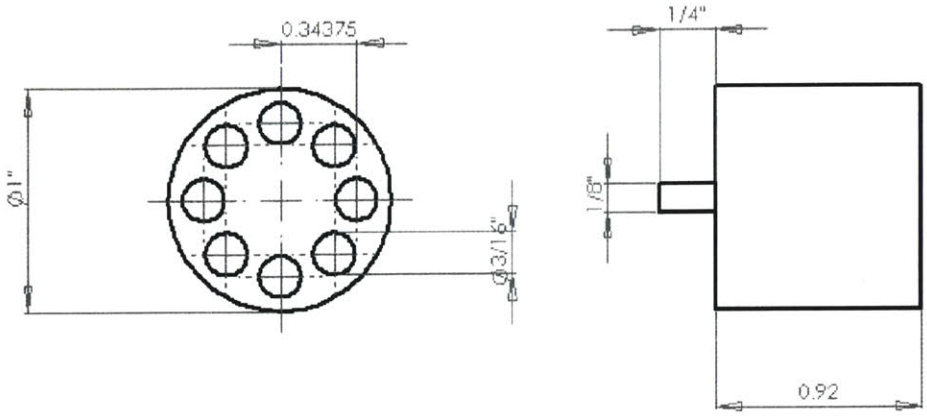

Figure 3.15: Pressure Regulator Weight

3.4 Design Evolution

The thermal control upgrade has shown improved performance over the original design. However, the design has evolved as problems were identified and fixed. Below is the first version of the new design. This section outlines the flaws discovered and the work done to resolve them.

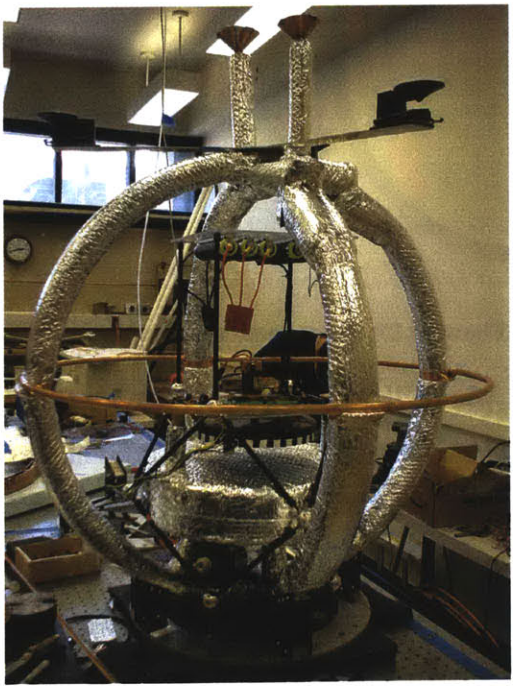

Figure 3.16: Initial EMFF Redesign

3.4.1 Superconductor Burn

It was found that the placement of the connectors to the superconducting coils was not ideal. In two coils, the superconductor broke from apparent burning near the point of connection. It is thought that an air bubble formed around the superconductor next to the connector, allowing it to increase temperature, and causing it to cease superconducting. In review, it was seen that the geometry of the connection port could lend well to this phenomenon.

The point of the connection port was slightly higher than the vent for escaping nitrogen gas. It is likely that gas was caught in this area and caused the superconducting wire to heat up past superconducting temperatures. The wire is separated from the rest of the coil at this point so it does not have the thermal mass to keep it from heating up quickly. As the wire became highly resistive, large amounts of current were continued to be driven into it. Too much power was dissipated, $P = I^2R$, and the wire burnt through.

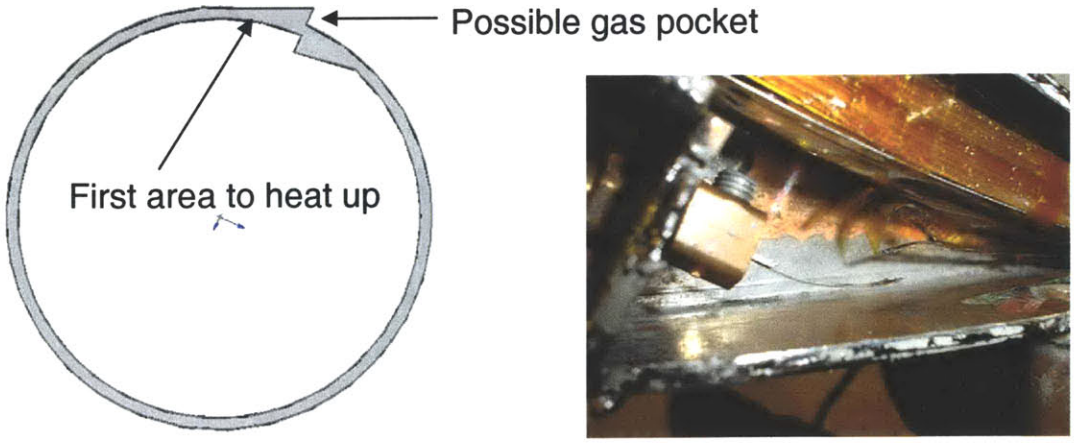

Figure 3.17: Superconductor Burn

To ensure that the area where the superconducting wire exits the container stayed completely covered in liquid nitrogen, the connection point was lowered. This required the wall of the container to be cut at a lower point, bent outwards and patched with additional copper. As another safeguard, a temperature sensor, called a resistance temperature detector (RTD), was installed in the liquid nitrogen vent in each vehicle.

When the liquid nitrogen level falls below the sensor, a light turns red and current is not applied to the superconductors.

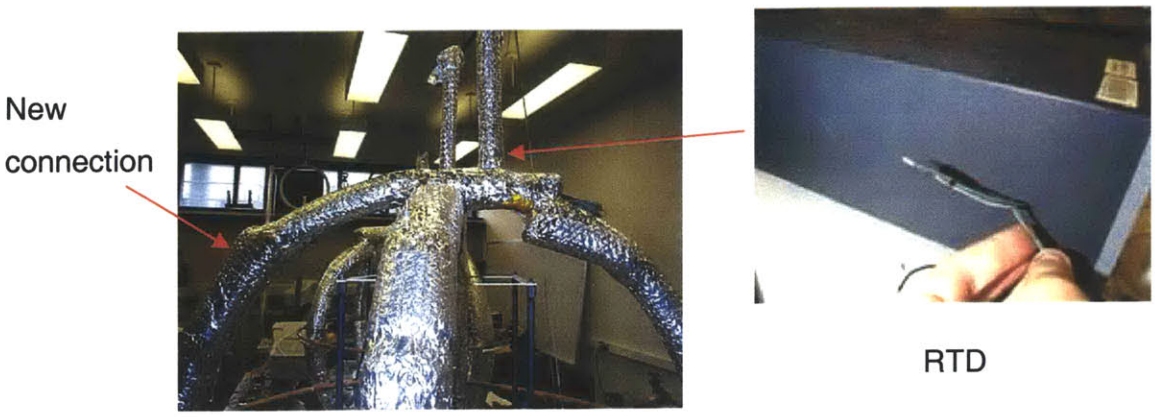

Figure 3.18: Superconductor Burn Fixes

3.4.2 Oscillating Pressure Regulator

The weight used in the pressure regulator valve was able to regulate the liquid nitrogen level accurately, but exhibited an oscillating behavior. The liquid level in the containers would reach the vent pipes and then slowly rise until the pressure regulator would let out a sudden burst of nitrogen gas and the level would fall below the top of the container and return again. The holes in the weight did not allow the gas to escape quickly enough until the pressure rose enough to lift the weight significantly. The sides of the weight were milled out to allow gas to escape. The behavior with the modified weight was much smoother, with a constant release of nitrogen to maintain the correct pressure.

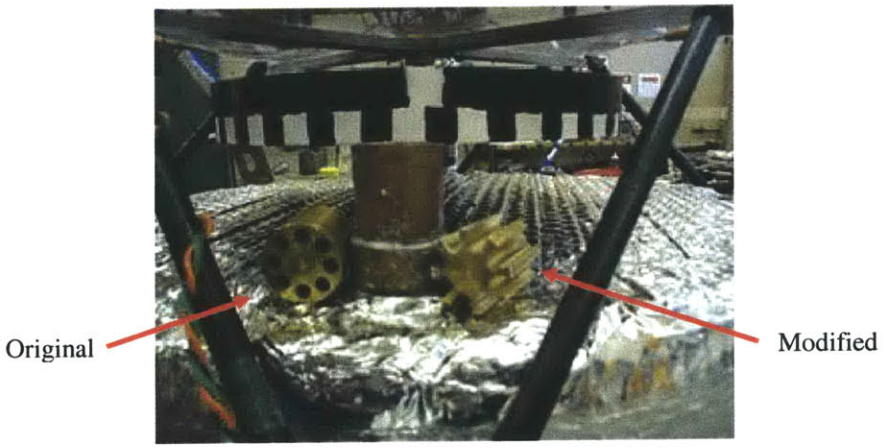

Figure 3.19: Pressure Regulator Fix

Chapter 4

System ID and Description

The EMFF system is driven by a computer that reads inputs from multiple sensors, processes metrology measurements, handles communications procedures, calculates control outputs, and sends commands to actuators. This section will describe the components of this system and the physical properties of an EMFF vehicle.

4.1 Electronics description

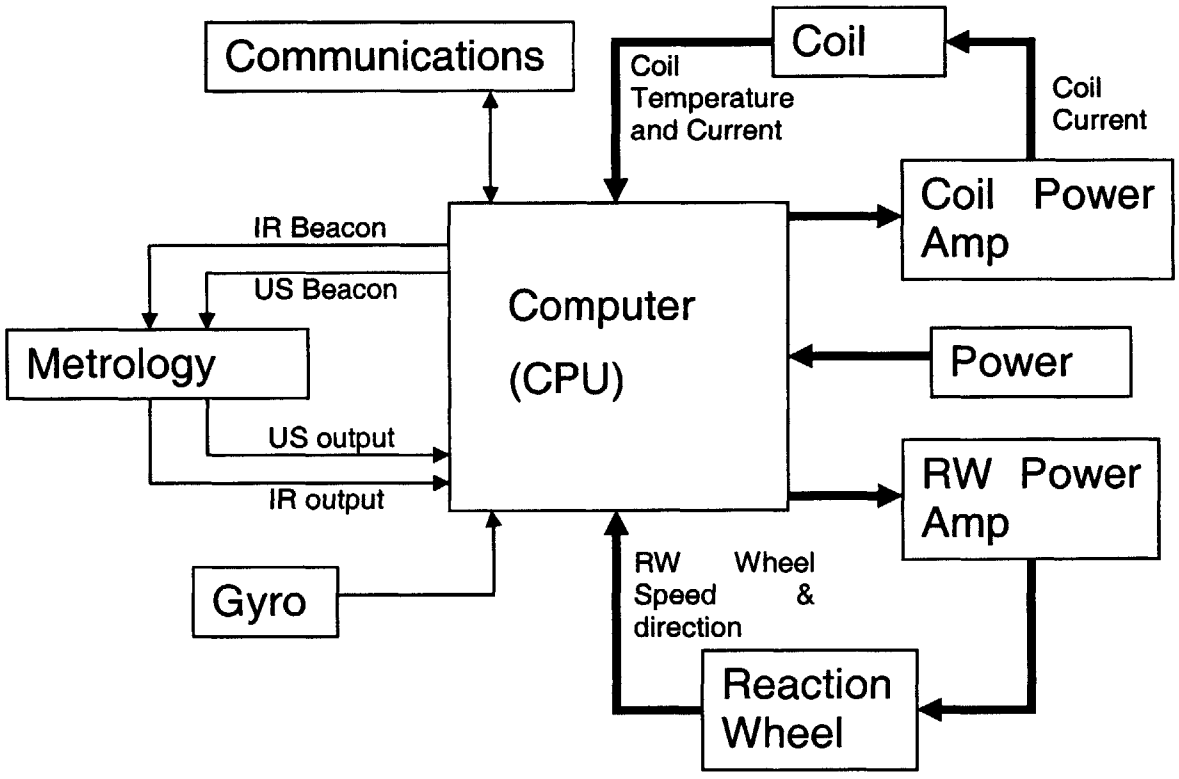

Figure 4.1: EMFF Data Flow Diagram

4.1.1 Computer

A Texas Instruments C6701 DSP runs the flight software at a rate of 167 MHz. Table 1.1 shows the key characteristics of the computer.

Table 4.1: Processor Details[3]

DSP	No.	1
Speed	Mhz	167
FLOPS (Peak)	G	1
RAM	MB	16
Cache	kB	512
ROM - available	kB	224
ComPorts	No.	6
CommPort Rate	Mbps	20
Power	W	7

Figure 4.2: DSP Processor[3]

Analog sensors are sampled and digitized by an FPGA at 12-bit resolution. It has a speed of 25 MHz. The computer reads inputs from infrared and ultrasound receivers for metrology. It also senses information about the system from the reaction wheel tachometer, a gyroscope, a temperature sensor, and a current sensor. The computer also handles communications outputs and inputs. It outputs commands to the actuators, which are the reaction wheel and electromagnetic coils. The computer also outputs commands to the metrology system to signal it to send IR and US pulses.

4.1.2 Communications

The communications subsystem uses a radio frequency channel to transmit data. An RFM DR2000 is used to provide 57.6 kbps of raw data, or an effective 18 kbps. We send packets of 32 bytes at a rate of 70 packets of useful data per second. The

communications structure is time-division multiple access so the vehicles and laptop take turns communicating while the others listen. The communications period is split into windows for each vehicle to transmit.

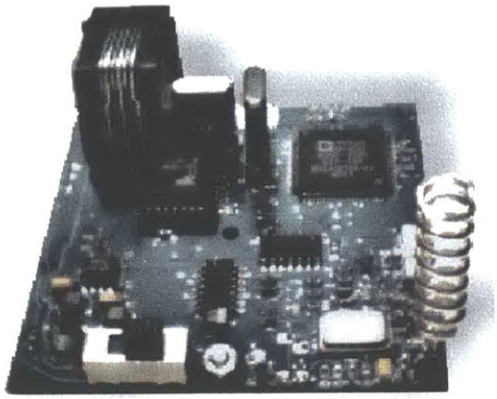

Figure 4.3: RFM DR2000[3]

4.1.3 Power

Each EMFF vehicle is equipped with two sets of eight AA batteries to power the avionics. A voltage regulator maintains supplies of 5 volts and 12 volts. Most avionics chips use the five volt supply, and the twelve volt supply is used by a circuit that displays information about the coils. Each electromagnetic coil has 3 D-cell batteries to provide the current used to create the electromagnet. The reaction wheel uses a separate supply of 7 D-cell batteries.

4.1.4 Metrology

The relative positions of the vehicles are determined real-time with a metrology system that uses infrared and ultrasound pulses. The metrology loop is initialized with a command for an infrared pulse that is sent by the FPGA. The infrared pulse is transmitted and then immediately received by all vehicles to synchronize their timing. Next the vehicles take turns sending ultrasound pulses. The receiving vehicle knows when the transmitting vehicle sent its US pulse and counts the time until it receives the pulse. Since the speed of sound is known, this time count can be converted to a distance.

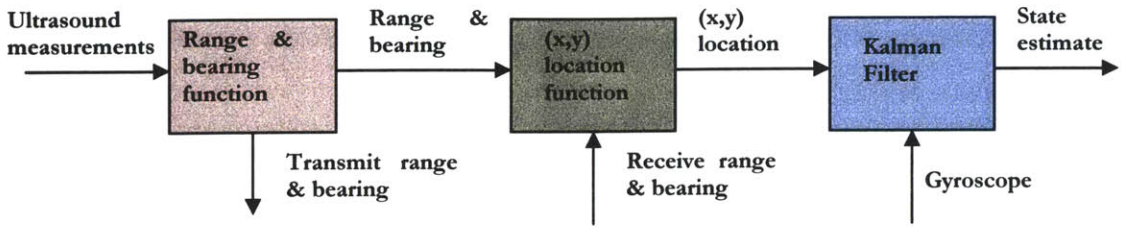

Figure 4.4: Metrology Procedure

Each vehicle has three ultrasound receivers positioned at points of an equilateral triangle. At all times, at least the two closest receivers will detect the ultrasound pulse from the other vehicle. With the two distance measurements from these receivers, the distance between the vehicles can be calculated, along with the receiving vehicle's bearing angle with respect to the line between them. This range and bearing information can be shared between the two vehicles to get full information on their relative positions.

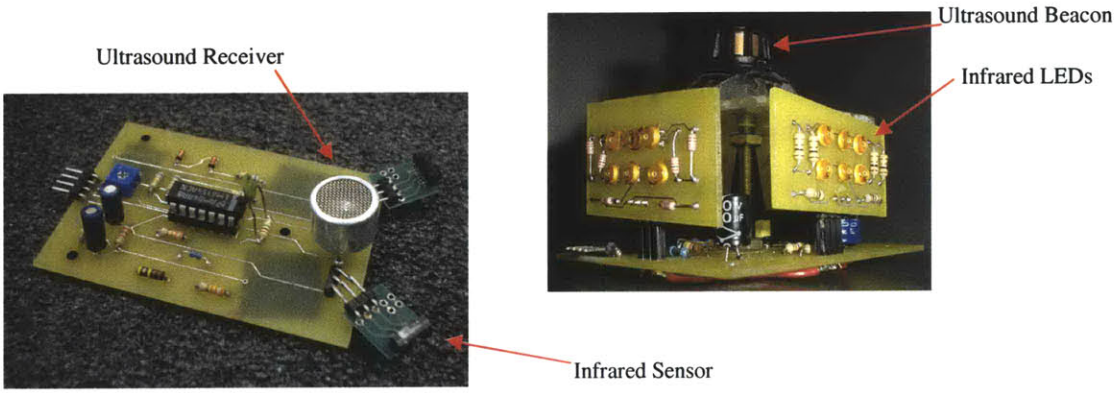

Figure 4.5: Metrology Hardware

4.1.5 Sensors

A gyroscope is used to provide angular rate data about the vertical spin axis of the vehicle. It gives an analog input to the processor between zero and five volts. It has a very high bandwidth of 300 Hz so it can be used to give high rate updates for attitude determination.

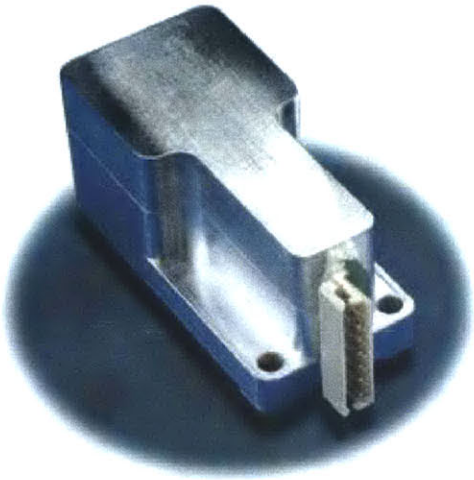

Figure 4.6: Gyroscope[3]

A tachometer is used to read the speed of the reaction wheel. Optical sensors are used to count alternating black and white stripes on the reaction wheel. One sensor tells the frequency of stripes, which can be used to determine speed. Another sensor determines the direction of the reaction wheel. A circuit changes the digital frequency into an analog input corresponding to the correct speed of the reaction wheel.

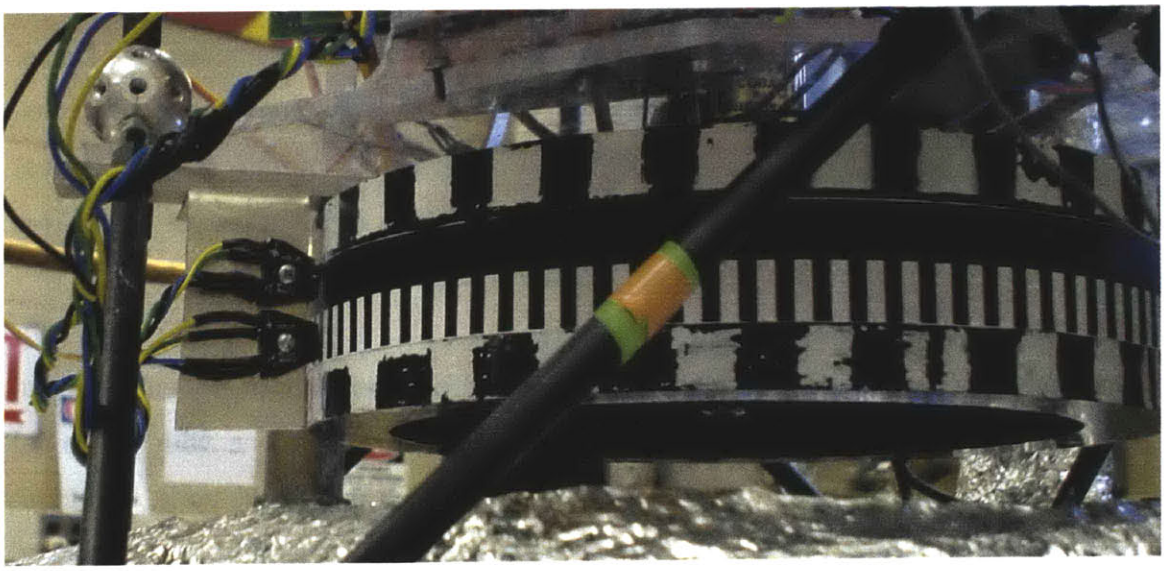

Figure 4.7: Reaction Wheel Tachometer Sensors

A resistance temperature detector (RTD) is located in the vent tube at the top of the containers holding the coils. The resistance in this detector decreases when it is

submerged in liquid nitrogen. A circuit uses this phenomenon to flip a switch when the RTD leaves liquid nitrogen. This information is displayed and it can be used to automatically turn off power to the electromagnets. A current sensor measures the amount of current being pumped through each coil. This information is displayed on an LCD screen and can be read by the processor.

Figure 4.8: Resistance Temperature Detector

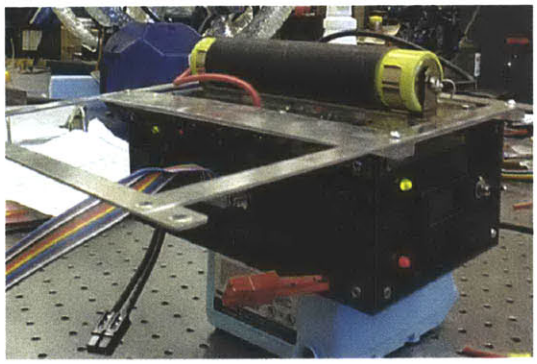

Figure 4.9: Current and Temperature Display

4.1.6 Actuation

The electromagnetic coils are powered by a separate set of 3 D-cell batteries and a controller was developed to regulate the current in the coils. A detailed description of the method used to command current in the coils can be found in the masters thesis of Daniel Kwon.[7] The current controller is commanded by an analog input from zero to five volts. An input of 2.5 volts corresponds to a command of zero amps of current. The current regulated varies linearly with supplied voltage with a slope of 50 amps per volt. This means that a five volt input yields 125 amps and 0 volts gives -125 amps in the coil.

Siglab was used to approximate a transfer function from commanded current to actual current for the superconducting coil. The characterization was done with the initial avionics system, which used a pulse modulated signal to command the coils. A circuit with a resistor and capacitor would average the PWM signal and cause a small delay. The RC circuit gave the system a pole at 7 Hz. We found that the coil itself has a pole at 0.9 Hz (5.65 rad/s). The experimental and fitted bode plots corresponding to the transfer function for the system are shown below.

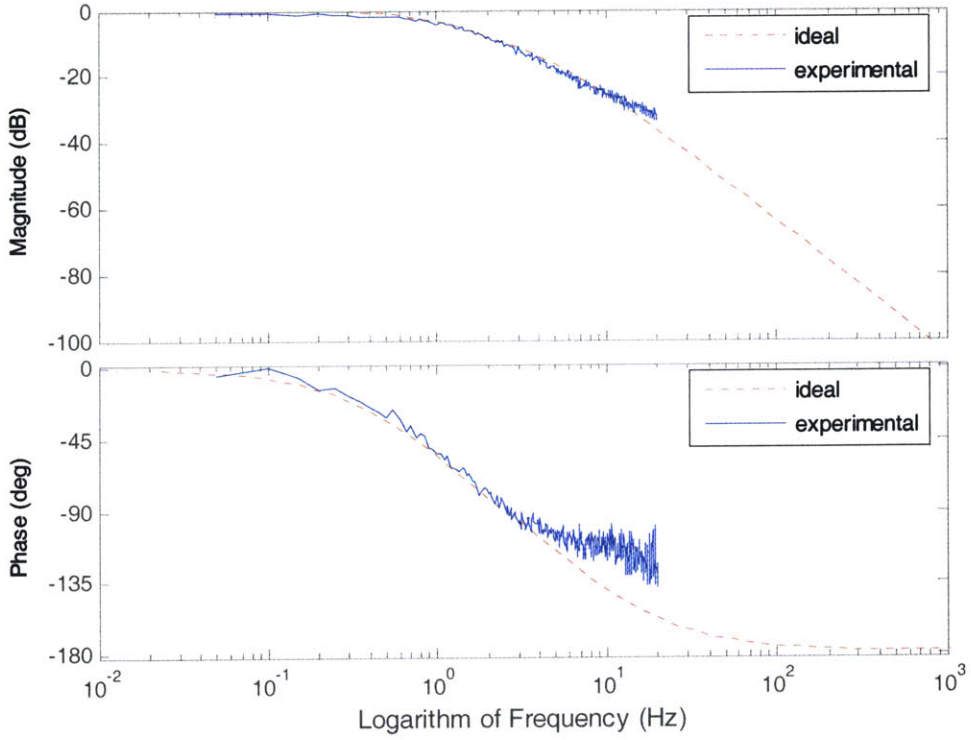

Figure 4.10: Electromagnetic Coil Behavior

The reaction wheel was made of urethane because a metal wheel would introduce complexities with eddy currents generated in the magnetic field. It was designed to have an angular momentum capacity half of what is required for a system of two vehicles to spin-up. A detailed description is given in the class' design document.[5] The final design of the wheel is shown in cross-section in Figure 4.11.

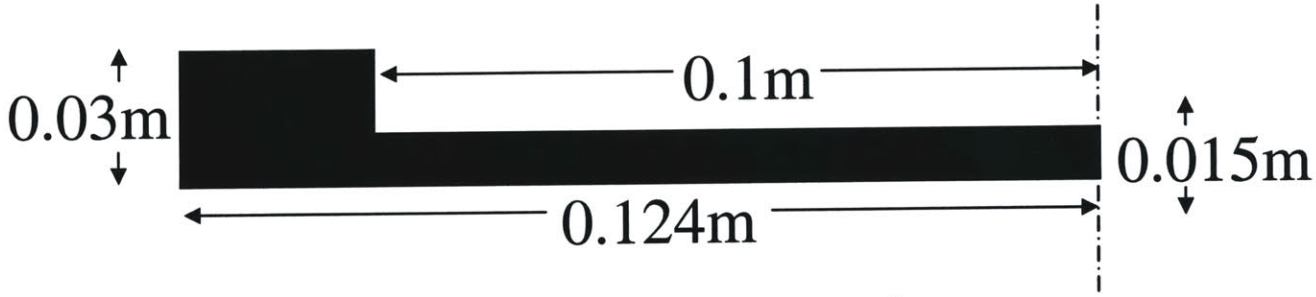

Figure 4.11: Reaction Wheel Dimensions[5]

A cobalt motor, ASTRO-40, is used to spin the reaction wheel. A DC motor can be modeled using its torque constant, Kt, electromotive force constant, Ke, internal resistance, Ra, and a friction constant, b.[8]

$$V = (\mathrm{T} + b\omega)\frac{R_a}{K_t} + K_e\omega \tag{4.1}$$

The reaction wheel and motor exhibited behavior that matched this model with a constant friction term added to the product $b\omega$. A step input in voltage can be used to determine the frictional constant, given the other constants. Below is the speed response from a voltage step of one volt.

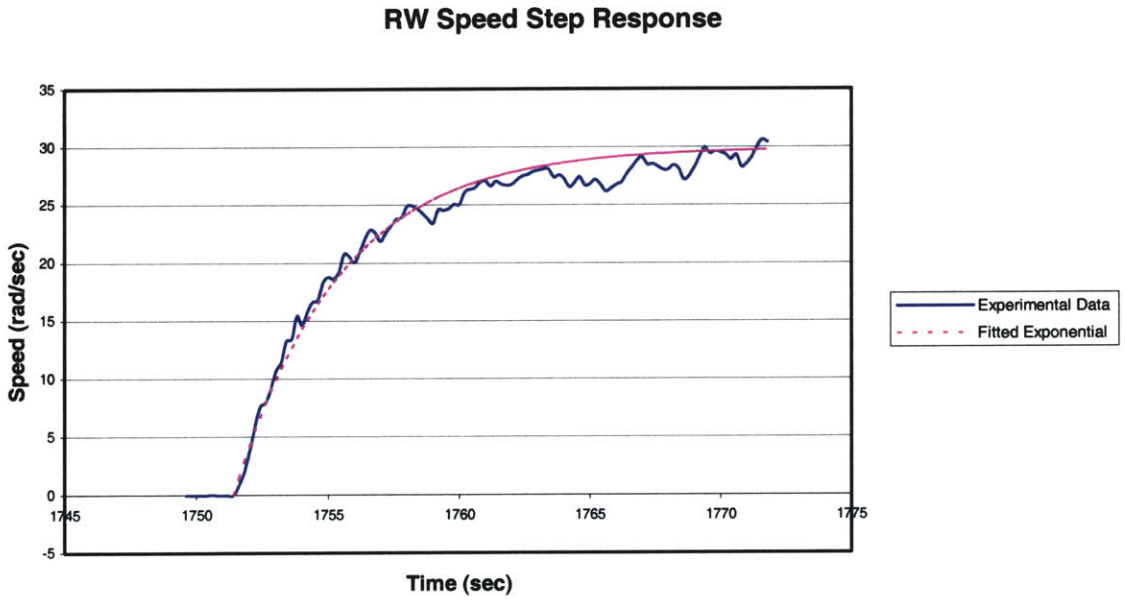

Figure 4.12: Reaction Wheel Step Response

This data was used to solve for a general friction term in place of the $b\omega$ term. It was found that this term had the form of a constant that opposed the direction of rotation added to a constant multiplied by the reaction wheel speed. The plot of the friction term is shown below.

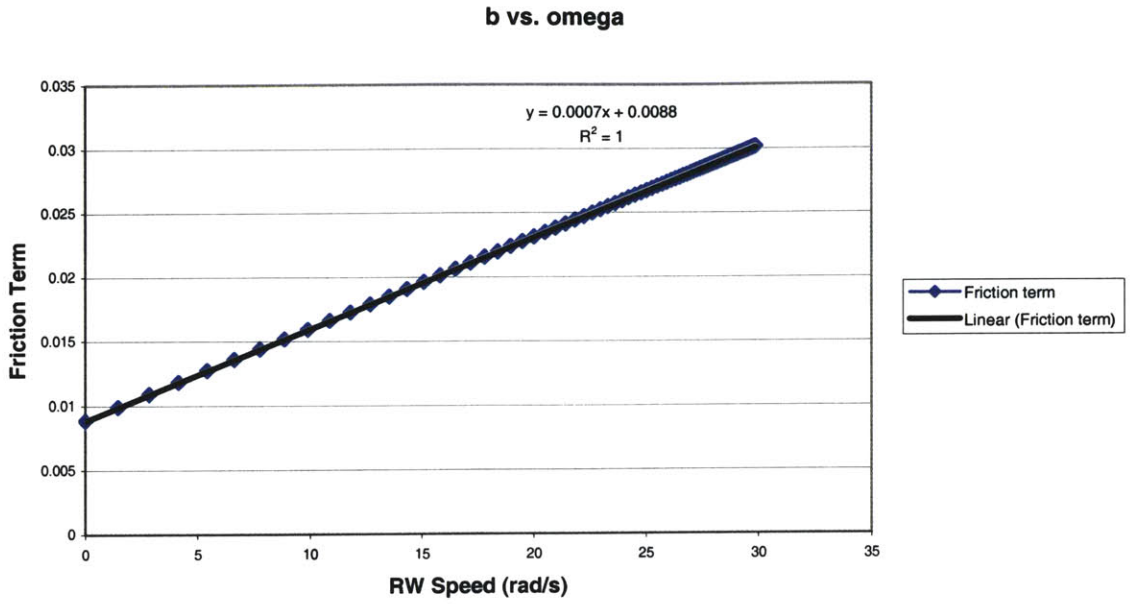

Figure 4.13: Friction Term of Reaction Wheel Model vs. Speed

The motor model used on the testbed is shown below with reaction wheel speed measured in radians per second.

$$V = \left(\mathrm{T} + 0.0088 \bullet rw\_direction + 0.0007 \bullet \omega\right)\frac{R_a}{K_t} + K_e\omega \tag{4.2}$$

The behavior of the reaction wheel when decelerating is slower than the acceleration case shown above. Another model could be developed for this case, but since the behavior is close to actual behavior, this model should suffice.

4.2 Physical Properties

The mass of an EMFF vehicle is approximately 36 kilograms when full of liquid nitrogen. This mass is broken down into sub-components to estimate the moment of inertia of the vehicle. The two containers, with the coils and liquid nitrogen inside can be

approximated as a solid torus with a cross-sectional radius of "a". The inertia of a ring of this type is calculated using

$$I_{xx,yy} = \frac{1}{8}\left(5a^2 + 4r^2\right)M \tag{4.3}$$

The inertias of the tank and other components can be added to determine an estimate of the total inertia of the system.

Table 4.2: EMFF Mass and Inertia Estimates

Component	Mass (kg)	Radius (m)	Cross-sectional radius (m)	Moment of Inertia (kg m²)
Large Coil	9	0.425	0.02	0.82
Small Coil	8	0.395	0.02	0.63
Tank	9.25	0.198		0.18
Structural Ring	0.75	0.45		0.08
Other Components	9	0.2		0.18
Total	36			1.89

Chapter 5

One-Vehicle Control Models

Initial tests in using electromagnetic control in the lab use one moving vehicle, which interacts with a stationary vehicle on the same table. This set-up simplifies the control requirements and allows testing on a relatively small area. With two vehicles moving, the center of mass can drift due to disturbances, so a larger area is needed to allow for this movement. With only one moving vehicle, the table provides reaction forces against the stationary vehicle and the moving vehicle can be maneuvered into any position. For simplification in control, the stationary vehicle is commanded to have constant current in one coil. The current in the coils on the moving vehicle are manipulated to provide control for the system. The basic layout of the testbed is shown below.

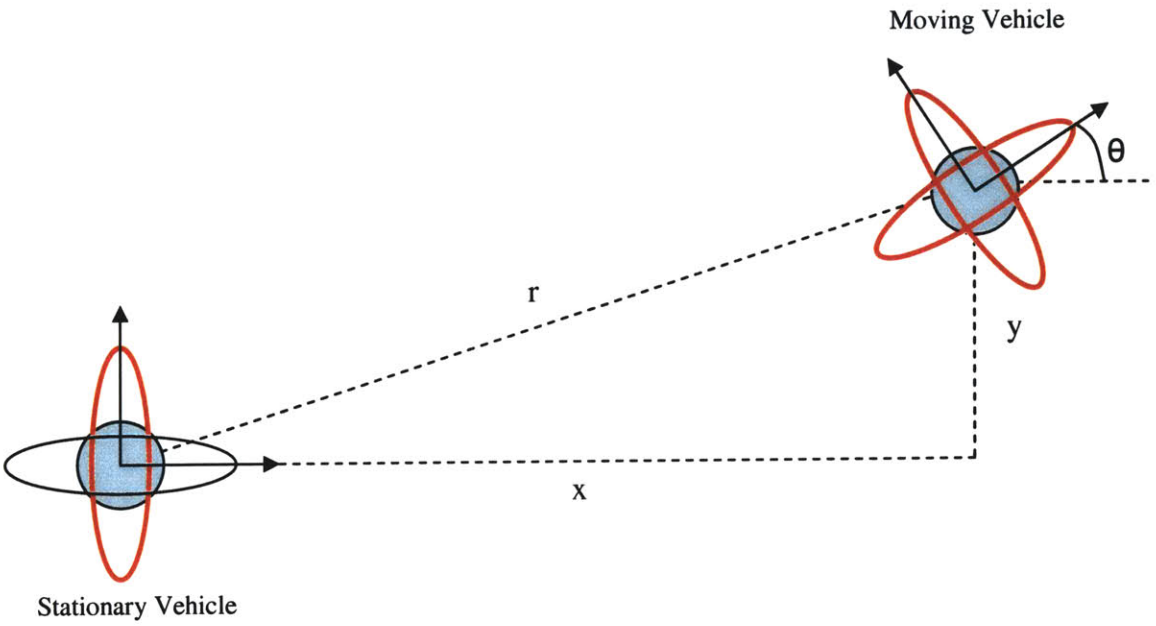

Figure 5.1: Testbed Set-up

5.1 Field Models

Permanent magnets and current-carrying conductors create a magnetic field, or B-field, around themselves. In a permanent magnet the field is represented by closed loops, with lines leaving the north pole of the magnet and entering at the south pole. Any moving electric charge creates such a field. The interaction of these fields create forces. Most current-carrying wires have very small fields, and their orientations cause the fields to cancel each other, so there is no large net force. However, with a ring of current, the B-fields from the charges moving through the coil add up to create a larger B-field. The symmetry of the coil simplifies the relationship between the motion of the electric charges and the field created. This section will explore ways of modeling the forces created between coils of current in varying levels of fidelity.

5.1.1 Far Field

At distances far from a coil of current, the magnetic field created looks the same as that created by a magnetic dipole, or a permanent magnet, with a north and south pole. The dipole points through the center of the coil, with its direction determined by the right-hand rule. Figure 5.2 illustrates this concept. The strength of the dipole is determined by the amount of current flowing through the coil, how many turns of wire are in the coil, and the area enclosed by the coil, as seen in Equation (5.1). This approximation of the B-field in a coil of current is called the Far Field approximation.

$$\mu = NiA \tag{5.1}$$

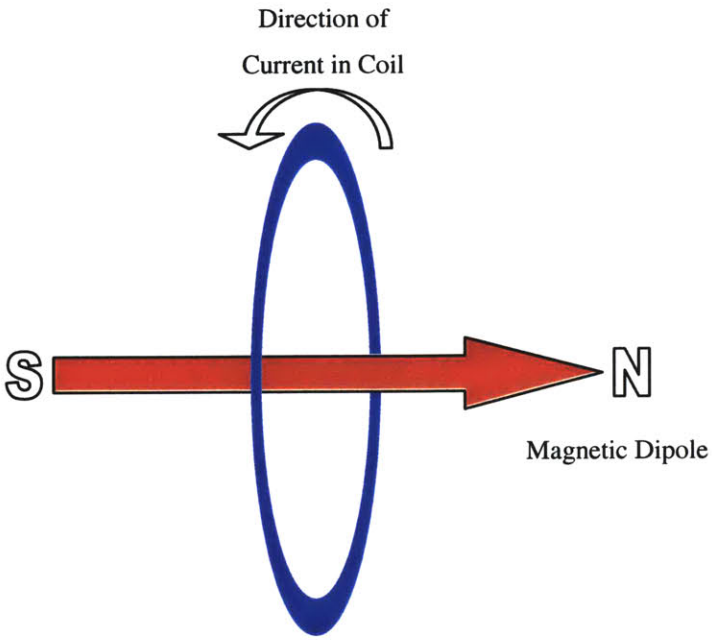

Figure 5.2: Magnetic Dipole Approximation of Coil of Current

Since each vehicle has two coils that are structurally connected to each other, the dipoles created by each coil add into a resultant dipole. If each orthogonal coil is creating a dipole of equal strength, it is like having a dipole pointed diagonally between them with a magnitude equal to $\sqrt{2}$ times their individual magnitudes. This phenomenon allows us to steer the dipole by changing the amount of current in each coil. Using this far field approximation, the testbed layout simplifies to two dipoles, as shown below.

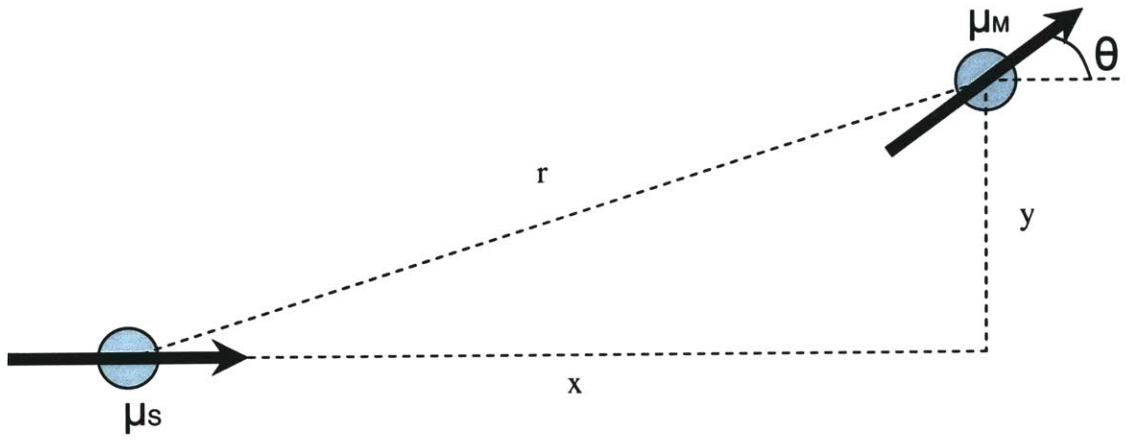

Figure 5.3: Testbed set-up with far-field approximation

The B-field created by a magnetic dipole is described by equation (5.2).[9] μ_0 is the permeability constant, $4\pi\times10^{-7}T\cdot m/A$. μ is the magnitude of the dipole moment, and $\hat{\boldsymbol{\mu}}$ its direction. r is the distance to the point where you are calculating the B-field and $\hat{\mathbf{r}}$ is the direction from the dipole to that point.

$$\mathbf{B}=\frac{\mu_0}{4\pi}\left(\frac{\mu}{r^3}\right)\left[3\left(\hat{\boldsymbol{\mu}}\cdot\hat{\mathbf{r}}\right)\hat{\mathbf{r}}-\hat{\boldsymbol{\mu}}\right] \tag{5.2}$$

The force experienced by a dipole in a B-field is calculated by equation (5.3). Force depends on the gradient of the B-field.

$$\mathbf{F}=\boldsymbol{\mu}_M\bullet\nabla\mathbf{B}_S \tag{5.3}$$

Torque on the dipole in a B-field is calculated by equation (5.4).

$$\mathbf{T}=\boldsymbol{\mu}_M\times\mathbf{B}_S \tag{5.4}$$

Using these three equations, we can find the force and torque on a magnetic dipole in the presence of another magnetic dipole. The following equations describe the forces and torques on the moving dipole, $\vec{\mu}_M$, as a result of its interaction with the stationary dipole, $\vec{\mu}_S$, using the coordinates shown in Figure 5.1: Testbed Set-up.

$$\mathbf{F}_x=\frac{-3\mu_0}{4\pi}\left[\frac{\mu_S\mu_M}{x^2+y^2}\right]\left\{\left(\frac{5x^3}{\left(x^2+y^2\right)^{3/2}}-\frac{3x}{\left(x^2+y^2\right)^{1/2}}\right)\cos\theta+\left(\frac{5x^2y}{\left(x^2+y^2\right)^{3/2}}-\frac{y}{\left(x^2+y^2\right)^{1/2}}\right)\sin\theta\right\} \tag{5.5}$$

$$\mathbf{F}_y=\frac{-3\mu_0}{4\pi}\left[\frac{\mu_S\mu_M}{x^2+y^2}\right]\left\{\left(\frac{5x^2y}{\left(x^2+y^2\right)^{3/2}}-\frac{y}{\left(x^2+y^2\right)^{1/2}}\right)\cos\theta+\left(\frac{5xy^2}{\left(x^2+y^2\right)^{3/2}}-\frac{x}{\left(x^2+y^2\right)^{1/2}}\right)\sin\theta\right\} \tag{5.6}$$

$$\mathbf{T}_z=\frac{\mu_0}{4\pi}\left[\frac{\mu_S\mu_M}{\left(x^2+y^2\right)^{3/2}}\right]\left\{\left(\frac{3xy}{\left(x^2+y^2\right)}\right)\cos\theta+\left(1-\frac{3x^2}{\left(x^2+y^2\right)}\right)\sin\theta\right\} \tag{5.7}$$

5.1.2 Near Field

At distances less than a few radii from the coil, the far field approximation does not represent the system as well as at large distances. The forces experienced by the coils at small distances are smaller than what the far field model would estimate. The exact amount of force created by the coils can be calculated by investigating the influence of every moving charge in one coil on every moving charge in the other. For ease in calculation, each coil will be broken into segments that are assumed to be straight.

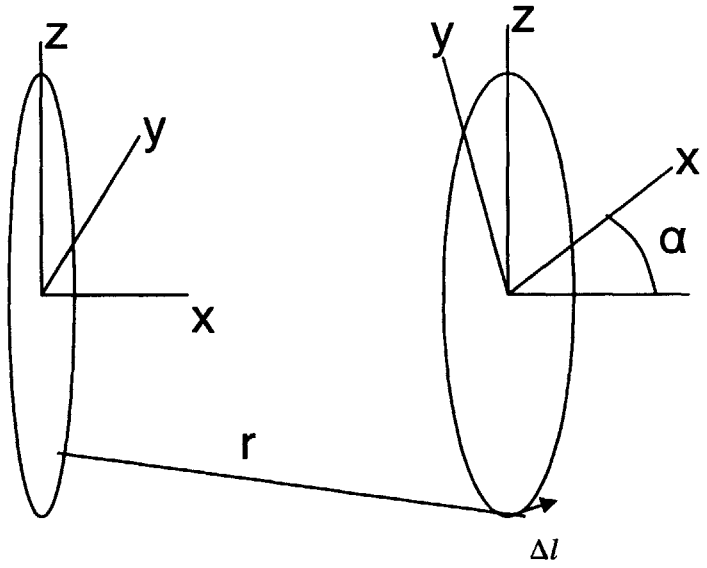

Figure 5.4: Coil set-up for near field integration

For calculation of the force between to coils, we will assume that the moving coil is at a position of (x_0, y_0) and at an angle of α. We will use the angles θ_S, θ_M to integrate about the coils. Each coil has radius R. The radius vector between each segment and the length segments for each coil, for given angles, are shown below.

$$\vec{r} = -\begin{bmatrix} 0 \\ R\cos\theta_S \\ R\sin\theta_S \end{bmatrix} + \begin{bmatrix} x_0 \\ y_0 \\ 0 \end{bmatrix} + \begin{bmatrix} -R\cos\theta_M \sin\alpha \\ R\cos\theta_M \cos\alpha \\ R\sin\theta_M \end{bmatrix} \tag{5.8}$$

$$\Delta l_S = \begin{bmatrix} 0 \\ -R\sin\theta_S \Delta\theta_S \\ R\cos\theta_S \Delta\theta_S \end{bmatrix} \tag{5.9}$$

$$\Delta l_M = \begin{bmatrix} R\sin\theta_M \sin\alpha\Delta\theta_M \\ -R\sin\theta_M \cos\alpha\Delta\theta_M \\ R\cos\theta_M \Delta\theta_M \end{bmatrix} \tag{5.10}$$

Mathematical integration can be used to calculate the force influence of one segment of the stationary coil on each segment of the moving coil. Integrating again allows us to add the force contributions of each segment of the stationary coil on the moving coil. Below is the equation for calculating the exact force between two coils carrying current.

$$\vec{F}_M = \frac{\mu_o i_S i_M}{4\pi} \oint\oint \left(\frac{\vec{r} \times d\vec{l}_S}{r^3}\right) \times d\vec{l}_M \tag{5.11}$$

This integral can be calculated numerically as a double summation. This requires using finite length segments, whose size will determine the accuracy of the approximation. The more segments we use, the more accurate it will be. If we break each coil into N segments, the force between them can be calculated by the following equation.

$$\vec{F}_M \approx \frac{\mu_o i_S i_M}{4\pi} \sum_{i=1}^{N} \sum_{j=1}^{N} \frac{(\vec{r}_{ij} \times \Delta l_i)}{|r_{ij}|^3} \times \Delta l_j \tag{5.12}$$

$$\Delta\theta_S = \Delta\theta_M = \frac{2\pi}{N} \tag{5.13}$$

$$\theta_S = \frac{2j\pi}{N} \quad \theta_M = \frac{2i\pi}{N} \tag{5.14}$$

It was found that using a value of 25 for N gave the same 13 significant digits as using 100 for N. This means that we can calculate the force between two coils in the near field very accurately in a reasonable amount of time.

5.2 Control Methods

5.2.1 Angle Control

In two dimensions, a steerable magnetic dipole on one vehicle can provide full position control between itself and a vehicle with a fixed magnetic dipole. However, in implementing this control, torques would be constantly applied to this vehicle causing it to rotate uncontrollably. By adding a reaction wheel to this system, the angular position of the vehicle can be controlled. This method decouples the position and angle control of the EMFF vehicle. The two superconducting coils are used to control the two-dimensional position of the vehicle and the reaction wheel is used to control the angle of the vehicle. This method simplifies the implementation of more complex controllers for the magnetic coils.

The state-space representation of the angle control system is quite simple. The torque of the reaction wheel provides an opposite torque on the vehicle, to preserve angular momentum. This torque causes an angular acceleration on the vehicle, proportional to its moment of inertia.

$$\begin{bmatrix} \dot{\alpha} \\ \ddot{\alpha} \end{bmatrix} = \begin{bmatrix} 0 & 1 \\ 0 & 0 \end{bmatrix} \begin{bmatrix} \alpha \\ \dot{\alpha} \end{bmatrix} + \begin{bmatrix} 0 \\ 1/I \end{bmatrix} T_{RW} \tag{5.15}$$

A controller was developed for this system using the optimal control method explained in the next section. To provide sufficient resistance to the torque to be imposed by the magnetic control, large weighting was applied to keeping the angular rate of the system at zero. The weighting functions used are shown below. According to Bryson's rule this weighting should keep angular error below 0.04 radians, angular rate below 0.02 rad/sec, and maximum torque should be 0.22 Nm.

$$Q = \begin{bmatrix} 600 & 0 \\ 0 & 3000 \end{bmatrix} \quad R = 20 \tag{5.16}$$

This yields a full-state controller of the form $u = -Kx$.

$$K = [3.0574 \quad 7.6352] \tag{5.17}$$

5.2.2 Linearization

All real systems have a nonlinear relationship between the inputs and outputs, due to friction and other effects. In most systems, the nonlinear effects are very small when operating near the nominal point. In the EMFF system, as radius increases, force drops off proportional to r^{-4}. This makes the system inherently very nonlinear. Even so, at locations very close to the operating point, the dynamics can be approximated as being linear.

To develop a controller for the EMFF system, state-space techniques will be used as presented in the Feedback Control Systems class at MIT.[10] First, a state-space model must be developed to describe the dynamics of the system. This model describes the change in each state over time as a linear combination of the states and inputs. $\mathbf{A}, \mathbf{B}, \mathbf{C}, \mathbf{D}$ are matrices of constants. $\mathbf{x}, \mathbf{u}, \mathbf{y}$ are vectors of the states, inputs and outputs, respectively.

$$\begin{aligned} \dot{\mathbf{x}}(t) &= \mathbf{A}\mathbf{x}(t) + \mathbf{B}\mathbf{u}(t) \\ \mathbf{y}(t) &= \mathbf{C}\mathbf{x}(t) + \mathbf{D}\mathbf{u}(t) \end{aligned} \tag{5.18}$$

The dynamics of most systems can be described by nonlinear functions of the state and inputs. Here $f(\mathbf{x}, \mathbf{u})$ is a nonlinear vector function of the state and input vectors.

$$\dot{\mathbf{x}} = f(\mathbf{x}, \mathbf{u}) \tag{5.19}$$

To linearize this relationship, we look at the response of the system to a small change in each state and input. Using the first term of the Taylor Series Expansion, we get the following relationship.

$$\frac{d}{dt}(\delta \mathbf{x}) \approx \left.\frac{\partial f}{\partial x}\right|_0 \delta \mathbf{x} + \left.\frac{\partial f}{\partial u}\right|_0 \delta \mathbf{u} \tag{5.20}$$

This yields A and B matrices as derivatives of the nonlinear function describing the dynamics.

$$\mathbf{A} \equiv \begin{bmatrix} \frac{\partial f_1}{\partial x_1} & \frac{\partial f_1}{\partial x_2} & \cdots & \frac{\partial f_1}{\partial x_n} \\ \frac{\partial f_2}{\partial x_1} & \frac{\partial f_2}{\partial x_2} & \cdots & \frac{\partial f_2}{\partial x_n} \\ & & \vdots & \\ \frac{\partial f_n}{\partial x_1} & \frac{\partial f_n}{\partial x_2} & \cdots & \frac{\partial f_n}{\partial x_n} \end{bmatrix}_0 \qquad \mathbf{B} \equiv \begin{bmatrix} \frac{\partial f_1}{\partial u_1} & \frac{\partial f_1}{\partial u_2} & \cdots & \frac{\partial f_1}{\partial u_m} \\ \frac{\partial f_2}{\partial u_1} & \frac{\partial f_2}{\partial u_2} & \cdots & \frac{\partial f_2}{\partial u_m} \\ & & \vdots & \\ \frac{\partial f_n}{\partial u_1} & \frac{\partial f_n}{\partial u_2} & \cdots & \frac{\partial f_n}{\partial u_m} \end{bmatrix}_0 \tag{5.21}$$

For our system, we have found nonlinear equations relating the force and torque on the moving vehicle as functions of its position and the current applied. We also have a torque applied by the reaction wheel.

$$\begin{bmatrix} \ddot{x}_M \\ \ddot{y}_M \\ \ddot{\alpha}_M \end{bmatrix} = \begin{bmatrix} \frac{F_x}{m_M} \\ \frac{F_y}{m_M} \\ \frac{T_z + T_{rw}}{I_M} \end{bmatrix} \tag{5.22}$$

Our state vector is composed of x position and velocity, y position and velocity, and bearing angle and angular rate. Our inputs are the current applied to each coil and the torque from the reaction wheel.

$$\mathbf{x} = \begin{bmatrix} x \\ \dot{x} \\ y \\ \dot{y} \\ \alpha \\ \dot{\alpha} \end{bmatrix} \qquad \mathbf{u} = \begin{bmatrix} i_x \\ i_y \\ \mathrm{T}_{RW} \end{bmatrix} \tag{5.23}$$

To determine the linearized, state-space model for our system, we must differentiate our dynamic equations with respect to each state and input.

$$A = \begin{bmatrix} 0 & 1 & 0 & 0 & 0 & 0 \\ \frac{\partial}{\partial x}\left(\frac{F_x}{m_M}\right)\Big|_0 & \frac{\partial}{\partial \dot{x}}\left(\frac{F_x}{m_M}\right)\Big|_0 & \frac{\partial}{\partial y}\left(\frac{F_x}{m_M}\right)\Big|_0 & \frac{\partial}{\partial \dot{y}}\left(\frac{F_x}{m_M}\right)\Big|_0 & \frac{\partial}{\partial \alpha}\left(\frac{F_x}{m_M}\right)\Big|_0 & \frac{\partial}{\partial \dot{\alpha}}\left(\frac{F_x}{m_M}\right)\Big|_0 \\ 0 & 0 & 0 & 1 & 0 & 0 \\ \frac{\partial}{\partial x}\left(\frac{F_y}{m_M}\right)\Big|_0 & \frac{\partial}{\partial \dot{x}}\left(\frac{F_y}{m_M}\right)\Big|_0 & \frac{\partial}{\partial y}\left(\frac{F_y}{m_M}\right)\Big|_0 & \frac{\partial}{\partial \dot{y}}\left(\frac{F_y}{m_M}\right)\Big|_0 & \frac{\partial}{\partial \alpha}\left(\frac{F_y}{m_M}\right)\Big|_0 & \frac{\partial}{\partial \dot{\alpha}}\left(\frac{F_y}{m_M}\right)\Big|_0 \\ 0 & 0 & 0 & 0 & 0 & 1 \\ \frac{\partial}{\partial x}\left(\frac{T_z + T_{RW}}{I_M}\right)\Big|_0 & \frac{\partial}{\partial \dot{x}}\left(\frac{T_z + T_{RW}}{I_M}\right)\Big|_0 & \frac{\partial}{\partial y}\left(\frac{T_z + T_{RW}}{I_M}\right)\Big|_0 & \frac{\partial}{\partial \dot{y}}\left(\frac{T_z + T_{RW}}{I_M}\right)\Big|_0 & \frac{\partial}{\partial \alpha}\left(\frac{T_z + T_{RW}}{I_M}\right)\Big|_0 & \frac{\partial}{\partial \dot{\alpha}}\left(\frac{T_z + T_{RW}}{I_M}\right)\Big|_0 \end{bmatrix} \tag{5.24}$$

$$B = \begin{bmatrix} 0 & 0 & 0 \\ \left.\frac{\partial}{\partial i_x}\left(\frac{F_x}{m_M}\right)\right|_0 & \left.\frac{\partial}{\partial i_y}\left(\frac{F_x}{m_M}\right)\right|_0 & \left.\frac{\partial}{\partial T_{RW}}\left(\frac{F_x}{m_M}\right)\right|_0 \\ 0 & 0 & 0 \\ \left.\frac{\partial}{\partial i_x}\left(\frac{F_y}{m_M}\right)\right|_0 & \left.\frac{\partial}{\partial i_y}\left(\frac{F_y}{m_M}\right)\right|_0 & \left.\frac{\partial}{\partial T_{RW}}\left(\frac{F_y}{m_M}\right)\right|_0 \\ 0 & 0 & 0 \\ \left.\frac{\partial}{\partial i_x}\left(\frac{T_z + T_{RW}}{I_M}\right)\right|_0 & \left.\frac{\partial}{\partial i_y}\left(\frac{T_z + T_{RW}}{I_M}\right)\right|_0 & \left.\frac{\partial}{\partial T_{RW}}\left(\frac{T_z + T_{RW}}{I_M}\right)\right|_0 \end{bmatrix} \tag{5.25}$$

If we assume that the moving vehicle has no current in its coils initially, the A matrix will always be as follows.

$$A = \begin{bmatrix} 0 & 1 & 0 & 0 & 0 & 0 \\ 0 & 0 & 0 & 0 & 0 & 0 \\ 0 & 0 & 0 & 1 & 0 & 0 \\ 0 & 0 & 0 & 0 & 0 & 0 \\ 0 & 0 & 0 & 0 & 0 & 1 \\ 0 & 0 & 0 & 0 & 0 & 0 \end{bmatrix} \tag{5.26}$$

With a reference position, $\mathbf{x}_r$, the B matrix can be calculated for both the far field model and the near field model. In both cases the current in the x and y coils are multiplicative factors in the forces and torques created by the coils. Therefore, the derivative with respect to current in the coil is the rest of the expression, excluding the current term.

$$\mathbf{x}_r = \begin{bmatrix} 1.5 \\ 0 \\ 0 \\ 0 \\ \pi \\ 0 \end{bmatrix} \quad \mathbf{B}_{far-field} = \begin{bmatrix} 0 & 0 & 0 \\ 0.00046239 & 0 & 0 \\ 0 & 0 & 0 \\ 0 & -0.00023119 & 0 \\ 0 & 0 & 0 \\ 0 & 0.0044037 & 0.5291 \end{bmatrix}$$

$$\mathbf{B}_{near-field} = \begin{bmatrix} 0 & 0 & 0 \\ 0.00033021 & 0 & 0 \\ 0 & 0 & 0 \\ 0 & -0.00021557 & 0 \\ 0 & 0 & 0 \\ 0 & 0.00454 & 0.5291 \end{bmatrix} \tag{5.27}$$

Given A and B matrices, an optimal controller can be developed to maximize performance. A Linear Quadratic Regulator, LQR, was determined by minimizing a cost function, J, composed of weighted state error and control variables.

$$\min J = \int \vec{x}^T Q\vec{x} + \vec{u}^T R\vec{u}dt \tag{5.28}$$

The algebraic Riccati equation is used to determine the correct gains for the controller.

$$\begin{aligned} A^T P + PA - PBR^{-1}B^T P + Q = 0 \\ K_{LQR} = R^{-1}B^T P \end{aligned} \tag{5.29}$$

Bryson's rule was used to determine weighting matrices Q and R for the state error and control variables, respectively. The weighting for a specific state is dependent on the expected maximum value it will take. This method adjusts for different scaling of variables. The controller was initially designed to keep position accurate to one centimeter and to allow for current inputs of 100 amps. This weighting was found to use too much control so the weights were adjusted as shown in the next section.

$$q_i = \frac{1}{x_{\max i}^2} \quad r_i = \frac{1}{u_{\max i}^2} \tag{5.30}$$

$$Q = \begin{bmatrix} 10000 & 0 & 0 & 0 & 0 & 0 \\ 0 & 1 & 0 & 0 & 0 & 0 \\ 0 & 0 & 10000 & 0 & 0 & 0 \\ 0 & 0 & 0 & 1 & 0 & 0 \\ 0 & 0 & 0 & 0 & 1 & 0 \\ 0 & 0 & 0 & 0 & 0 & 1 \end{bmatrix} \quad R = \begin{bmatrix} 0.0001 & 0 & 0 \\ 0 & 0.0001 & 0 \\ 0 & 0 & 0.000001 \end{bmatrix} \tag{5.31}$$

This method yields gains, which define the control law as

$$\mathbf{u}(t) = -K_{LQR}\mathbf{x}(t) \tag{5.32}$$

A low weight on reaction wheel control in the R matrix, decouples the angle control from the magnetic coils. The resulting controller assumes that the reaction wheel will provide full angle control and the angle measurement feedback is not used to calculate magnetic control.

5.2.3 Gain Scheduling

A linear controller works well near its nominal point. However, as we operate farther from that point, the behavior degrades. It is possible to design multiple controllers for various operating points and determine an algorithm for switching to the appropriate controller for the given state.

5.2.4 Sliding Mode Controller

Since the dynamics of the EMFF system are inherently nonlinear, it seems that the best approach to controlling it is with an inherently nonlinear control method. A sliding mode controller uses the nonlinear dynamics of the system to calculate control. It is explained in detail in Applied Nonlinear Control.[11] With the far field model the inputs (dipole

strength) multiply a state dependent quantity to produce forces and torques. This means that we can describe the dynamics primarily through the B matrix.

The exact B matrix would include additional terms to account for being in the near field. We will define a matrix $\hat{B}$ as our estimate to the actual B matrix. It contains the far field model. The near field terms are included as an uncertainty on the B matrix and are bounded by the elements of another matrix labeled as D. Uncertainties on the matrix B are written in multiplicative form.

$$\hat{B} = \frac{3\mu_0\mu_S}{4\pi m_M}\begin{bmatrix} \dfrac{-2x_M^3 + 3x_M y_M^2}{(x_M^2 + y_M^2)^{7/2}} & \dfrac{-4x_M^2 y_M + y_M^3}{(x_M^2 + y_M^2)^{7/2}} \\ \dfrac{-4x_M^2 y_M + y_M^3}{(x_M^2 + y_M^2)^{7/2}} & \dfrac{x_M^3 - 4x_M y_M^2}{(x_M^2 + y_M^2)^{7/2}} \end{bmatrix} \tag{5.33}$$

$$B = (I + \Delta)\hat{B} \quad |\Delta_{ij}| \le D_{ij} \quad i = 1,2 \quad j = 1,2 \tag{5.34}$$

A simulation was run that uses double integration over the two coils of wire in the moving vehicle to find the exact forces between the two vehicles. In the worst case the actual force is half of what the far field model gives. For this reason the controller was initially designed to handle uncertainties in the B matrix of a factor of 2. The bounding matrix for uncertainties used is shown below.

$$D = \begin{bmatrix} 1.1 & 0.01 \\ 0.01 & 1.1 \end{bmatrix} \tag{5.35}$$

To implement sliding control on the EMFF testbed two sliding surfaces, s_1 and s_2, must be defined. The sliding surfaces are defined by the vector equation $\mathbf{s}(\mathbf{x},t) = 0$. s_1 and s_2 are weighted sums of position and velocity errors. Therefore, if $\mathbf{s}$ goes to zero, the position and velocity error will also go to zero.

$$s_1 = \dot{\tilde{x}} + \lambda_1 \tilde{x} \quad \tilde{x} = x - x_d$$
$$s_2 = \dot{\tilde{y}} + \lambda_2 \tilde{y} \quad \tilde{y} = y - y_d \tag{5.36}$$

For notational compactness, we introduce the variable x_r.

$$\dot{x}_{ri} = \dot{x}_{di} - \lambda_i \tilde{x}_i \quad s_i = \dot{x}_i - \dot{x}_{ri} \tag{5.37}$$

To cause **s** to remain at zero, the control input $\vec{u}$ must satisfy the individual sliding conditions of the form

$$\frac{1}{2}\frac{d}{dt} s_i^2 \leq -\eta_i |s_i| \qquad (\eta_i > 0) \tag{5.38}$$

If this is true, all trajectories of **s** will approach the surface $S(t)$ as shown here.

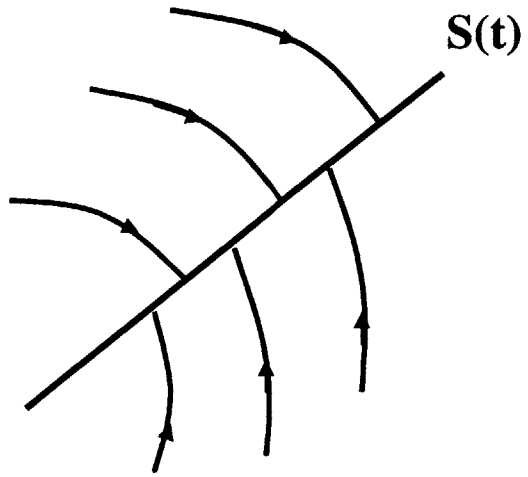

Figure 5.5: The Sliding Condition

The control law takes the form

$$\vec{u} = \hat{B}^{-1}(\dot{\vec{x}}_r - \vec{k}\,\mathrm{sgn}(\vec{s})) \tag{5.39}$$

The two switching gains can now be solved for

$$\bar{k} = \begin{bmatrix} \dfrac{(1-D_{22})}{(1-D_{11})(1-D_{22})-D_{12}D_{21}}\left(\eta_1 - \dfrac{D_{12}}{1-D_{22}}\left(\eta_2 + (D_{21}+D_{22})|\dot{x}_{r2}|\right) + (D_{11}+D_{12})|\dot{x}_{r1}|\right) \\ \dfrac{(1-D_{11})}{(1-D_{22})(1-D_{11})-D_{21}D_{12}}\left(\eta_2 - \dfrac{D_{21}}{1-D_{11}}\left(\eta_1 + (D_{11}+D_{12})|\dot{x}_{r1}|\right) + (D_{21}+D_{22})|\dot{x}_{r2}|\right) \end{bmatrix} \quad (5.40)$$

The values used for our controller are

$$\begin{aligned} \eta_1 &= 0.01 \quad \lambda_1 = 0.79 \\ \eta_2 &= 0.01 \quad \lambda_2 = 0.79 \end{aligned} \quad (5.41)$$

The controller described above exhibited chattering behavior, which hindered the execution of the simulation and would require unachievable control speeds. This is caused by the trajectories overshooting the sliding surface and oscillating about $s = 0$. To solve this problem, a boundary layer of thickness Φ was introduced. This allows the trajectory to coast when near the sliding surface.

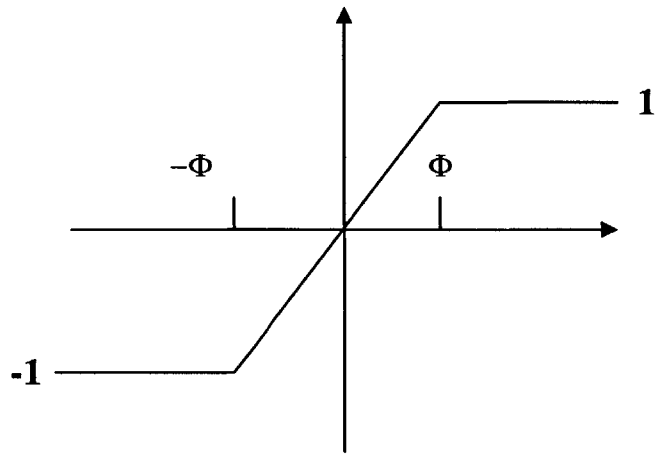

Figure 5.6: Saturation Function, sat(s/Φ)

The new control law is

$$\vec{u} = \hat{B}^{-1}\left(\dot{\vec{x}}_r - \begin{bmatrix} k_1 sat(s_1/\Phi_1) \\ k_2 sat(s_2/\Phi_2) \end{bmatrix}\right) \tag{5.42}$$

For simplicity we used a constant boundary layer Φ=0.15, which yielded satisfactory results.

5.3 Simulation Description

Multiple simulations were created to evaluate various controllers using both the far-field and near-field models. Simulations using the far-field model can be executed very quickly, but do not fully model the magnetic interactions experienced in reality. The near-field model, as described previously, uses double integration about the coils to solve very accurately for the forces and torques experienced by the vehicles. However, this accuracy comes with the cost of much longer execution time.

The following sections evaluate simulations run with multiple combinations of controllers and dynamics models. The first controller is called the far-field controller. It is a linear controller developed using a dynamics model that assumes that the superconducting coils behave as magnetic dipoles. This controller should give its best performance when used in the far-field simulation. When it is used in a near-field simulation it should not perform as well because it assumes that it will get more force for a given commanded current than it actually does.

The second controller, the near-field controller, is also a linear controller, but it is developed using a dynamics model that assumes that the coils interact according to the near-field model. Both of these linear controllers are developed using optimal control techniques with the same weighting matrices, but they have different B matrices due to the different field models used. The main purpose of the far-field controller is to provide a fast way to evaluate a controller without having to run the time consuming near-field simulation. The behavior exhibited by the far-field controller in the far-field simulation

should be very close to what would be expected of the near-field controller run in the near-field simulation.

The final controller developed is the nonlinear, sliding mode controller. There is only one nonlinear controller that is evaluated. It uses the far-field model to calculate control, but also assumes an error in the model due to near-field effects as described in 5.2.3.

The simulations were implemented in Matlab using Simulink. The simulation was designed to model the actual system as closely as possible. The coils can carry close to 90 amps of current. This characteristic was included in the simulation as a saturation on the commanded current. We also know that the coil current controller has a pole at 5.65 rad/sec. This behavior was also included in the model and gives the assurance that the electric current switching speeds we see in the simulations are physically realizable on the testbed. Small amplitude, band-limited white noise was also included to simulate the testbed more accurately.

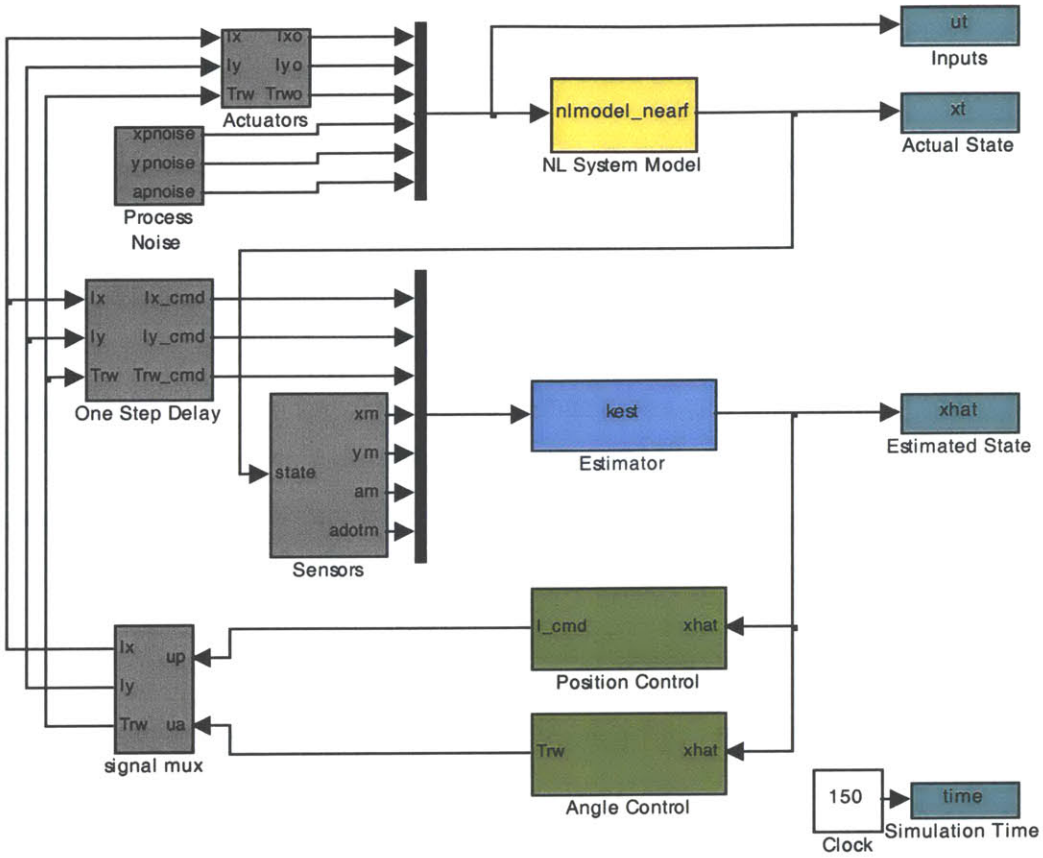

Figure 5.7: Testbed Control Simulation

The "NL System Model" block contains the appropriate nonlinear model of the dynamics, either with the far-field or near-field model. It takes in the control commands as inputs and outputs the simulated state. The "Estimator" block contains the same discrete kalman filter that is used on the testbed. Its inputs are the control commands that were applied to the system in the last iteration and the measured state variables. Position information for x, y and alpha are given to the estimator to simulate the metrology measurement and angular rate is also supplied to the estimator because the gyroscope supplies this information on the testbed. The estimator gives an estimate of the full state of the system. The separated angle and position control is shown by the two control blocks. The "Angle Control" block contains the linear angle controller described in 5.2.1 and outputs the commanded reaction wheel torque. Either the linear position controller

or nonlinear position controller can be placed in the "Position Control" block. This controller outputs the commanded current in each coil of the vehicle. The blocks on the left side of the simulation are used to more fully model the details of the actual system.

5.4 Controller Development

Most implementations of the EMFF concept will require accurate trajectory following. Therefore, the linear and non-linear controllers were developed to provide effective control in following a trajectory involving both radial and shear directions. A sinusoid in both the x and y directions was commanded with a frequency of 0.2 rad/sec and an amplitude of 0.25 meters in the x direction and 0.2 meters in the y-direction. The controllers were adjusted until the maximum error in the x and y directions was close to five centimeters. The far-field simulation was used to test the controllers because of its execution speed.

The weighting matrices that gave satisfactory control using linear methods are as follows.

$$Q=\begin{bmatrix} 10000 & 0 & 0 & 0 & 0 & 0 \\ 0 & 1 & 0 & 0 & 0 & 0 \\ 0 & 0 & 10000 & 0 & 0 & 0 \\ 0 & 0 & 0 & 1 & 0 & 0 \\ 0 & 0 & 0 & 0 & 1 & 0 \\ 0 & 0 & 0 & 0 & 0 & 1 \end{bmatrix} \quad R=\begin{bmatrix} 0.003 & 0 & 0 \\ 0 & 0.003 & 0 \\ 0 & 0 & 0.000003 \end{bmatrix} \tag{5.43}$$

The gains for position control are then given below.

$$K_{far-field}=\begin{bmatrix} 1603.4 & 2633.6 & 0 & 0 & 0 & 0 \\ 0 & 0 & -1665.5 & -3795.8 & 0.00009 & 0.00009 \end{bmatrix} \tag{5.44}$$

$$K_{near-field}=\begin{bmatrix} 1636.0 & 3147.9 & 0 & 0 & 0 & 0 \\ 0 & 0 & -1670.8 & -3937.2 & 0.00009 & 0.00009 \end{bmatrix} \tag{5.45}$$

The linear controller using the far-field controller gains for position control has the following behavior in the far-field simulation.

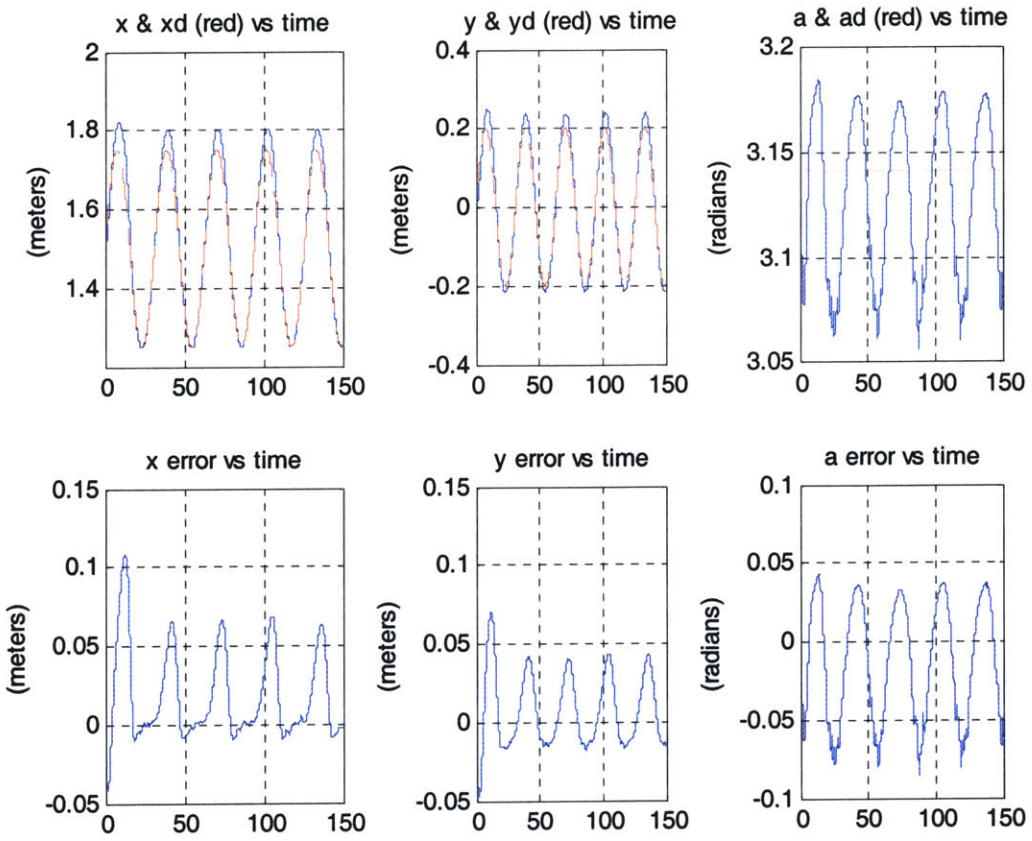

Figure 5.8: Linear Far-Field Controller Sinusoid Trajectory for Controller Development

The nonlinear controller was developed to have similar behavior when tracking two sinusoids. Its behavior is shown in Figure 5.9.

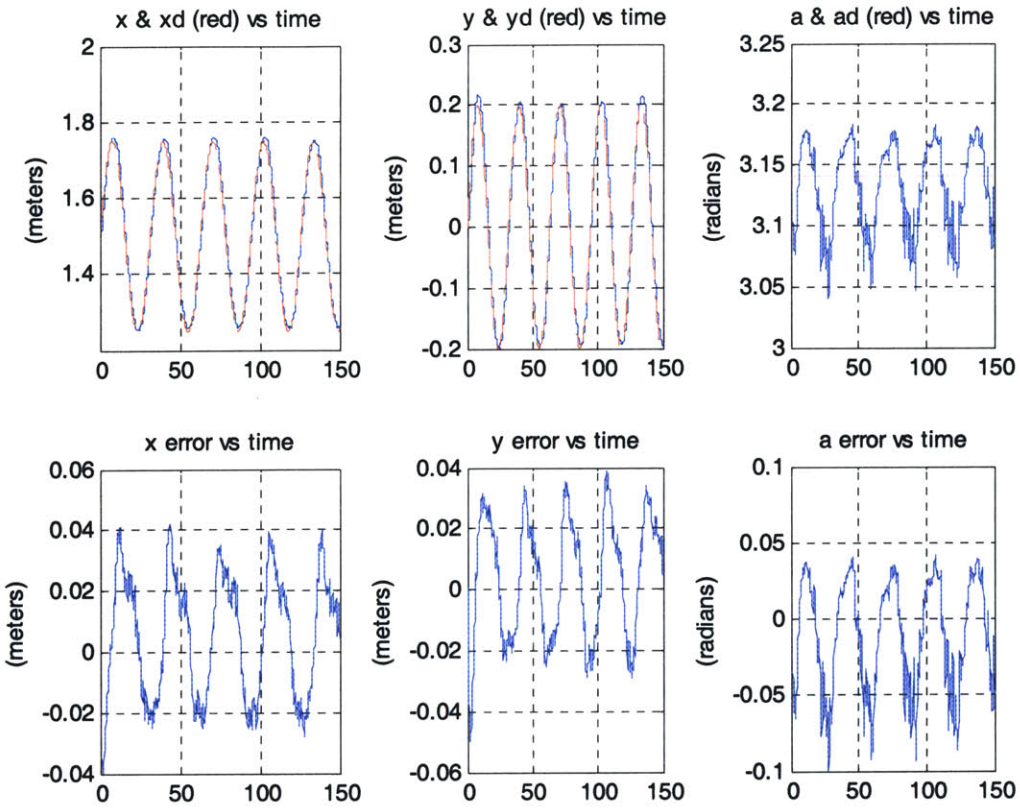

Figure 5.9: Nonlinear Controller Sinusoid Trajectory for Controller Development

Both controllers are able to follow a sinusoid in x and y position very well. The linear controller overshoots the trajectory when it is farthest from the nominal position and tracks very well when it is closer to the stationary vehicle and has more control authority. The nonlinear controller, which is not designed around an operating point, gives similar behavior at both extremes of the sinusoid. Both controllers also introduce a torque on the vehicle, which is opposed by the reaction wheel, and cause a maximum angle error of about 0.08 radians.

5.5 Maneuvers

To prove the concept of using electromagnetic forces to control satellite separation, it is necessary to show maneuvers involving disturbance rejection and trajectory following. The following section shows the results from simulations implementing the controllers

described above. Each controller was first implemented in a nonlinear simulation using the far-field approximation of coil interaction. After the controller showed satisfactory behavior in the far-field, the controller was then tested using a nonlinear simulation using a near-field approximation with double integration about each powered coil, as described previously. The results of the simulation are labeled with the commanded trajectory, followed by the controller used, and then the dynamics model used by the simulation.

5.5.1 Radial Step Response

First a controller was implemented that was designed using the far-field approximation with optimal control techniques as described in section 1.2.2. The far-field gains in 5.4 were tested first in a far-field simulation shown in Figure 5.10. The system was given a step input from x=1.25 to x=1.5.

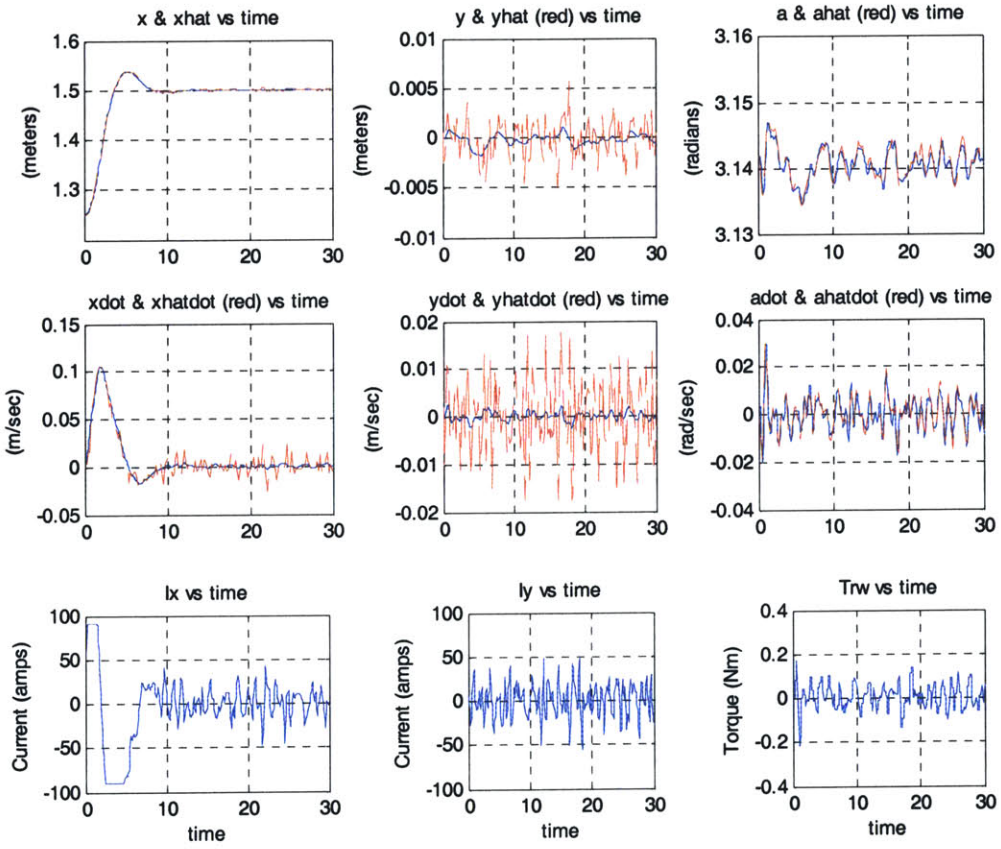

Figure 5.10: Step Response in x, Far-Field Controller, Far-Field Model

The step response has a percent overshoot of 15.2% and a 2% settling time of 7.9 seconds.[12] The other states were kept very close to zero. The maximum error in angle was 0.007 radians. This shows that the system can reject disturbances in the x-direction. To get a better idea of what the response of the actual system would be using a controller based on far field dynamics, the same controller was used with the near field model, shown in Figure 5.11.

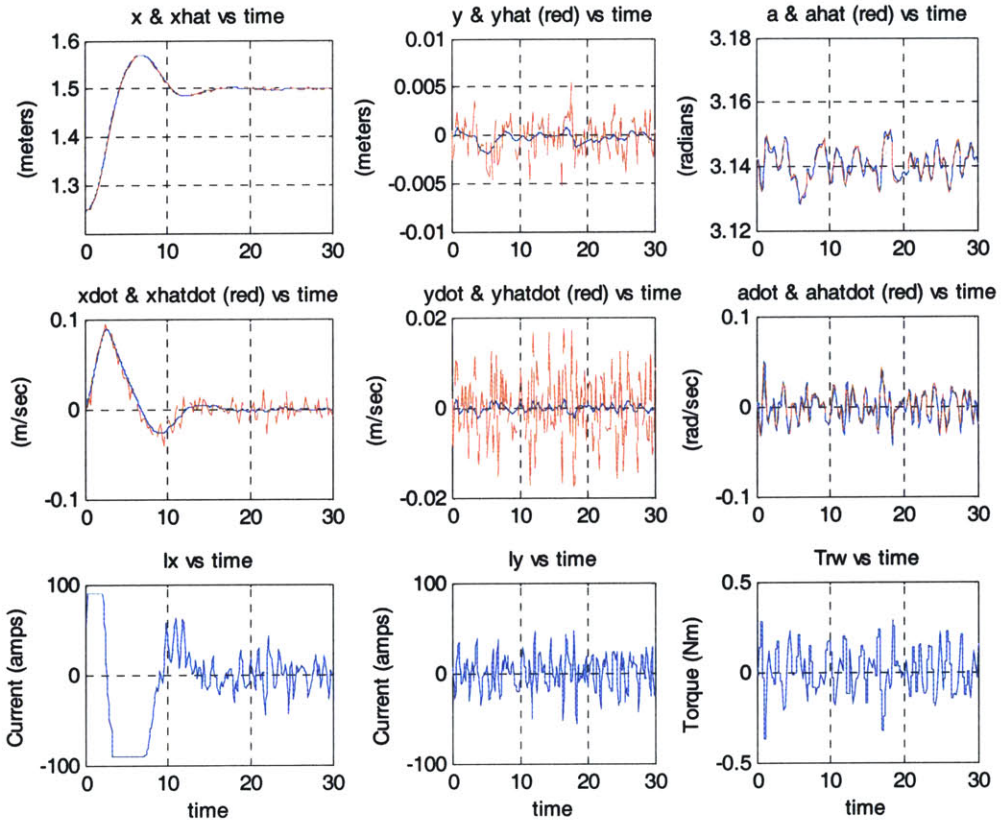

Figure 5.11: Step Response in x, Far-Field Controller, Near-Field Model

In the near-field model the coils do not produce as much force as estimated by the far-field. This results in a slower response and larger overshoot. The vehicle overshoots the desired position in x by 29.0% and takes 14.6 seconds to settle. The largest error in angle is 0.013 radians. This behavior shows that developing a controller using the far-field model will not give the same quality of results in the near-field. Next we will look at the

step response using the near-field model to develop our linearized controller. Figure 5.12 shows the results using the near-field controller with the near-field simulation.

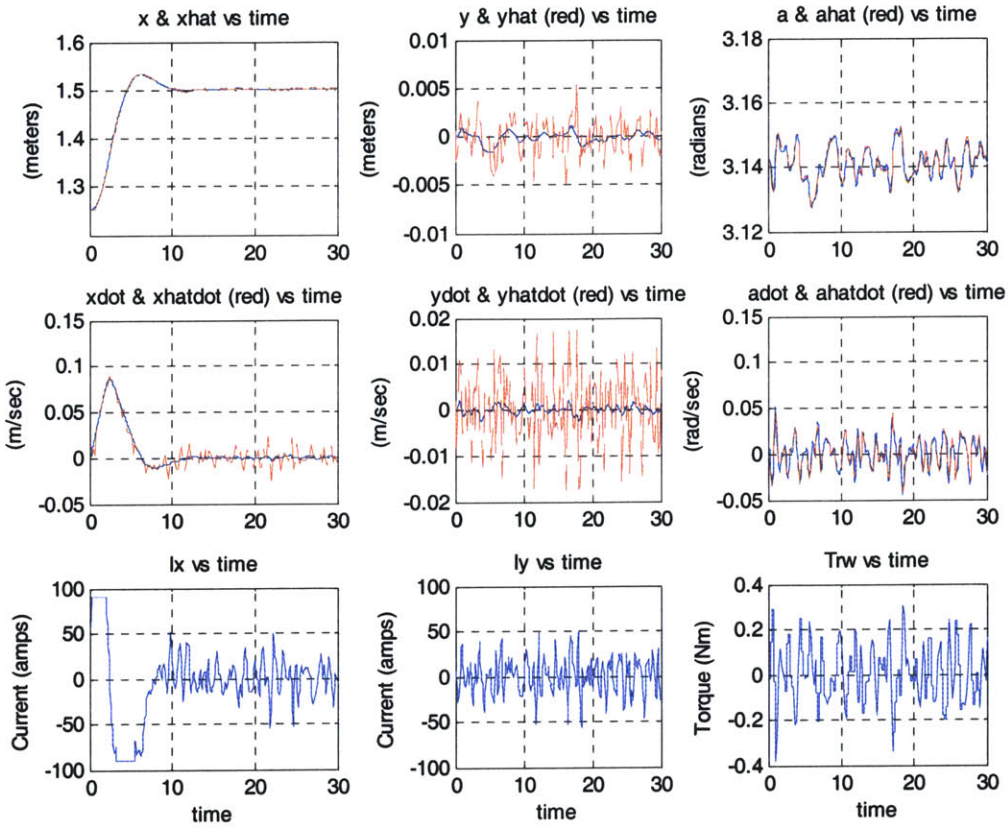

Figure 5.12: Step Response in x, Near-Field Controller, Near-Field Model

The response with the near-field controller is much better than with the far-field controller. Developing the controller with the knowledge of the weaker forces in the near-field allows the controller to produce less overshoot, only 12.4%, and settle to within 2% of the desired position in 9.5 seconds. The largest error in angle does not change much, it is 0.014 radians.

Next, the response using a nonlinear controller as described in section 1.2.4 is implemented. First the controller is tested with the far-field simulation. Figure 5.13 shows the step response to an input of 0.25 meters.

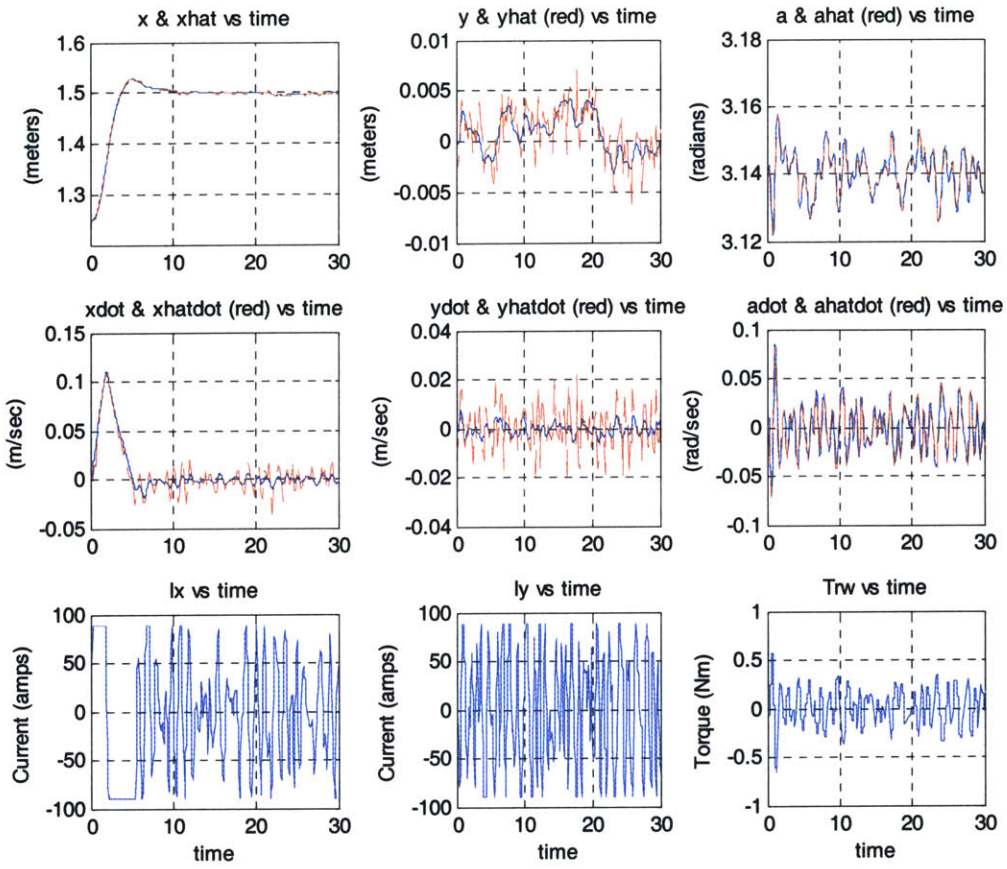

Figure 5.13: Step Response in x, Nonlinear Controller, Far-Field Model

The response has an overshoot of 12.0% and a settling time of 9.8 seconds. This controller also gives good angle control, with a maximum error of 0.019 radians. This response shows that the nonlinear controller has the ability to reject disturbances effectively in the far-field. Next we look at the response using the near-field simulation, in Figure 5.14.

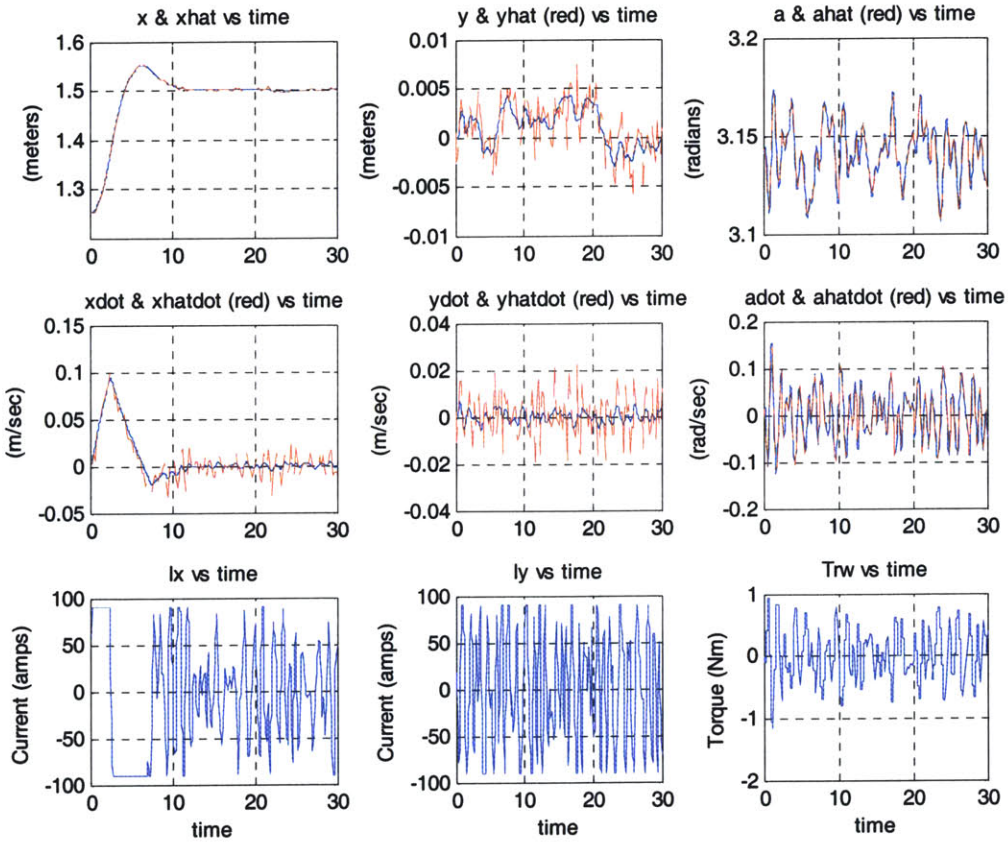

Figure 5.14: Step Response in x, Nonlinear Controller, Near-Field Model

The response with the realistic, near-field simulation has 20.4% overshoot and a settling time of 10.6 seconds. The angular control is on par with the linearized controllers, with a maximum error of 0.034 radians. The nonlinear controller has much more overshoot than the linear controller. It also uses more control switching.

5.5.2 Shear Step Response

It is also necessary to demonstrate the ability of the EMFF concept to provide disturbance rejection perpendicular to the radius between the vehicles. In this section we apply a step input of 0.2 meters in the y-direction. First we look at the response of the far-field controller using the far-field simulation, shown in Figure 5.15.

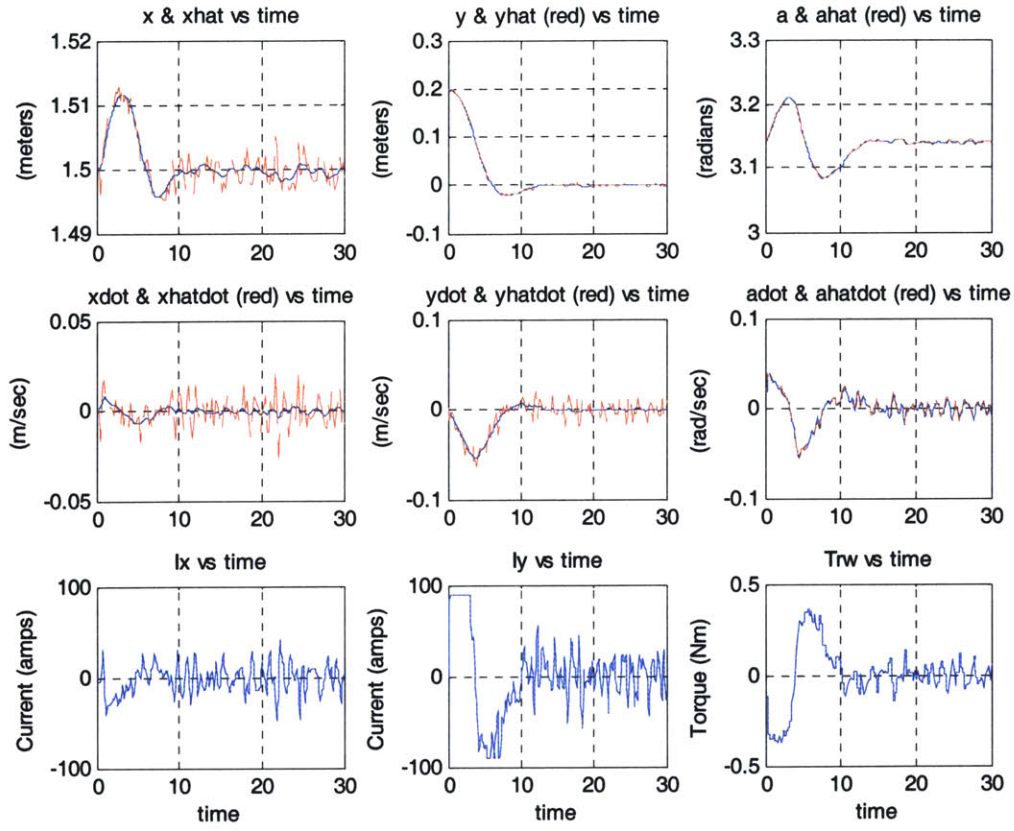

Figure 5.15: Step Response in y, Far-field Controller, Far-field Model

The response has an overshoot of 9.4% and a settling time of 11.6 seconds. Controlling y-position also introduces error on the x-position and alpha states. The x-position experiences a maximum error of 1.2 centimeters and the angle is disturbed by 0.071 radians. Even with this error, this simulation shows that the system is able to reject rather large disturbances in the shear direction. Next we test the same input and far-field controller using the near-field model (Figure 5.16).

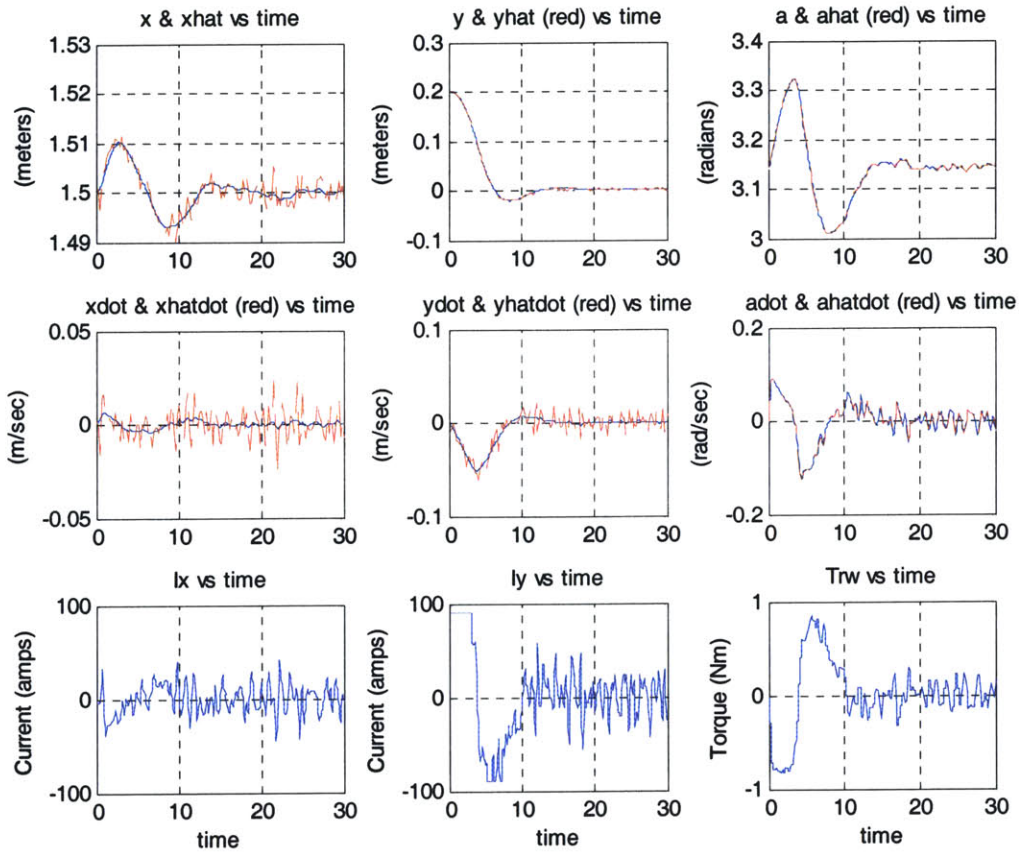

Figure 5.16: Step Response in y, Far-Field Controller, Near-Field Model

As expected, the response in the more realistic simulation is slower. The overshoot is 11.0% and settling time is 12.0 seconds. X-position error is 1.0 centimeters and the angle is disturbed to 0.178 radians. Next we look at the controller developed using the linearization of the near-field model (Figure 5.17).

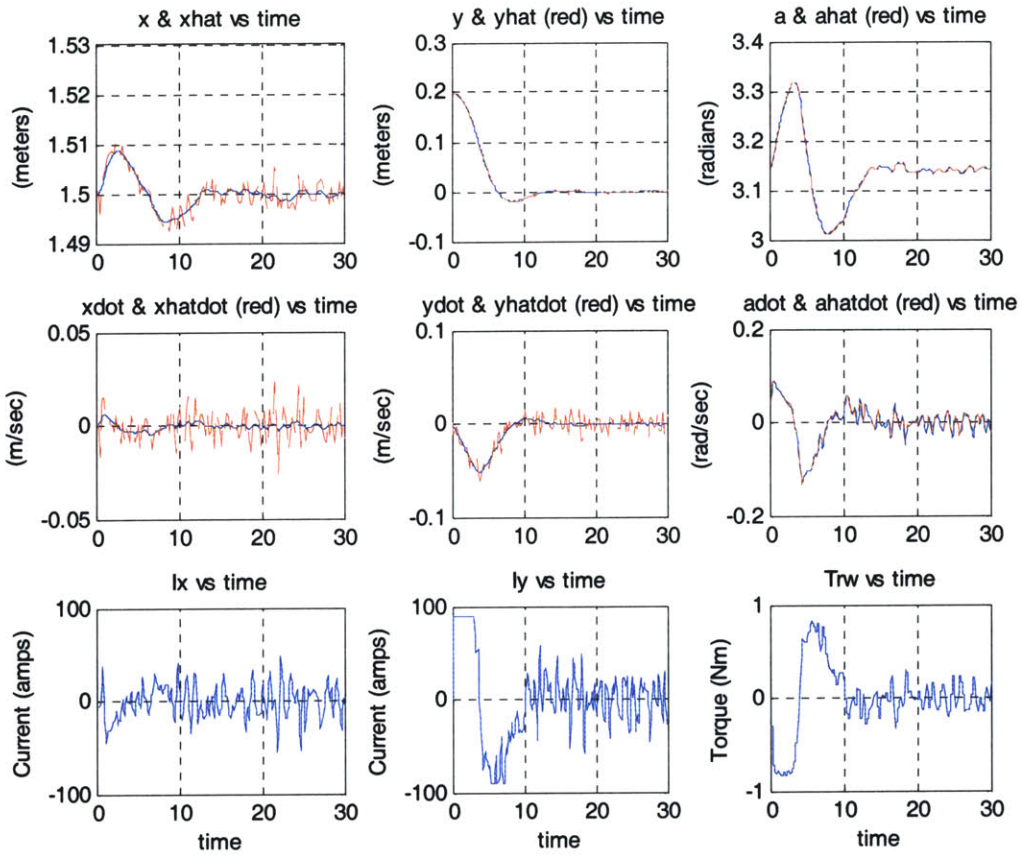

Figure 5.17: Step Response in y, Near-Field Controller, Near-Field Model

The near-field linear controller gives a slightly better response in the y-direction. The overshoot is less at 9.4% and settling time is still 12.0 seconds. This is most likely because both controllers call for very large commands in the y coil to fight the large error in y, because more current is needed to produce shear forces than radial forces. Error in x-position is 0.9 centimeters and in 0.178 radians in angle.

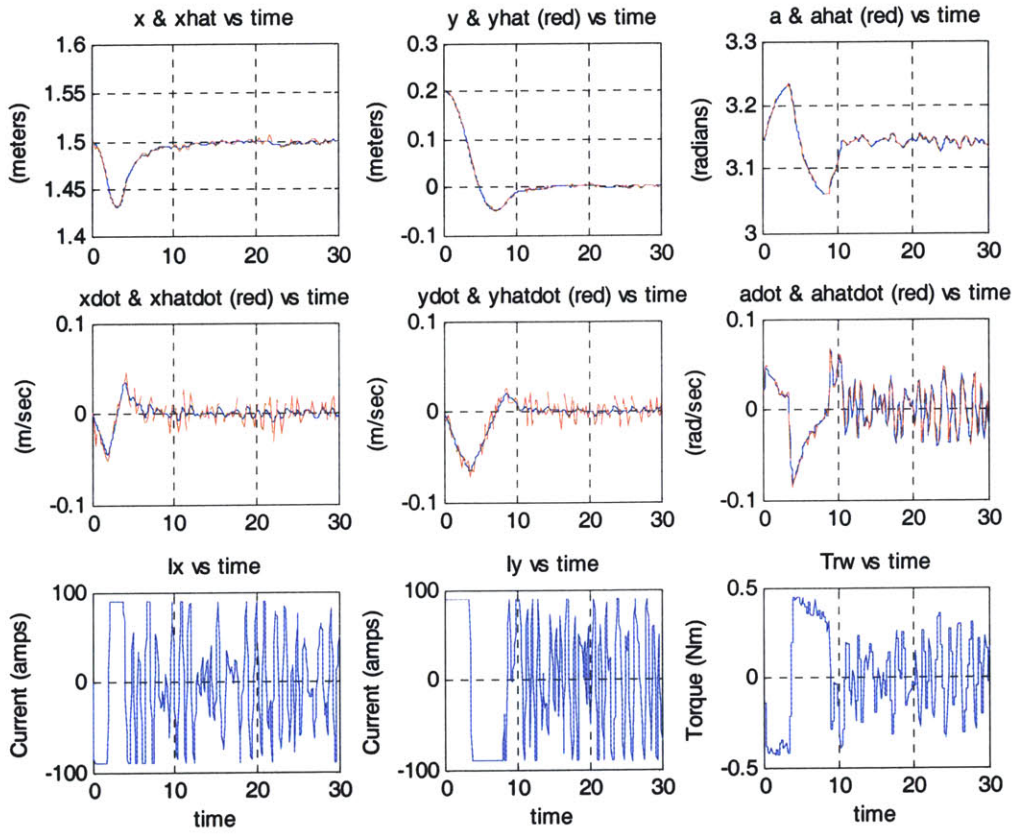

Figure 5.18: Step Response in y, Nonlinear Controller, Far-Field Model

The nonlinear controller also gives a stable response (Figure 5.18), but not as good as the linear controller. In the far-field model, the overshoot is 25.1% and settling time is 14.3 seconds. The x-position error is 6.9 centimeters and angular error is 0.091 radians. Although the position error is greater using the nonlinear controller, the angle is kept closer to its desired value.

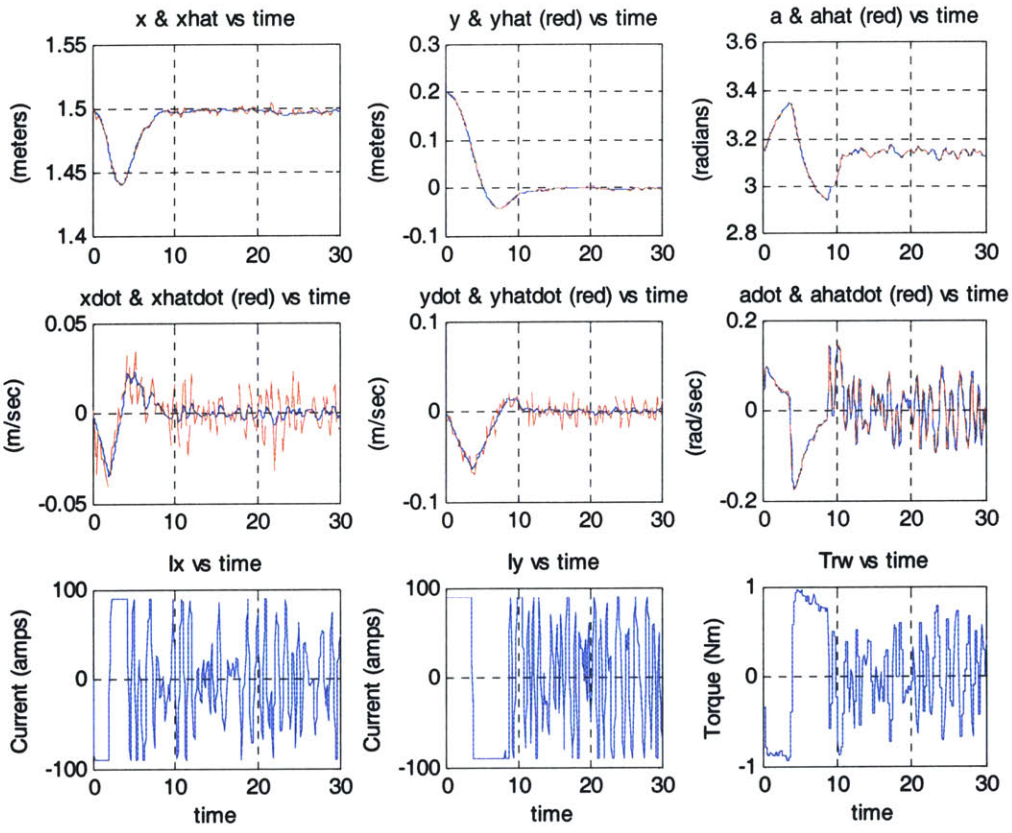

Figure 5.19: Step Response in y, Nonlinear Controller, Near-Field Model

The response using the near-field simulation is slower, with less overshoot, but the settling time is the same as in the far-field simulation. Overshoot is 20.9% and settling time is 14.3 seconds. The error in x-position is 5.8 centimeters and in angle it is 0.210 radians.

5.5.3 Radial Trajectory

The system's ability to move in any trajectory will be shown by demonstrating its ability to follow a radial trajectory and shear trajectory separately. This section will describe the system's response to a commanded sinusoid trajectory with frequency of 0.2 rad/sec and amplitude of 0.25 meters. Since we are interested primarily in the response of the real system, we will only investigate the linear controller designed using the near-field model as well as the sliding mode controller, both using the near-field model for simulation.

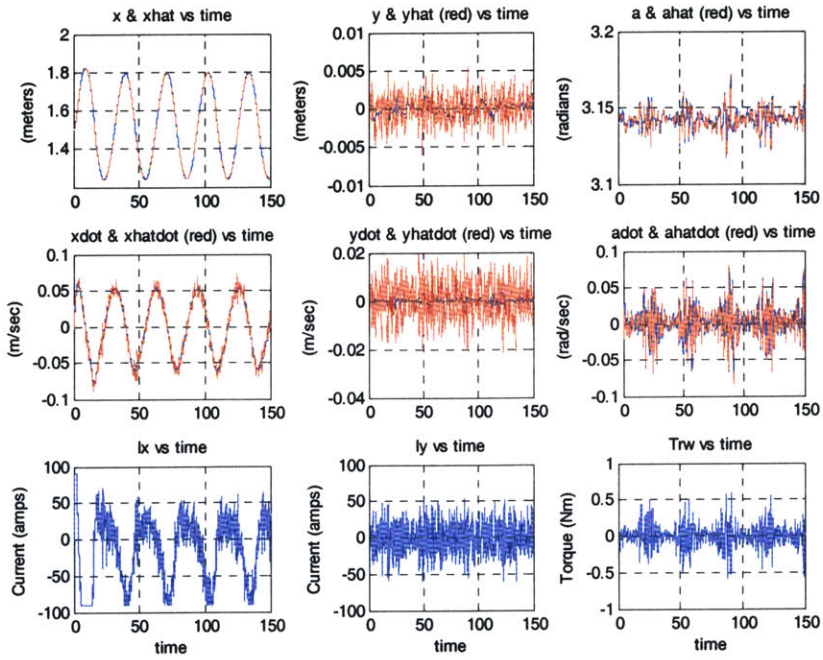

Figure 5.20: Linear Controller, Near-Field Model Sinusoid in x

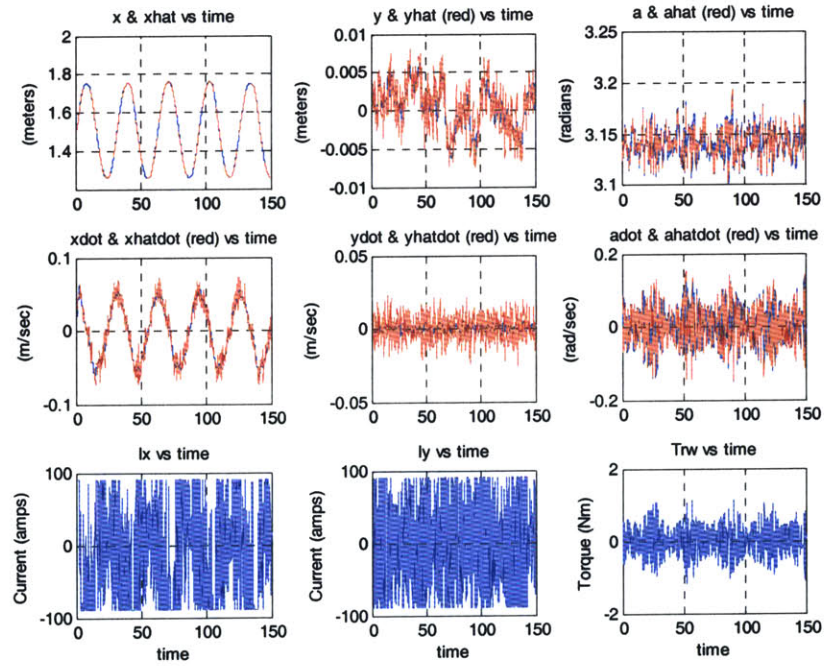

Figure 5.21: Nonlinear Controller, Near-Field Model, Sinusoid in x

Both controllers cause the vehicle to follow a sinusoidal trajectory. It is interesting to note that the nonlinear controller uses much more control switching than the linear controller. Next, we will look at the error from the desired trajectories in each case.

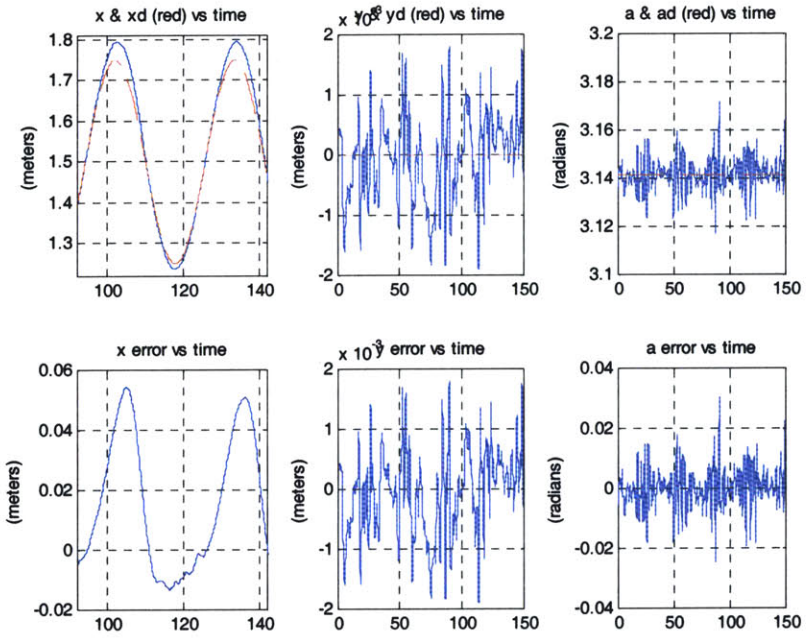

Figure 5.22: Linear Controller, Sinusoid in x error

The linear controller overshoots the commanded sinusoid at both extremes. The phase of the sinusoid does not lag noticeably. There is more error at the peak of the sinusoid, 5.4 cm, which makes sense since the linear controller does not account for the drop in magnetic force as separation distance increases. The error is smaller, 1.3 cm, close to the stationary coil where more force is experienced than expected. The sinusoid in the radial direction introduces very small error in the y direction and in angle.

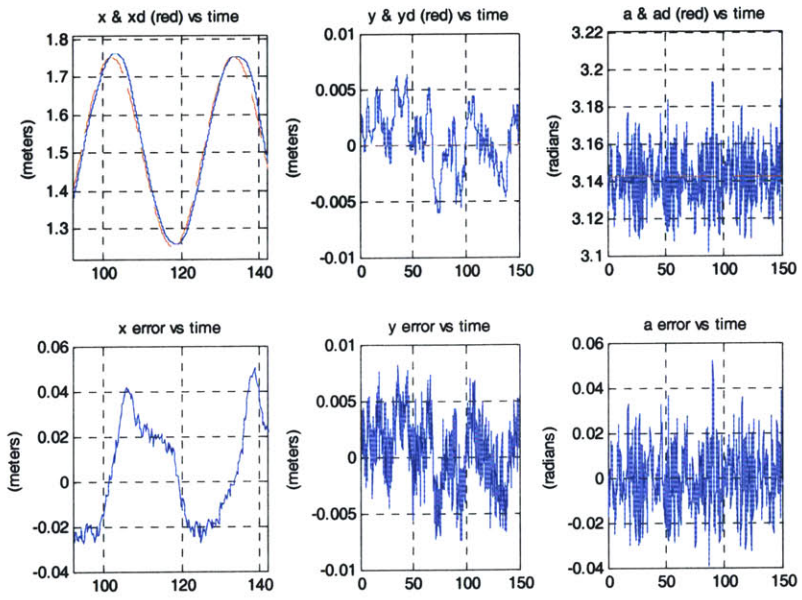

Figure 5.23: Nonlinear Controller, Sinusoid in x error

The nonlinear controller matches the magnitude of the commanded sinusoid very well, but lags it slightly. The response lags more at the largest distance from the stationary vehicle, which introduces 5.0 cm of error. At the trough of the sinusoid, the sinusoid tracks more closely with an error of 2.7 cm. The y and angle errors introduced are very small.

5.5.4 Shear Trajectory

To evaluate the system's ability to follow a trajectory in the shear direction, a sinusoid will be commanded with frequency of 0.2 rad/sec and amplitude of 0.2 meters.

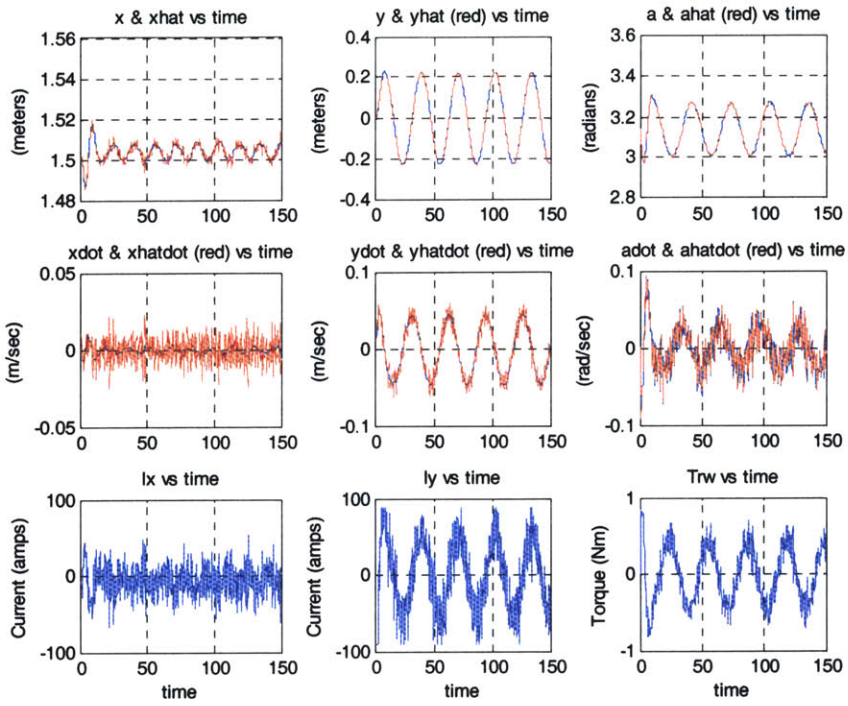

Figure 5.24: Linear Controller, Near-Field Model, Sinusoid in y

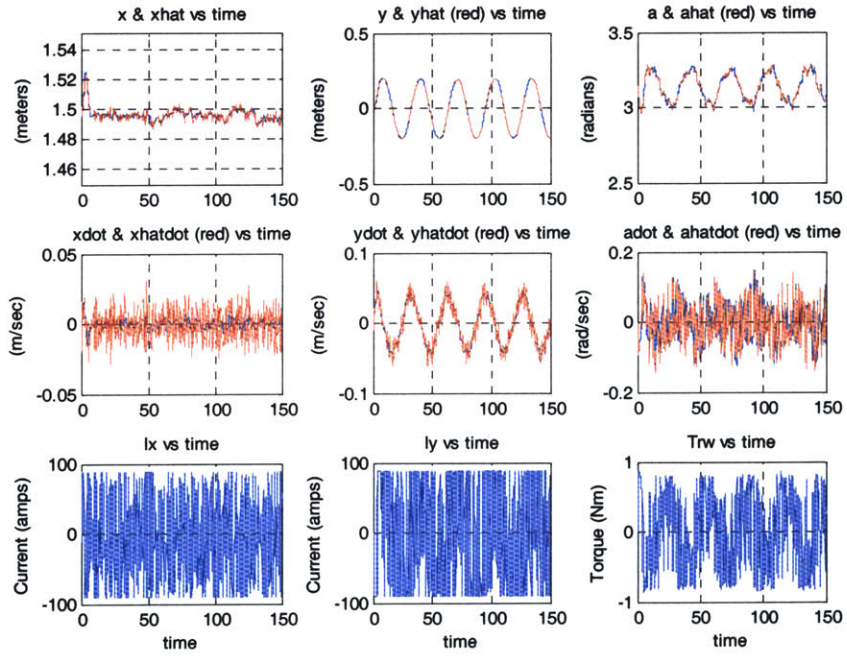

Figure 5.25: Nonlinear Controller, Near-Field Model, Sinusoid in y

Both controllers cause the vehicle to follow a sinusoidal trajectory, but they also introduce a sinusoid in x-position and angle, as shown enlarged in Figure 5.26.

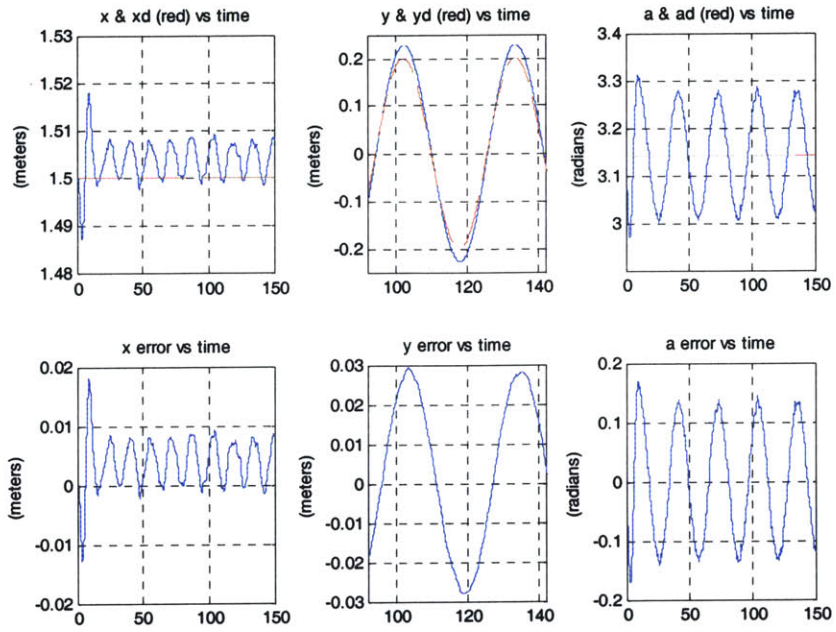

Figure 5.26: Linear Controller, Sinusoid in y error

The linear controller overshoots on both sides of the sinusoid. The maximum error is 2.9 cm. The x-position is pushed slightly off nominal and exhibits a faster sinusoid with maximum error of 0.9 cm. Since applying shear forces also produces torques, the angle also has sinusoidal error with the same frequency as the y trajectory. This error has a maximum of 0.145 radians. The reaction wheel control is designed to keep the vehicle at the nominal angle, but when pure shear forces are applied it cannot completely cancel the magnetic torques experienced. Increasing the gain on angular rate could fight this problem, but given the noise on the testbed, this could create instabilities.

As in the radial trajectory, the nonlinear controller again matches the magnitude of the trajectory very well, but slightly lags. The error has a maximum in steady-state of 3.3 cm due to this lag. The error in x-position is pushed slightly off nominal with and error of

1.2 cm. As with the linear controller, the angle has sinusoidal error with amplitude of 0.164 radians.

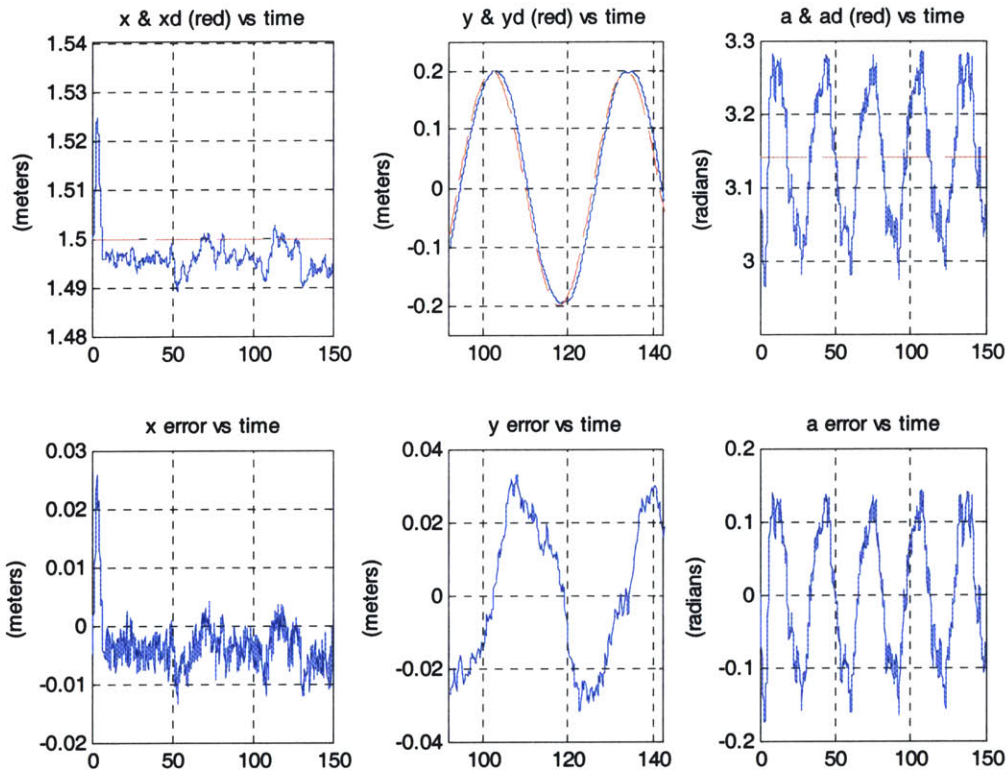

Figure 5.27: Nonlinear Controller, Sinusoid in y error

Chapter 6

Experimental Results

The controllers developed with computer simulations in Chapter 5 were implemented on the two-dimensional EMFF testbed in the Space Systems Laboratory. This section will analyze the results of these experiments and compare them with the simulation results. Next, we will examine the results from a modified controller implemented on the testbed. We will then determine how closely our simulation model reflects the actual system and make changes to the model to make it more accurately predict the dynamics of the testbed.

6.1 Original Controller Step Response

The simulations in Chapter 5 yielded controllers that could stably hold position and follow trajectories. These control algorithms were programmed into the EMFF vehicle computers and implemented on the test hardware. We will primarily investigate the step responses using the linear quadratic regulator described in Section 5.3. Since the linear controller used in the simulations of Chapter 5 overshot the desired state and saturated the commanded current, a second linear controller was implemented with lower gains. It was created using the same technique as the original controller, but with a control cost magnified by a factor of ten. To make the cost of using control more expensive, each element of the control weighting matrix, R, was multiplied by 10. We will refer to this new controller as having expensive control and the controller developed in Chapter 5 and evaluated in the simulations as having cheap control. The feedback gains are shown below.

$$K_{cheap} = \begin{bmatrix} 1636.0 & 3147.9 & 0 & 0 & 0 & 0 \\ 0 & 0 & -1670.8 & -3937.2 & 0.00009 & 0.00009 \end{bmatrix} \quad (6.1)$$

$$K_{expensive} = \begin{bmatrix} 542.78 & 1813.2 & 0 & 0 & 0 & 0 \\ 0 & 0 & -549.25 & -2257.4 & 0.00087 & 0.00096 \end{bmatrix} \quad (6.2)$$

6.1.1 Results

To test the step response of the EMFF vehicles, the estimator and controller were started and the moving vehicle was moved to 1.25 meters in the x direction from the stationary vehicle. The coils were then turned on and the controller attempted to bring the vehicle to 1.5 meters of separation in the x direction. To allow for the cleanest possible metrology data, the vehicles were positioned to face each other, so the moving vehicle maintains a constant angle of π radians. The first plot is the x position data using the cheap control gains (Figure 6.1).

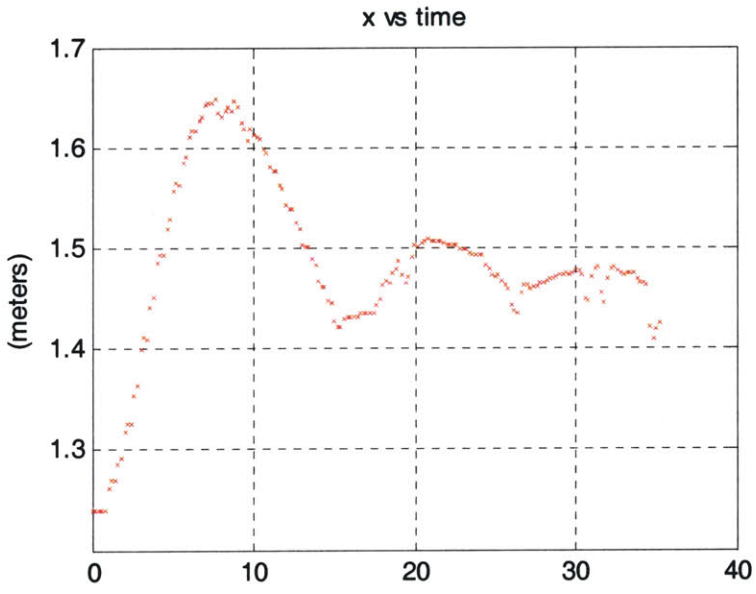

Figure 6.1: x-position Step Response in x, Cheap Control

The vehicle showed a stable response and approached a steady state. The response had 60% overshoot and a 2% settling time of 33 seconds. The position did not level off at 1.5 meters, but approached a steady state of 1.47 meters. This is most likely caused by a slight tilt in the table or by a local deformity. Since the error is not integrated in this full-state feedback controller, it makes sense that steady state error of this form would occur. The rest of the states for this experiment are shown below. Since this controller was optimized for trajectory following (see Section 5.4), it commands very high current when it is far from its nominal position. However, the coils can carry no more than 100 amps of current, so the controller did not get as much authority as it wanted, as seen in the saturated current command in Figure 6.2.

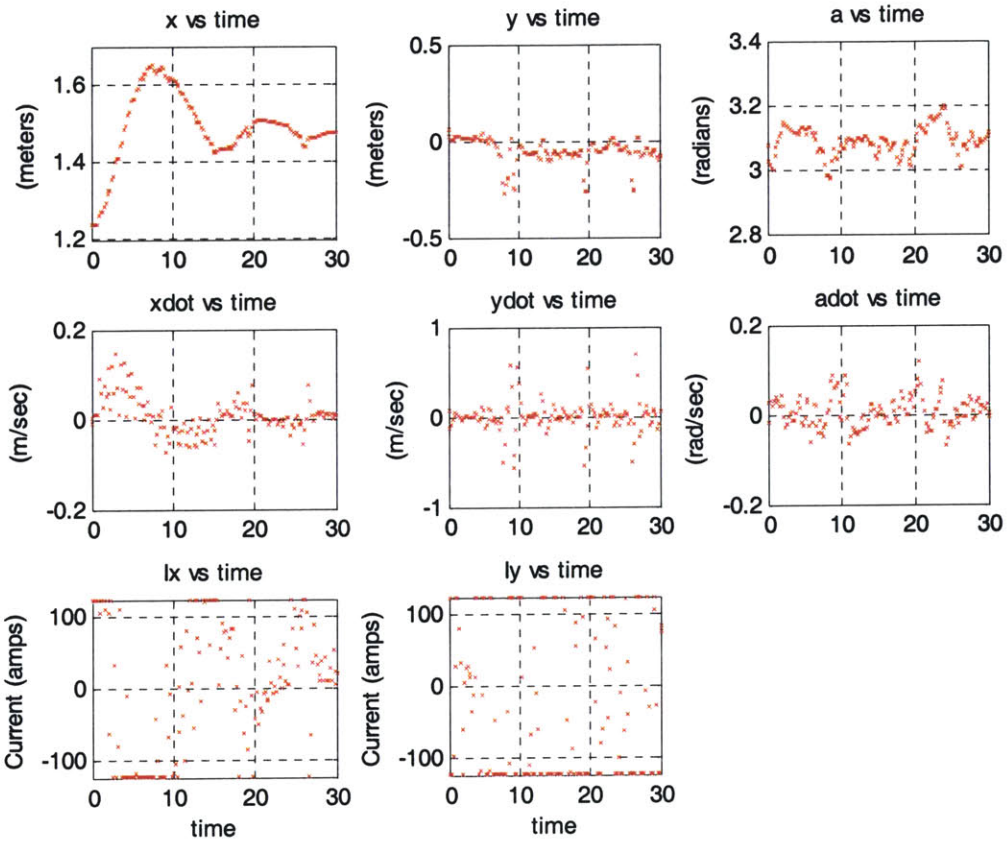

Figure 6.2: Step Response in x, Cheap Control

The same step response was also implemented using more expensive control. It was thought that with lower gains, the response would exhibit less overshoot.

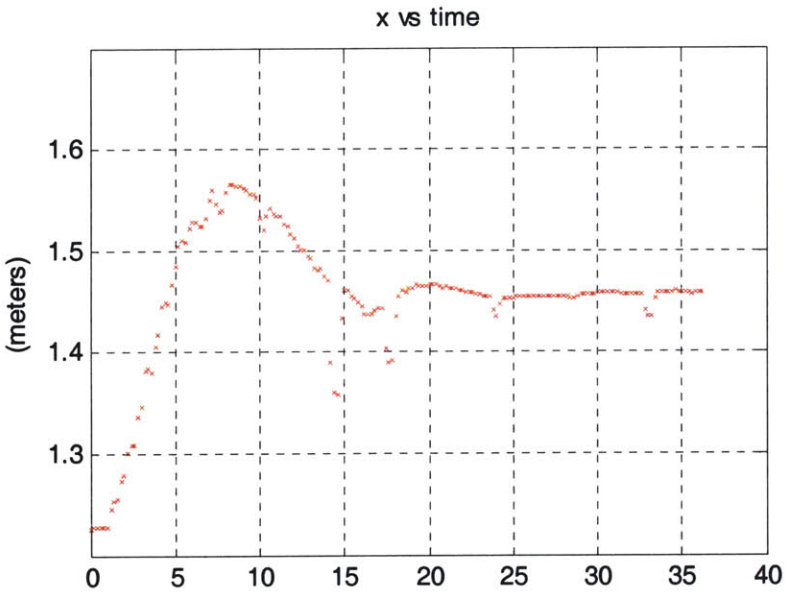

Figure 6.3: x-position Step Response in x, Expensive Control

Increasing the cost of control did bring the overshoot of the response down to 28% and settling time to 27 seconds (Figure 6.3). The vehicle's position goes to a similar steady state error of 1.46 meters. The rest of the state variables are shown below and it can be seen in Figure 6.4 that this controller did not saturate the commanded current as much as the previous controller.

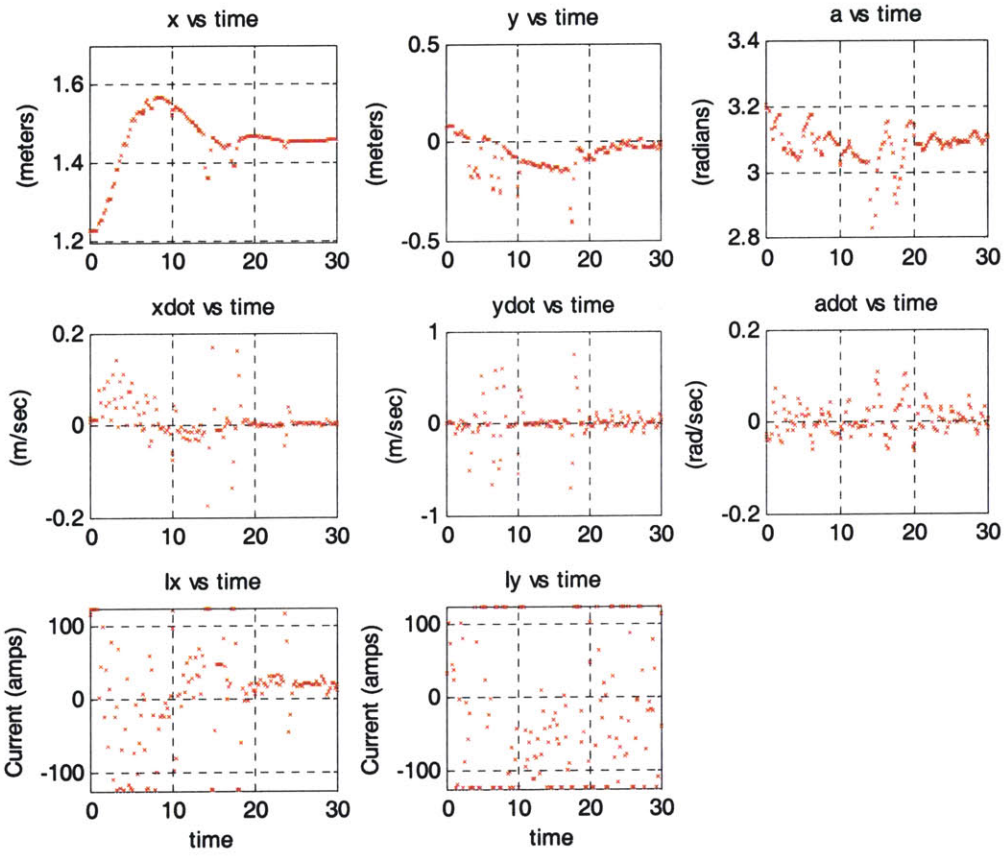

Figure 6.4: Step Response in x, Expensive Control

6.1.2 Comparison with Simulation

Computer simulations were used to predict the response of the experimental hardware. Below are the experimental results plotted with the expected results from the simulation (Figure 6.5, Figure 6.6).

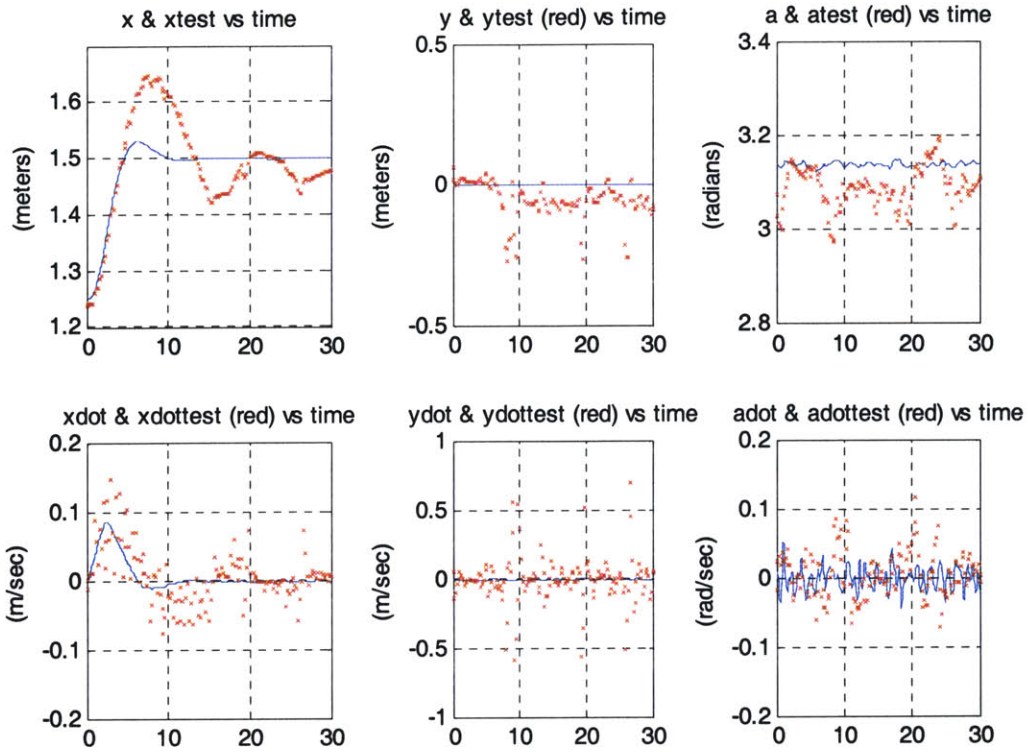

Figure 6.5: Step Response in x, Cheap Control, Simulation and Experimental Results

The behavior of the vehicles was much more oscillatory than predicted by the simulations. Given the modeled dynamics of the system, such large overshoot should not happen. In the real system, there are many outside disturbances that were not modeled that could be contributing to the discrepancy between these behaviors. One obvious disturbance is the slight slope in the table. Although we are able to level the table before a test sequence, we are limited in our precision and working with the vehicles and touching the table may cause slight tilting of the surface.

Another dynamic effect that is not modeled in the simulation used is the friction on the air pucks opposing the motion of the vehicle. There also may be interference of the magnetic field from ferromagnetic materials near the vehicles. The table that the vehicles float has shown ferromagnetic properties and may be distorting the magnetic field of the coils.

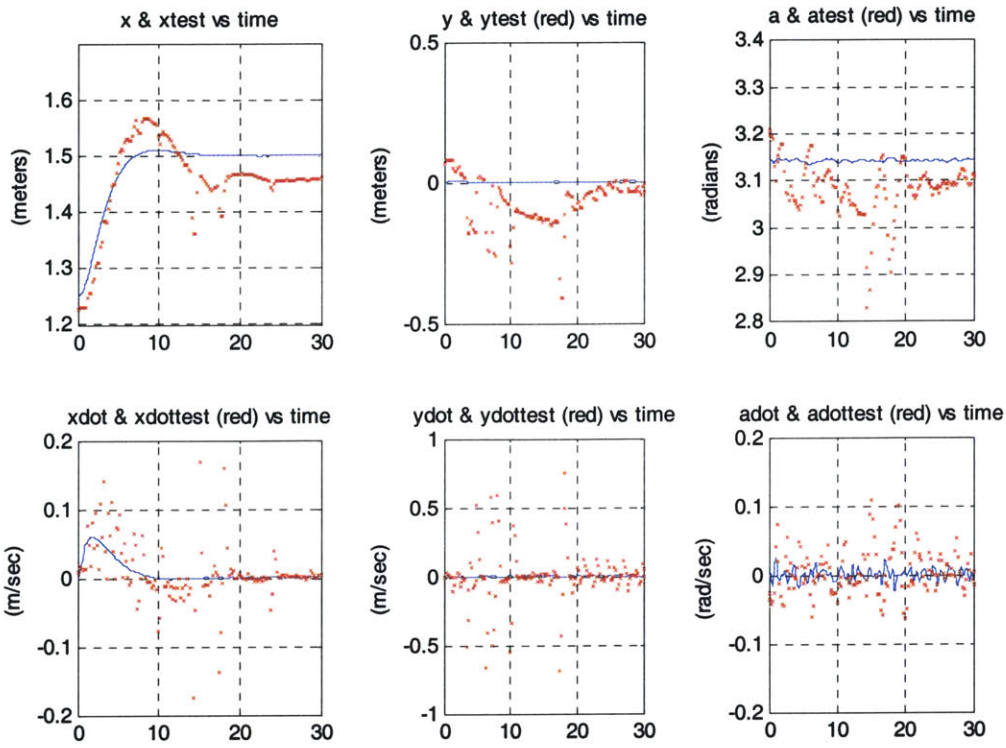

Figure 6.6: Step Response in x, Expensive Control, Simulation and Experimental Results

Other sources of error in our model could come from mismodeling of the system. The mass estimate used may not be as precise as thought and the vehicle mass changes slightly as liquid nitrogen boils off. It is also possible that the model of the current control in the coils has a lower bandwidth than determined in system identification. Problems with metrology are also encountered on the testbed in the form of jumps to bad data points that are not rejected by the filter. This noise is not easily replicated in simulation.

6.2 Modified Controller

The slow settling of the step response using the EMFF vehicles implied that the model used did not completely capture the dynamics of the real system. Although there are many factors contributing to the discrepancies seen, it is possible that the magnetic field

was deformed in some way and resulted in weaker interaction forces than expected. In an attempt to develop a controller that gives a faster, less oscillatory behavior, a new linear quadratic regulator was developed assuming weaker interaction forces between the vehicles. The effect of this assumption was to increase the gains on velocity in both the x and y directions. This can be seen in the gains below. A similar effect would be caused by increasing the weighting on velocity error when developing the controller. This higher weighting should cause the system to respond more slowly, yet with less oscillation.

$$K_{cheap\_modified} = \begin{bmatrix} 1703.3 & 5078.5 & 0 & 0 & 0 & 0 \\ 0 & 0 & -1726.1 & -6327.5 & 0.00036 & 0.00040 \end{bmatrix} \quad (6.3)$$

$$K_{expensive\_modified} = \begin{bmatrix} 555.24 & 2899.6 & 0 & 0 & 0 & 0 \\ 0 & 0 & -559.42 & -3602.2 & 0.00035 & 0.00039 \end{bmatrix} \quad (6.4)$$

The experimental results for these two controllers are shown in Figure 6.7-6.9.

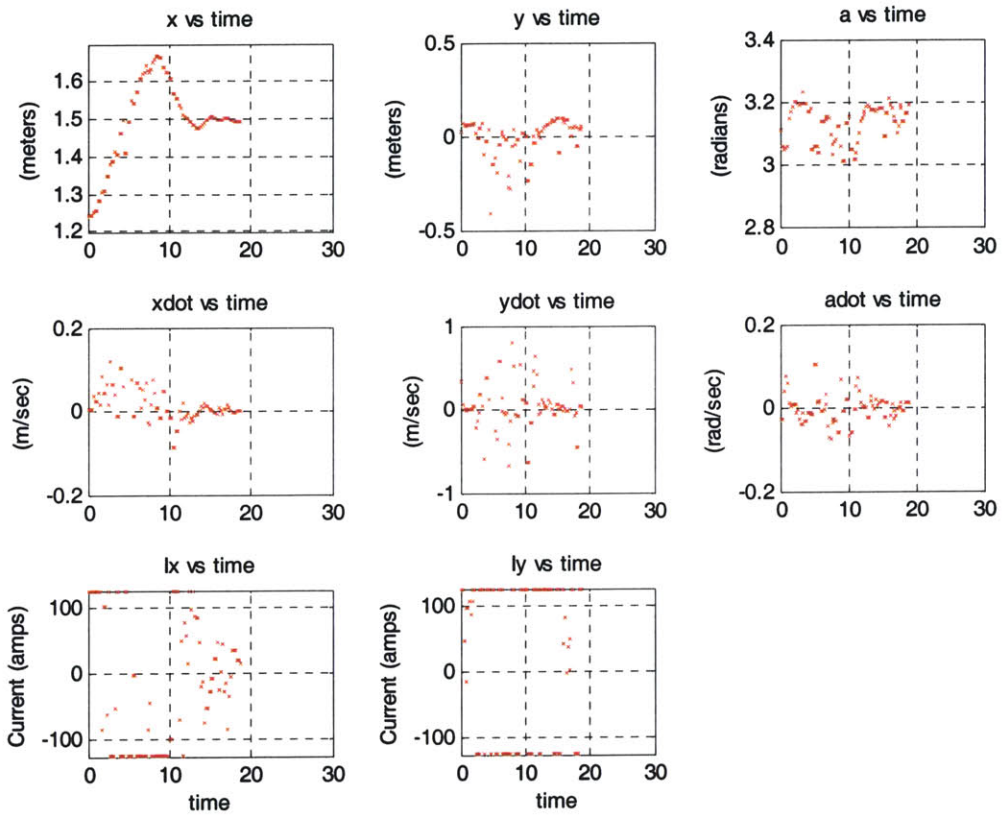

Figure 6.7: Step Response in x, Cheap Control Modified

The gains calculated with a low weighting on control use seem to be too large. This controller gives a step response with 66% overshoot (Figure 6.7). Despite the large overshoot, the settling time is improved in this case to 15 seconds. Next we look at the response using expensive control.

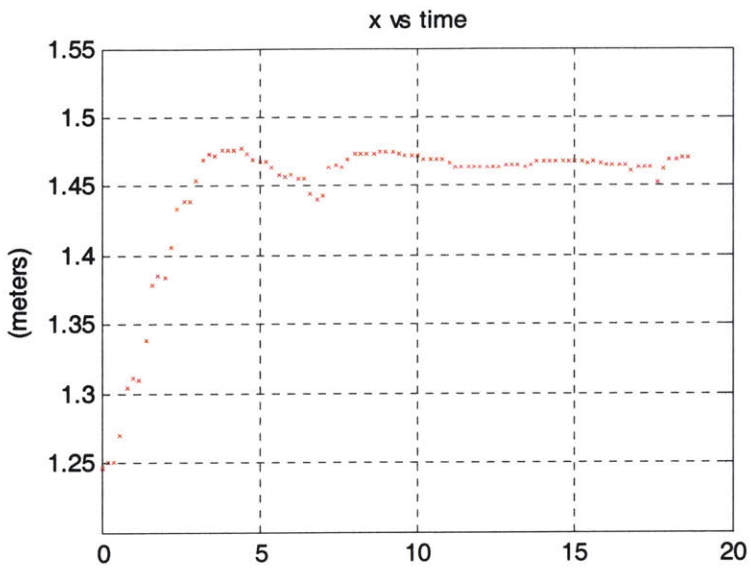

Figure 6.8: x position Step Response in x, Expensive Control Modified

The step response using the modified expensive control does not overshoot the desired position of 1.5 meters and slightly overshoots the steady state of 1.47 meters (Figure 6.8). The settling time to its steady state is 9 seconds. The state and input data in Figure 6.9 shows that this controller rarely saturated the current controller for the x-coil and therefore was able to yield very good behavior.

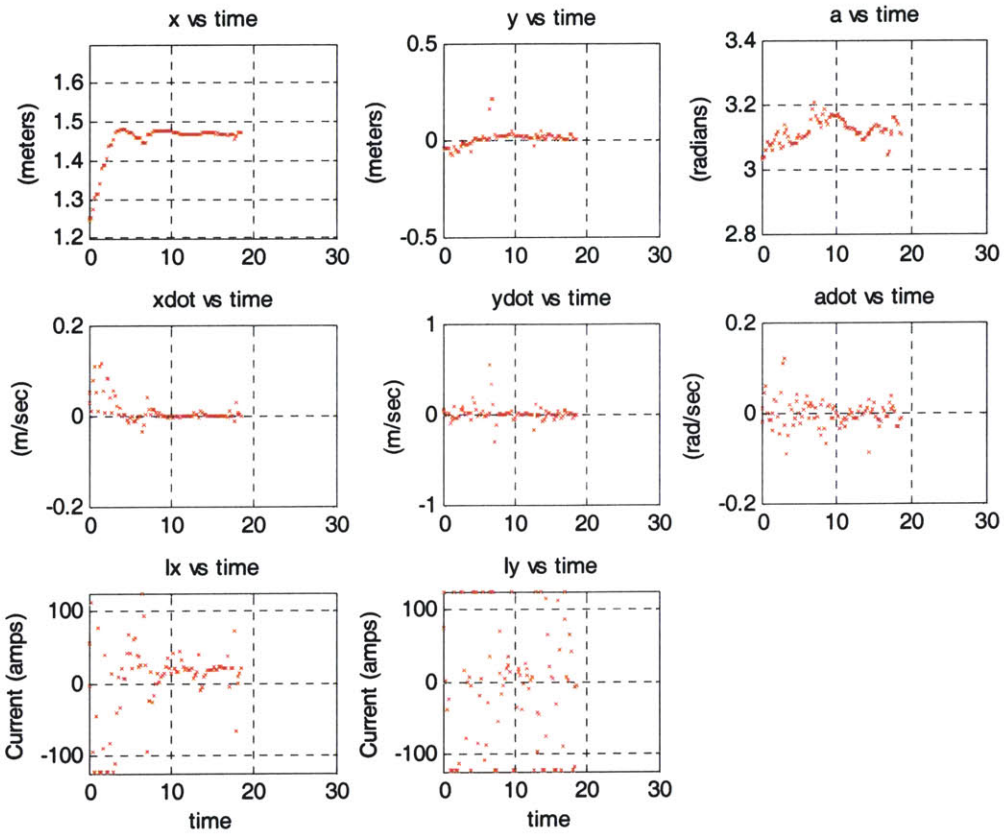

Figure 6.9: Step Response in x, Expensive Control Modified

6.3 Model Fitting

In order to be able to design effective controllers for the EMFF system, the model of the dynamics should be representative of the actual behavior on the testbed. As discussed earlier, there are many possible factors that our simulation may not represent accurately. In this section we attempt to improve our model of the system by varying parameters to fit the data recorded in experiments.

Many parameters are known to be within a small range such that variations within that range will not significantly change the dynamics of the system. The mass of the system is one such parameter. Changing the mass of the system by a few kilograms does not change the dynamics significantly. Other parameters, such as friction, air disturbances,

and local deformations in the table surface are known to be very small and would be difficult to estimate, so they are not modeled in the simulation.

The parameters that are known with the least confidence are those related to the magnetic field. We are able to calculate the exact forces and torques between two coils of wire assuming that they are producing the only magnetic fields of significant magnitude. It is possible that other metal objects are interfering with the magnetic fields of the coils. If the table is becoming magnetized by the electromagnetic coils, it could make the interaction forces weaker or slow the response of the magnetic field as the table is re-magnetized with the changing field. It is also possible that the frequency response of the coil is not as fast as we identified.

The variations of these parameters can be captured in the simulation by introducing a scaling factor on the forces and torques between the coils and by changing the pole, or break frequency, of the frequency response of commanded current in the superconducting coil. The amount of current in the coils enters into force and torque calculations multiplicatively, so slowing the response to commanded current in our simulation can either represent mismodeling of the actuator or a delay in the magnetic field propagation due to interfering magnetic objects.

The effect of the noise in the metrology data on the behavior of the system is not known. It is very difficult to replicate the noise introduced by the metrology system. The noise in the information it gives does not exhibit the characteristics of random white noise, but instead jumps at random times to incorrect measurements. When this jump is large enough to detect as abnormal, the estimator uses the measurement from the previous time step, which introduces velocity error. Since noise representative of that which is generated by the metrology system on the vehicle cannot be generated by our simulation, we will instead look at the simulation's behavior when given the same metrology information that the vehicle's controller was given.

Providing the metrology data from a test run to our simulation will not cause the simulated vehicle to follow the same trajectory as the actual vehicle unless the dynamics of the testbed are exactly modeled in the simulation. Since we know there are some disturbances and dynamics that we cannot model precisely, we can only attempt to get behavior from the simulation that is close to what was seen on the testbed. For example, if there was a slight slope in the table that we conducted our tests on, the actual vehicle would not return to the nominal position, but would reach a position slightly down the slope. If the simulation did not have this slope modeled, it would receive sensor measurements (from the experiment's metrology) telling it to constantly apply a force to fight a slope that didn't exist and it would race off to infinity. For this reason a slope term encapsulating the gravitational acceleration from a tilted table was introduced to the dynamic model. The slope terms g_x, g_y are gravitational acceleration times the angle of slope, $g \cdot \sin(\theta_{slope})$.

$$\begin{bmatrix} \ddot{x}_M \\ \ddot{y}_M \\ \ddot{\alpha}_M \end{bmatrix} = \begin{bmatrix} \frac{F_x}{m_M} + g_x \\ \frac{F_y}{m_M} + g_y \\ \frac{T_z + T_{rw}}{I_M} \end{bmatrix} \tag{6.5}$$

In order to find the appropriate parameters for a given test run, we must match the motion of the simulated vehicle as closely as possible with the behavior of the actual vehicle. Completing this task required running the simulation using the experimental metrology data at every combination of the varied parameters until the best combination was found. The goal of this procedure was to find the scaling factor for the calculated forces and torques as well as the actual pole location for the effective magnetic field propagation, which could be a result of coil dynamics. In addition to providing a range of scaling factors and pole locations, this procedure also required providing a range of initial conditions for the vehicle position close to what the metrology had measured, as well as a range of slope terms in the x and y directions.

An example of a model fitted to the experimental results is shown below. It corresponds to the test run with the modified cheap control. It is interesting to note that the x velocity cuts through what looks like the average of what the estimator calculated as the velocity of the vehicle using the noisy metrology data. It was especially difficult to fit the simulation to the y data because it has so many jumps in value. The other fitted models can be found in APPENDIX B.

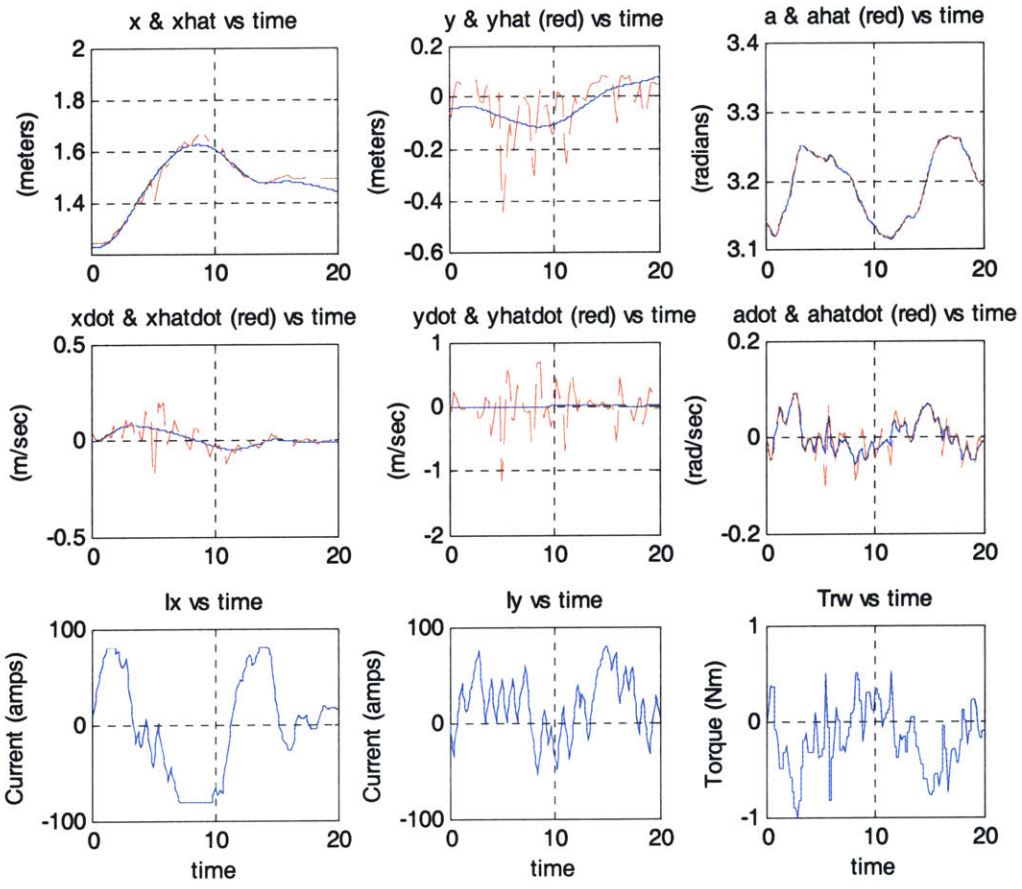

Figure 6.10: Model Fitted to Step Response in x using Cheap Control Modified

To evaluate how closely a simulation with a given set of parameters fit the experimental data, the error between the two trajectories was squared and added at each time step, with a larger weighting on error in the x direction. The combination of parameters with the

lowest total error was then determined. Below are the best values for the scaling factor and pole location for the four tests discussed previously.

Table 6.1: Best Fit Parameters

Controller	Scaling Factor	Pole Location (rad/sec)
Original Cheap Control	1.0	1.1
Original Expensive Control	0.85	0.8
Modified Cheap Control	1.0	0.8
Modified Expensive Control	1.0	0.8

Most test runs were fit best using a scaling factor of 1.0 and a pole location of 0.8. In each case that was not optimized with these common values, it was checked what the change in behavior would be if the scaling factor of 1.0 and a pole location of 0.8 was used. In both cases, there was a set of parameters including these values with slightly more error than the best case. From this procedure we can conclude that the dynamics of the EMFF testbed are best approximated by using the full forces and torques that are calculated by the near-field model and by modeling the coil dynamics as having a pole at 0.8 rad/sec. This means that either the frequency response of the commanded current rolls off in magnitude much earlier than expected or the table or some other ferromagnetic material is slowing down the responsiveness of the magnetic field due to the coils.

6.4 Comparison of Experimental Results with Modified Simulation

The reason for fitting the model used in our simulation to the actual data is so that we can predict the behavior of the actual system. With an accurate simulation, we can develop and evaluate control algorithms without needing to execute tests using the hardware. We can then use the EMFF vehicles to validate the control developed. This section will compare the simulation running on its own with what we observed on the testbed. The

model was developed using metrology data from the experimental tests, but this section will investigate what the modified simulation would predict without any outside input. The simulations were first run assuming that the table was completely flat. Figure 6.11 shows the results using the first controller developed using cheap control

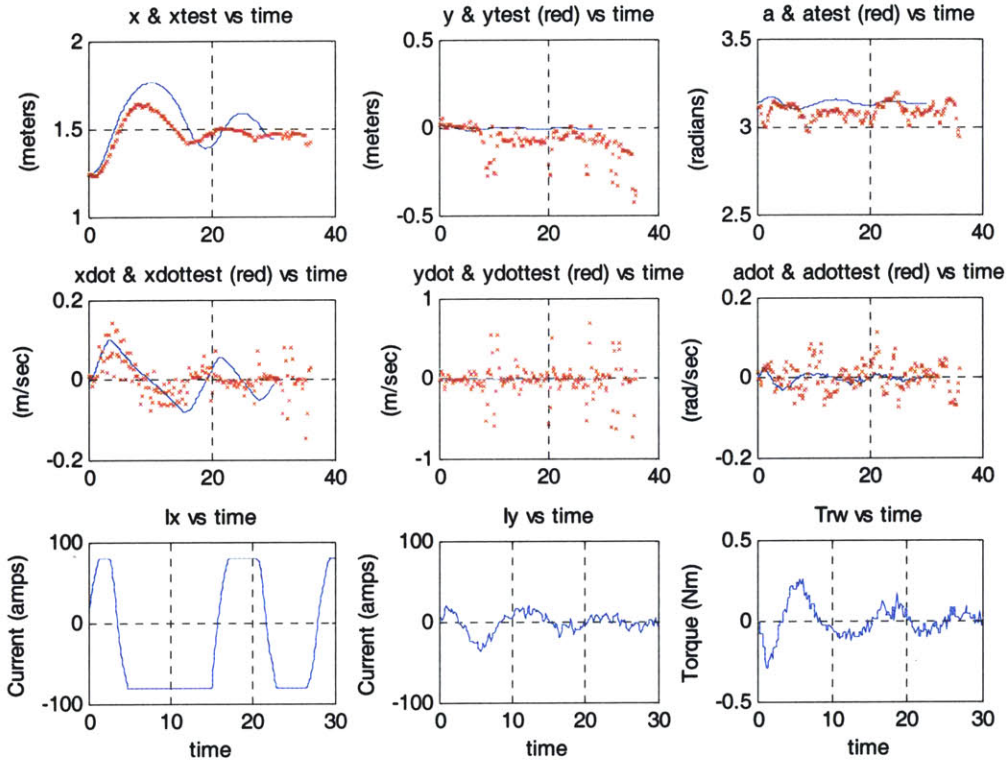

Figure 6.11: Step Response in x, Cheap Control Original, Modified Simulation

The modified simulation predicts results that exhibit oscillation similar to what occurred during the test. Changing the effective dynamics of the magnetic field by modeling the superconducting coil as having a slower response seems to have increased the accuracy of our model. Even though the predicted results from this simulation are similar to the experimental results, the behavior is not identical. One reason that the results shouldn't match completely is that the simulation assumes a perfectly flat table, which we can tell is not accurate from the presence of steady state error and the tendency of the vehicle to drift in the negative y direction. Figure 6.12 shows the same simulation, but with a slope term added to match the experimental data.

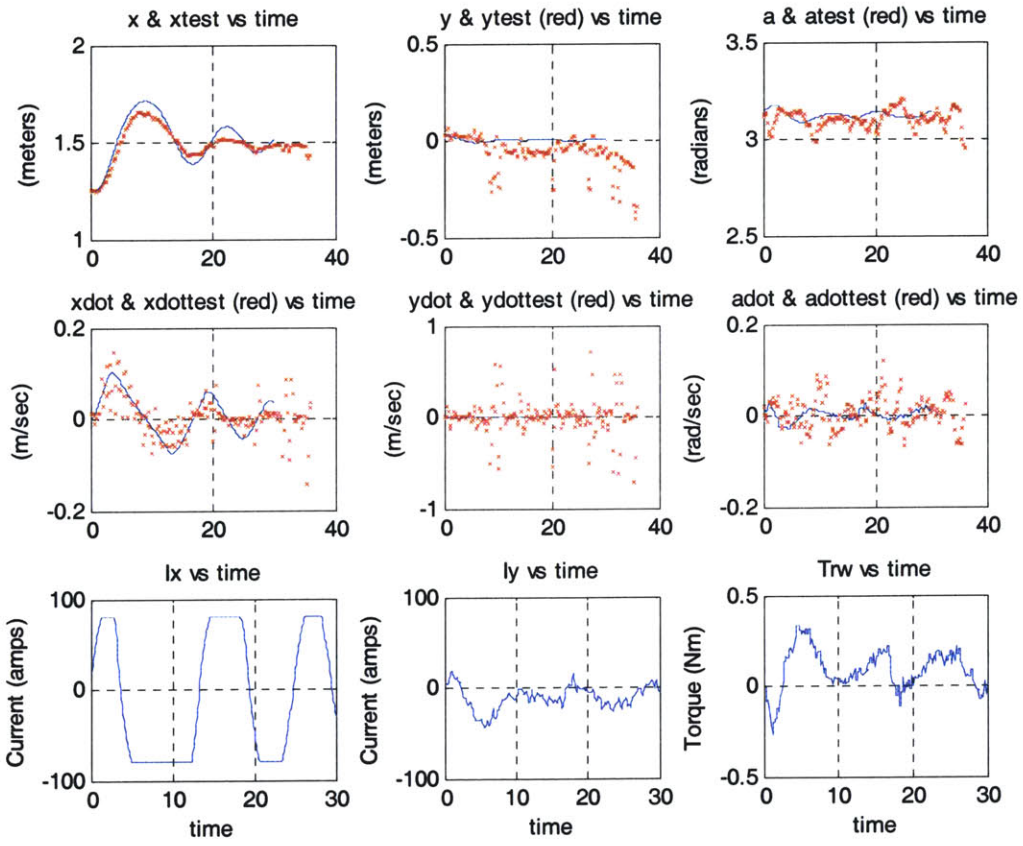

Figure 6.12: Step Response in x, Cheap Control Original, Modified Sim with Table Slope

The results from the simulation with the table slope included in the model give results much closer to what was seen in the experiment. Next we look at what the modified simulation would predict for the behavior using the original expensive control gains in Figure 6.13.

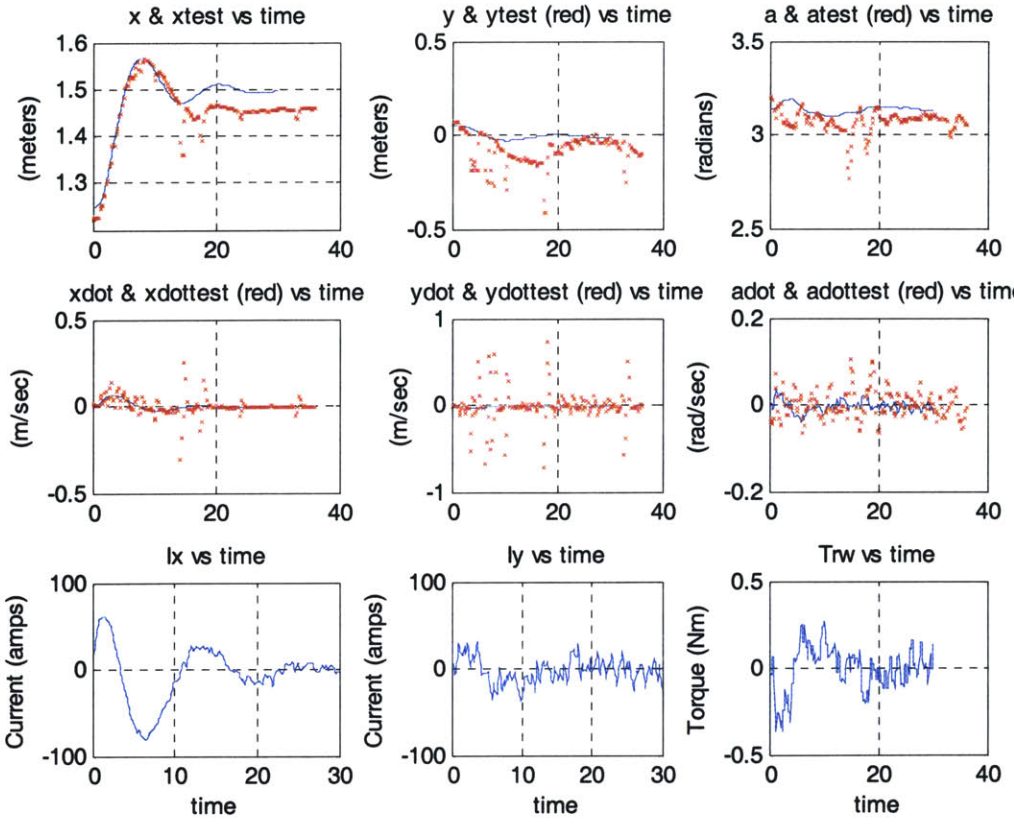

Figure 6.13: Step Response in x, Expensive Control Original, Modified Simulation

The simulation predicts almost identical results, except that since it assumes the table is flat it approaches the commanded position of 1.5 meters. Figure 6.14 shows the results when a slant is added to the dynamics model.

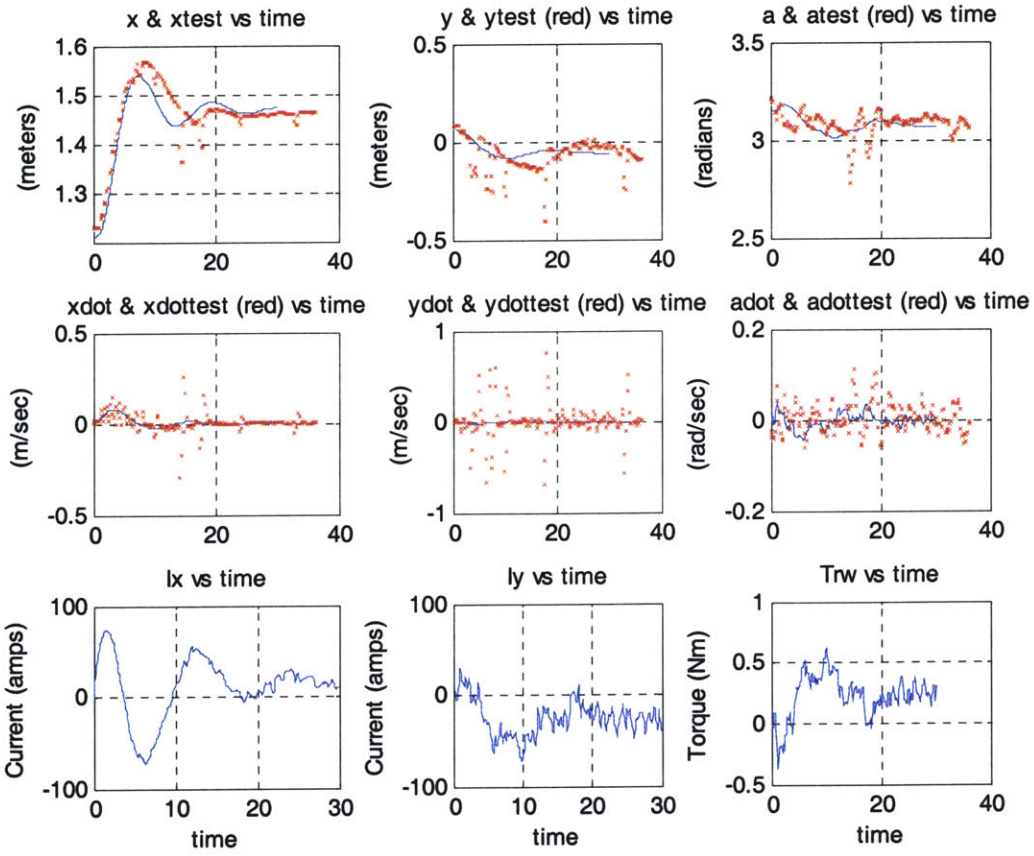

Figure 6.14: Step Response in x, Expensive Control Original, Modified Sim with Table Slope

The added slope causes the x position of the vehicle in the simulation to approach the same steady state as the test vehicle. The y positions also follow each other much more closely. The first peak of the response is lower in the simulation with a slant, which could imply that the table may not have a uniform slope. Next we will examine the results using the modified controller developed in Section 6.2.

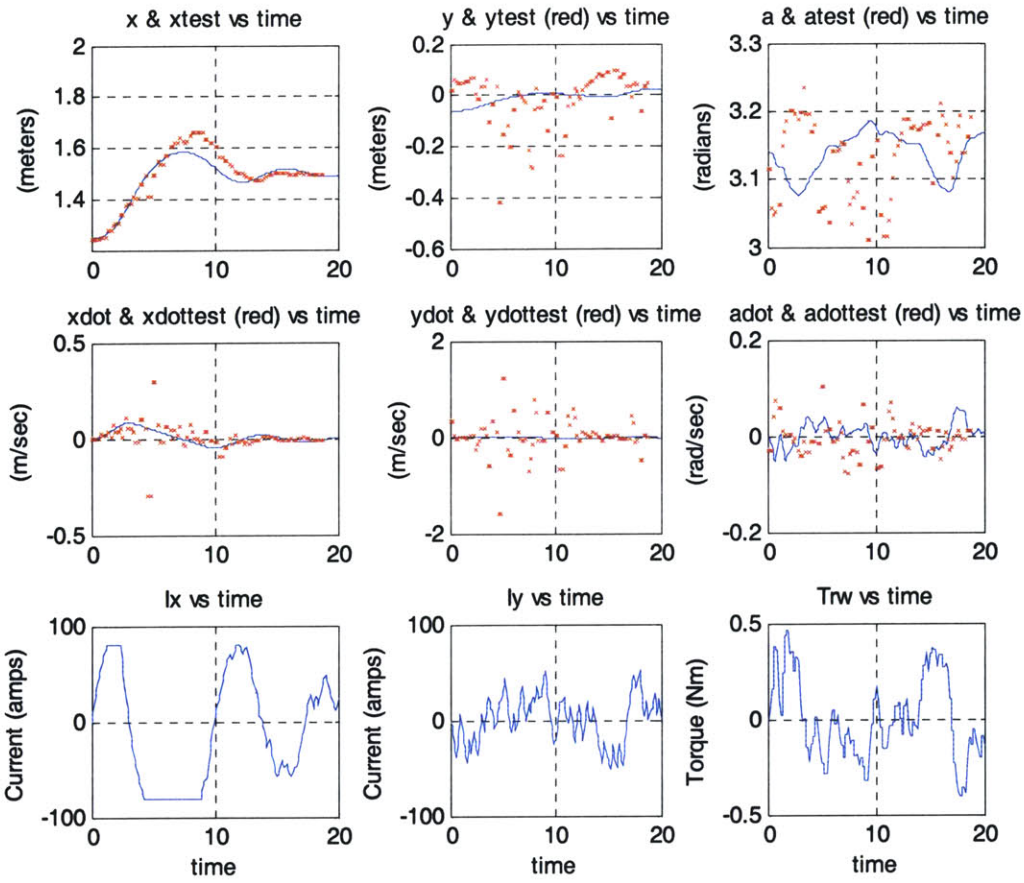

Figure 6.15: Step Response in x, Cheap Control Modified, Modified Simulation

Figure 6.15 shows the step response that the simulation predicted using cheap control from the modified controller. The behavior has the same shape as the actual response, but it does not reach the same peak. It is likely that the actual vehicle did not begin the test at exactly 1.25 meters, as assumed in the simulation, but its initial conditions could have been slightly closer to the stationary vehicle where force is higher. Figure 6.16 shows the results of lowering this initial condition.

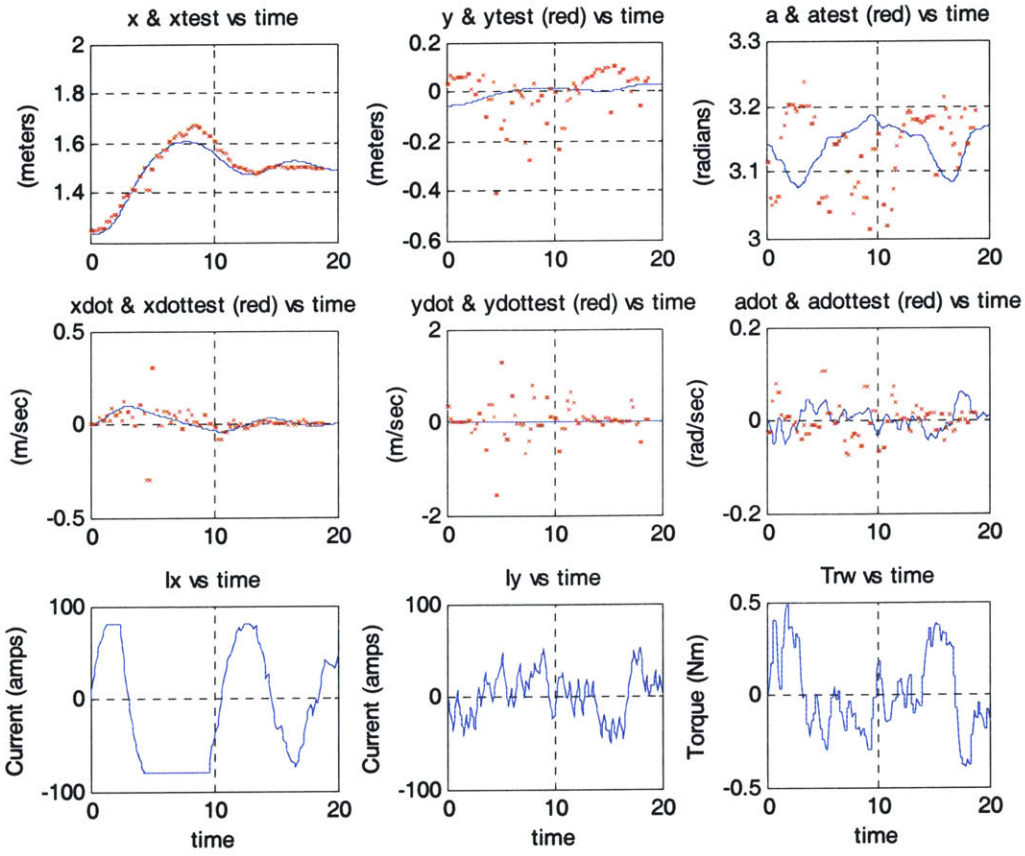

Figure 6.16: Step Response in x, Cheap Control Modified, Modified Sim with Initial Cond

Changing the initial conditions by only a few centimeters made the simulated response match the experimental data more closely. Next we will look at the step response of the only controller that did not exhibit any overshoot, using the modified expensive control weight.

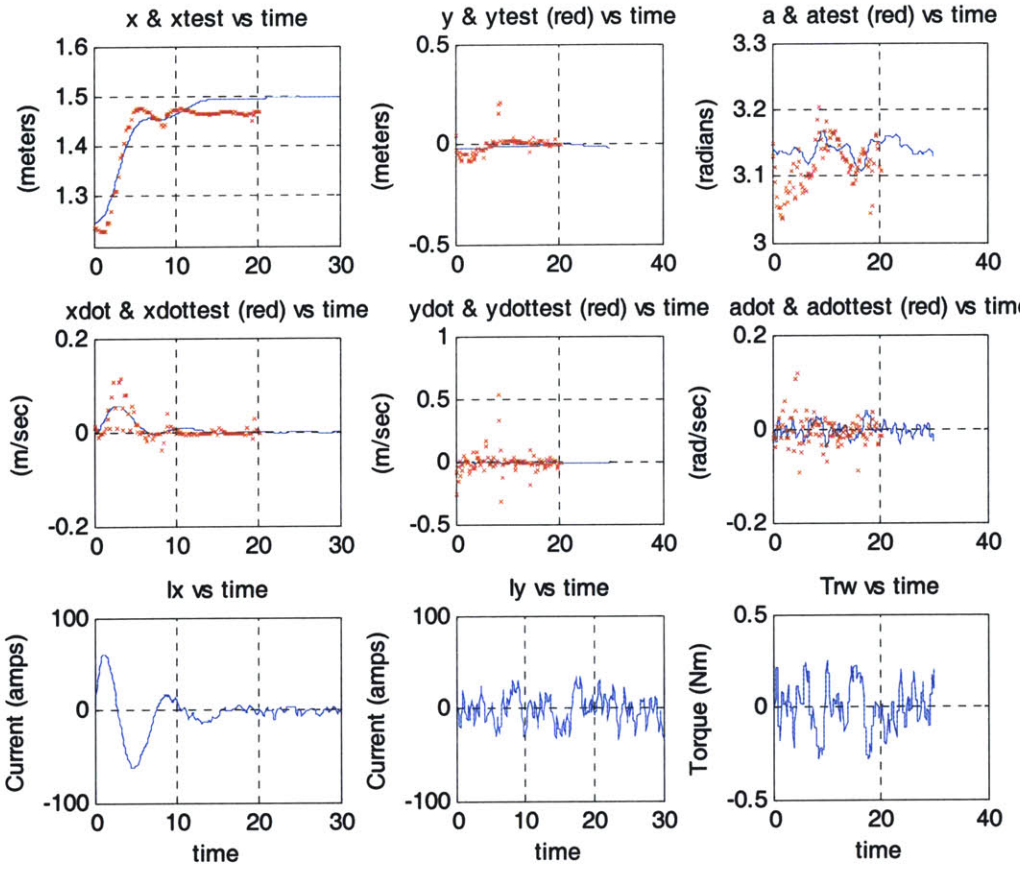

Figure 6.17: Step Response in x, Expensive Control Modified, Modified Simulation

The simulation results shown in Figure 6.17 do not predict any overshoot, and match the experimental results very closely, aside from the steady-state error. The data in Figure 6.18 lets us investigate the effect of adding a slope in the table to our model.

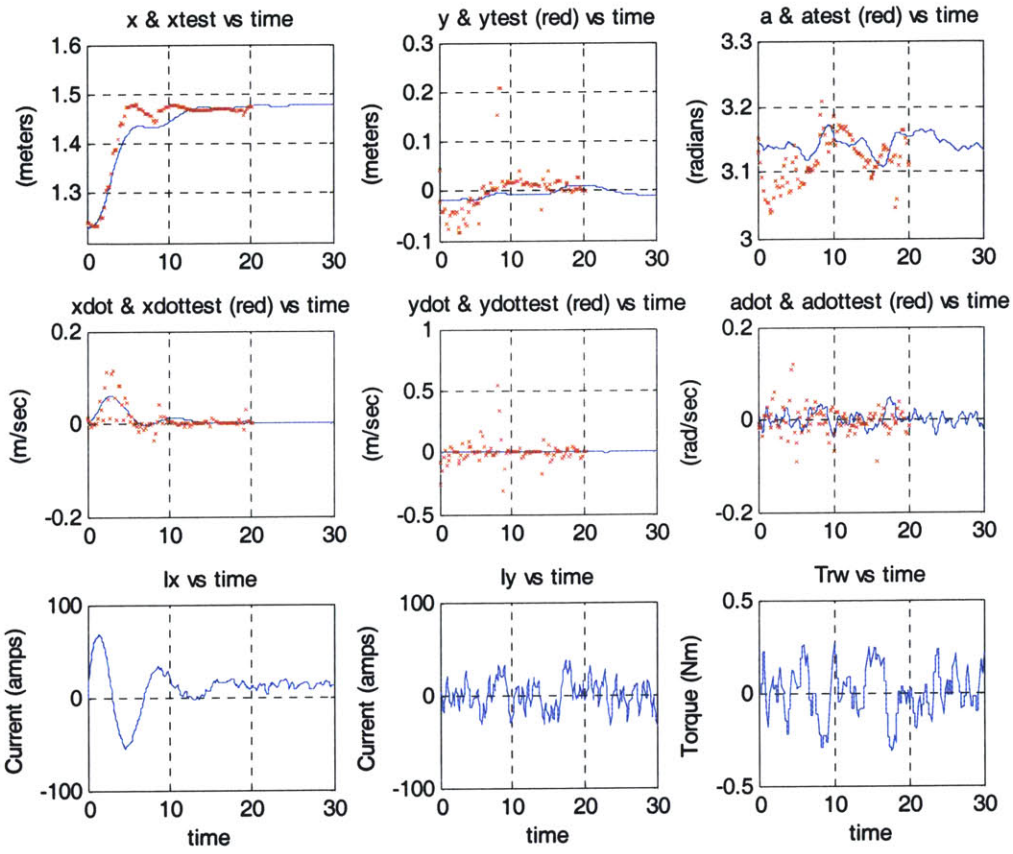

Figure 6.18: Step Response in x, Expensive Control Modified, Modified Sim with Table Slope

The simulation predictions with a slanted table do not match the initial rise as closely, but they do reach the same steady state as the actual vehicle did. We have focused most of our evaluation of the controllers developed for the EMFF testbed on examining the step response as the vehicles repel each other. This behavior was emphasized because the vehicles experience more force when close together than the linearized model expects. It is important to evaluate how the system responds when experiencing more force than expected while repelling the other vehicle. If the system pushed too hard, the moving vehicle could reach a velocity that causes it to escape from the influence of the magnetic field of the stationary vehicle.

However, tests were also conducted giving the system a step input from a location farther away from the nominal position. Figure 6.19 shows what the modified simulation

predicts will happen when the vehicle has initial position of 1.75 meters compared with what actually happened using the modified expensive control.

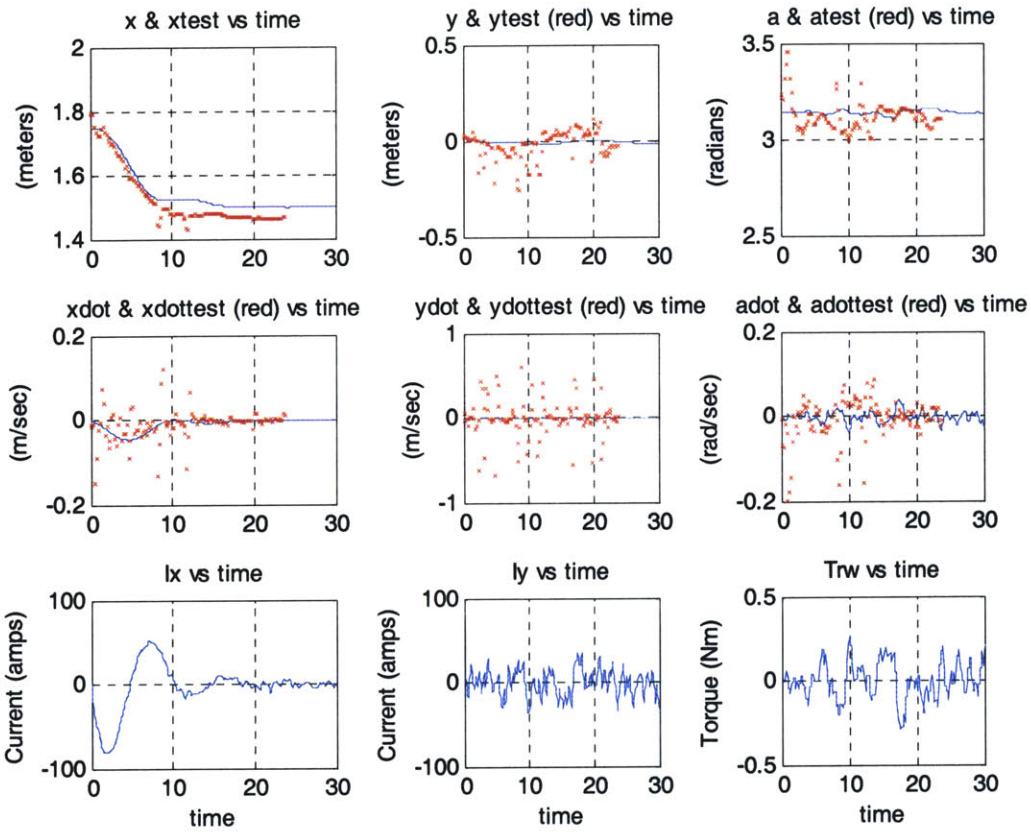

Figure 6.19: Attractive Step Response in x, Expensive Control Modified, Modified Sim

The expected response is very close to the measure experimental data. Again we see the effect of a slant in the table causing the vehicle to reach a position slightly smaller than the nominal position. Figure 6.20 shows the effect of adding a slant to the simulation model.

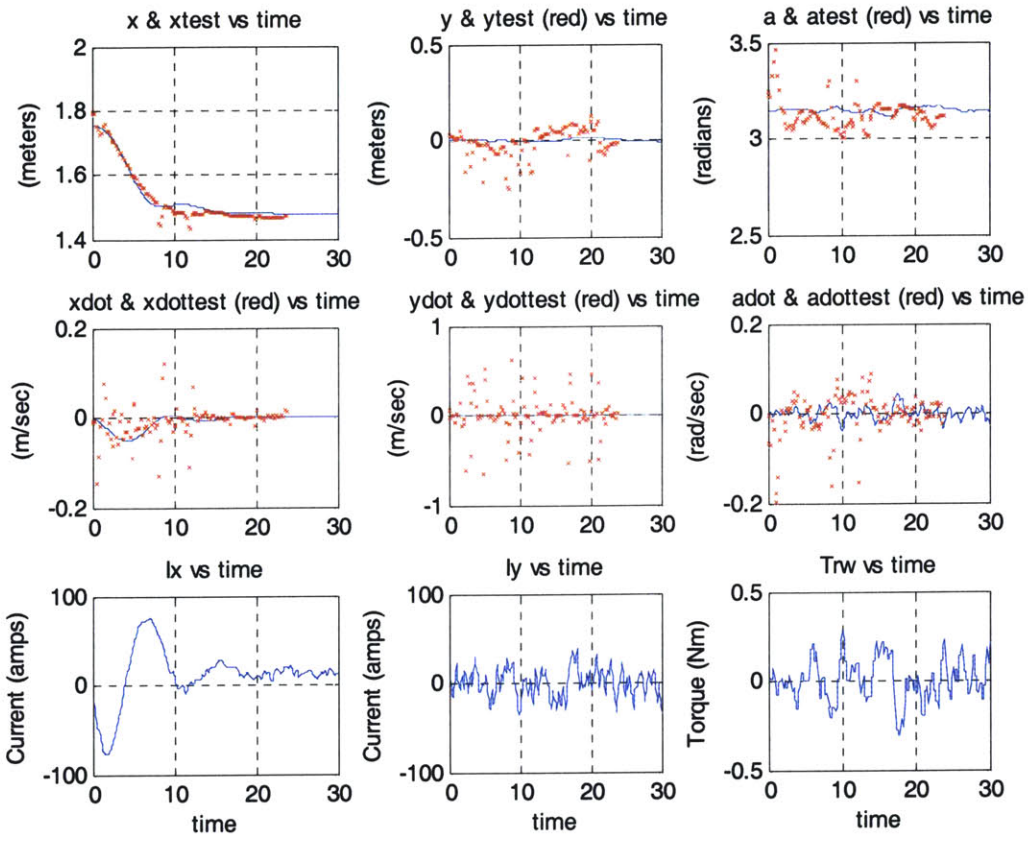

Figure 6.20: Attractive Step Response in x, Exp. Control Mod, Mod Sim with Table Slope

The response of the actual vehicle is almost identical to the predicted response from the simulation. This result gives confidence to the accuracy of the modified model to predict the dynamics of a step input in both repelling and attracting the moving vehicle.

The comparison of the modified simulation to the experimental results suggests that slowing the response of the commanded current in the coils made the simulation of the testbed dynamics much more accurate. The modified model can now give important information for control development in the future.

Chapter 7

Conclusions

7.1 Thesis Summary

This thesis began by motivating the research of implementing formation flight control using electromagnetic interactions between vehicles. The advantages of formation spacecraft flight and propellant free actuation were discussed. We also highlighted the enabling technology of superconducting wire to produce powerful electromagnets and a brief description of the Space Systems Lab's efforts to prove this concept using experimental hardware was given.

Chapter Two summarized the previous work done to provide thermal control for the superconducting wires and to develop control algorithms for electromagnetic actuation. The problems encountered with the first design of the thermal and avionics systems were described to provide motivation for their redesign. We also looked at the dynamic modeling and control work done by Dr. Laila Elias for a 3-dimensional EMFF system. Her work in finding that the EMFF system is indeed controllable provided the basis for the control development done for the 2-D testbed.

In Chapter Three we looked at the most recent efforts to provide effective thermal control for the superconducting wire coils used to create electromagnets. The rationale was provided for the choice of copper for the thermal containment system and the tests conducted to validate its use. We then presented the new thermal system, which was designed to provide more reliable containment of liquid nitrogen and more secure structural integrity. The process of developing the simple, yet effective pressure

regulator was also explained. Finally, we investigated the problems encountered with the new thermal control design and the measures taken to fix them.

Chapter Four identified the characteristics of the subsystems of EMFF used in implementing control of the moving vehicle. The specifications of the components of the avionics system were given and an explanation of hardware and procedure used by the metrology system was presented. The sensors and actuators used in controlling the system were also identified. Special attention was given to determining the frequency response of the superconducting coils to commanded current and to modeling the behavior of the reaction wheel. Accurate modeling of the reaction wheel enabled successful angular control of the vehicle. The physical properties of the EMFF system were also presented.

In Chapter Five, magnetic field models were presented to calculate the forces and torques between vehicles. The general far-field model, which assumes that each coil can be approximated as a magnetic dipole, was simplified to the two-dimensional case. A more accurate, yet also more computationally intensive, near-field model was also developed for greater fidelity when the vehicles are within a few coil radii from each other. Feedback controllers were designed using the two field models. The dynamics were linearized about an operating point to develop gains for linear feedback control and the nonlinear far-field model was used to develop a nonlinear sliding mode controller. The fast execution time of the far field model was exploited to develop the linear and nonlinear controllers to follow a trajectory with little error. Using the measured parameter for the EMFF hardware, it was shown that the controllers were able to reject disturbances and follow trajectories in the more accurate near-field model. It was found that the nonlinear controller commands higher frequency and magnitude control outputs, but it has the advantage of working anywhere around the vehicle.

In Chapter Six we examined the experimental results from implementing the controllers developed in Chapter Five. The control algorithms made the behavior of the vehicles stable, but more oscillatory than expected. In order to simulate the conditions of the

controller on the moving vehicle, the computer simulation was given the experimental metrology data and physical parameters were varied until the behavior of the simulation matched that of the experiment. This process yielded a new simulation model that has a slower response from commanded current to magnetic field than expected. It is possible that this delay is caused by mismodeling of the superconducting coil or by interference of metal objects around the testbed. The new simulation developed using experimental data predicts behavior very close to what was measured in experiments using the EMFF hardware.

7.2 Conclusions

7.2.1 Success of Thermal Design

The upgraded thermal control system has shown significantly improved performance over the previous design. The copper containment system withstands the thermal cycling imposed by frequent filling of liquid nitrogen and is easily repaired or modified with a soldering iron. The pressure regulator is able to keep the superconducting coils submerged in liquid nitrogen for the duration of a test. The tank holds enough liquid nitrogen to provide over twenty minutes of cooling and is easily refilled. The increased robustness of the test hardware has allowed more frequent and successful experiments to be conducted.

7.2.2 Comparison of Control Models

Three types of controllers were developed in this thesis. The linear controller based on the far field model of dynamics was useful in determining the state and control weightings for developing optimal control using the far field model for simulation. However, its performance declined when used in the near field simulation. The linear controller based on the near field model gave better results in the near field simulation and was used to implement control on the testbed as well. It was found that the controller developed for trajectory following used gains that saturated the current command, so control cost was increased in developing the optimal controller. The original linear controller enabled the EMFF vehicles to control position in a stable manner, with low

damping. A modified controller was developed that increased the gain on velocity error. This linear controller based on near field dynamics gave the best performance in disturbance rejection on the testbed. The nonlinear controller gave good results in the original simulation, but relies on the ability to change the magnetic field very rapidly. This controller did not perform well on the testbed because the dynamics of the changing the magnetic field were found to be much slower than originally estimated.

7.3 Recommendations

It was found that the dynamic model based on the physical parameters that were measured in system identification did not exactly match the dynamics of the actual testbed. Future work should investigate further where these discrepancies come from. The estimator should be improved to smooth out the data received from the metrology system. It would also be advantageous to improve the quality of the information the metrology system gives by adding sensors, such as accelerometers, or by improving the quality of the hardware.

The source of the delay found in fitting the dynamic model to the experimental data should be determined. Every coil should be tested to find its frequency response to commanded current. If the coil is found to have a pole higher than the one found in determining the modified model, then the interference of the table should be investigated. Tests should be conducted on a flat floor that does not contain ferromagnetic materials in order to see if the delay is present in those conditions as well.

The modified dynamics model presents opportunities to develop complex control using simulations that should predict the behavior of the testbed. The higher accuracy model does not only help with the evaluation of controllers, but can also be used in designing controllers. An extra state can be introduced for each coil to integrate the known pole into the dynamics model. The controller can then be designed for the plant including this new dynamic effect.

Further developments to the controller should include gain scheduling techniques using the stable controllers found in this thesis, but developed at different operating positions and attitudes. This method will use angular feedback to capture the effects of the rotating vehicle on magnetic forces and torques. Finally, the stationary vehicle should be equipped with air pucks and control algorithms should be developed for two moving vehicles.

APPENDIX A

This appendix contains the impulse response of the EMFF testbed using the modified expensive control gains. The x position returns to nominal position in little over five seconds.

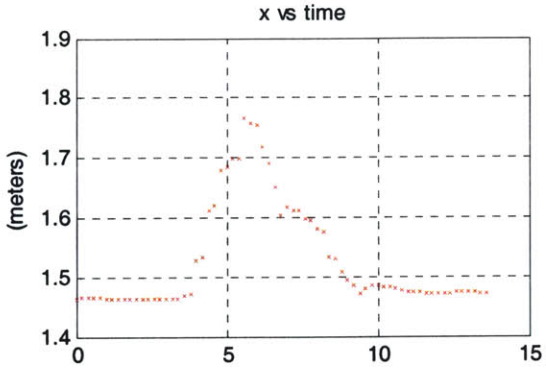

Figure A.1: x Position Impulse Response in x, Expensive Control Modified

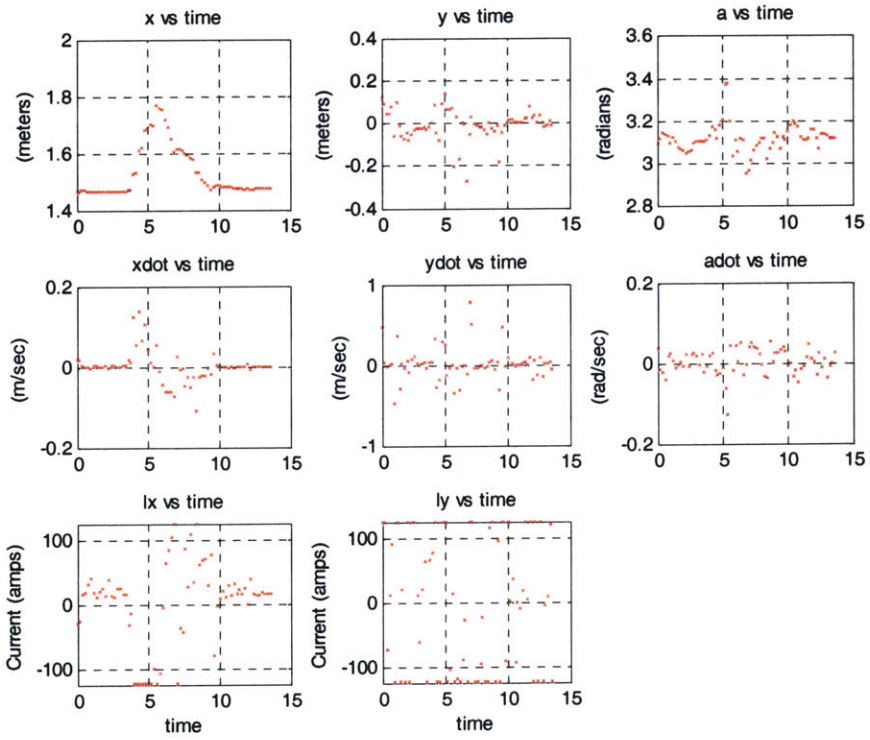

Figure A.2: Impulse Response in x, Expensive Control Modified

The response in y position to an impulse returns to nominal in about 10 seconds and then oscillates about the nominal position. The quality of the y position information given by the metrology system is quite low. Despite many jumps to bad data points the system seems to respond well.

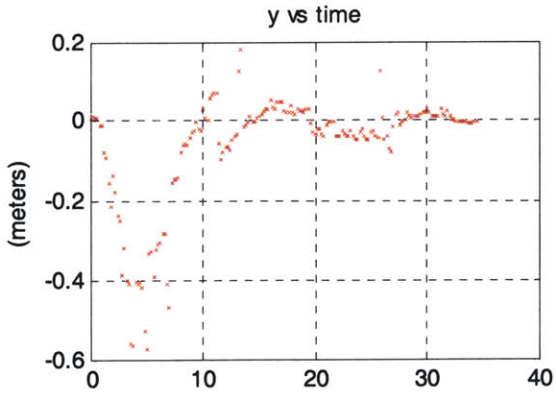

Figure A.3: y Position Impulse Response in y, Expensive Control Modified

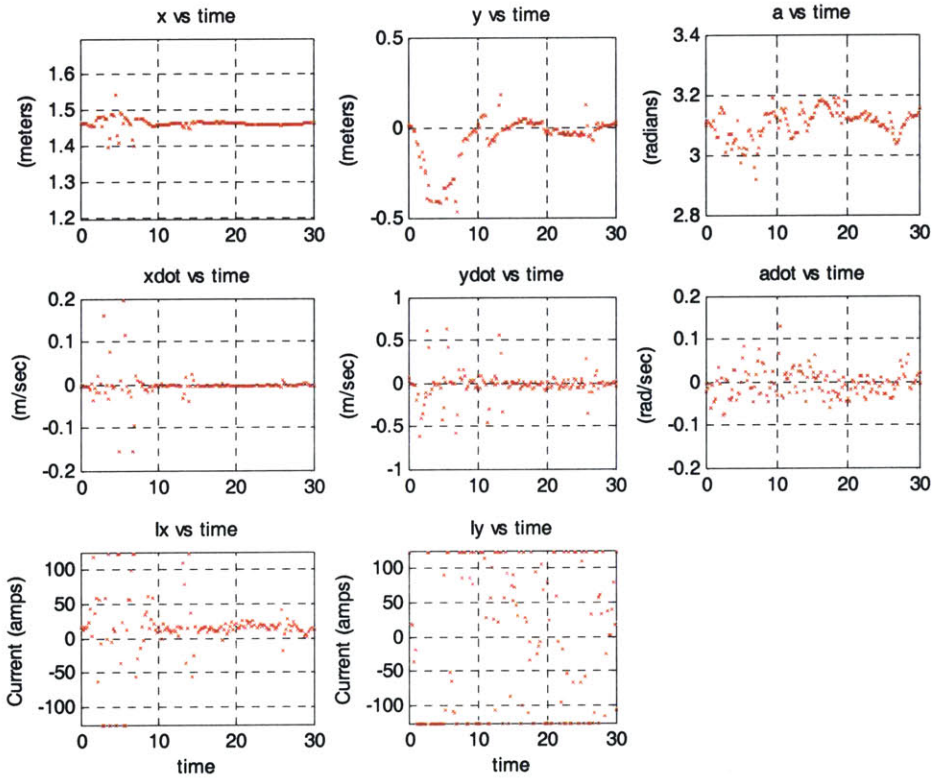

Figure A.4: Impulse Response in y, Expensive Control Modified

APPENDIX B

This appendix contains plots of the model fitting procedure that was used to find the correct physical parameters for simulating the testbed.

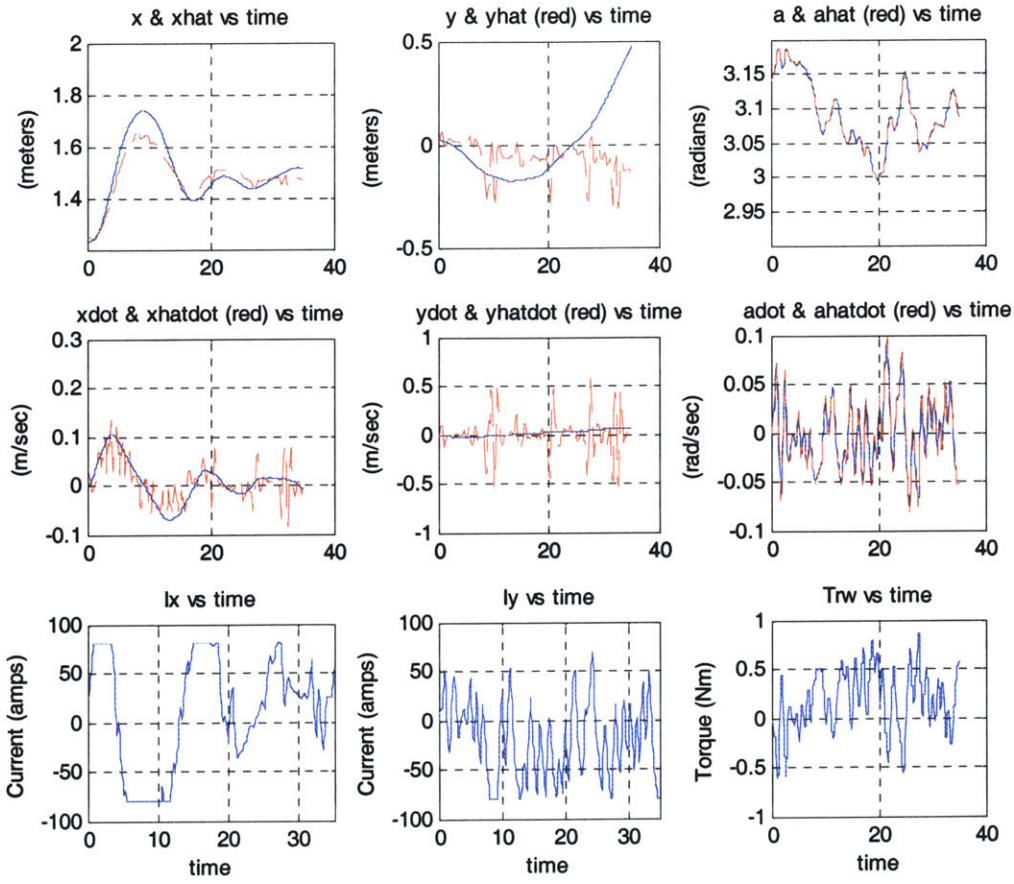

Figure B.5: Model Fitted to Step Response in x using Cheap Control Original

Figure B.5 shows the results of running the simulation with the best fit parameters that it gave as described in the Model Fitting section. This run is based on a pole location of 1.1 rad/sec and a near field scaling factor of 1. Since we determined that a pole at 0.8 rad/sec fits most of the data best, this test was run again using this pole location. The results

shown in Figure B.6 show that changing the pole by this small amount does not greatly decrease the accuracy of the fit.

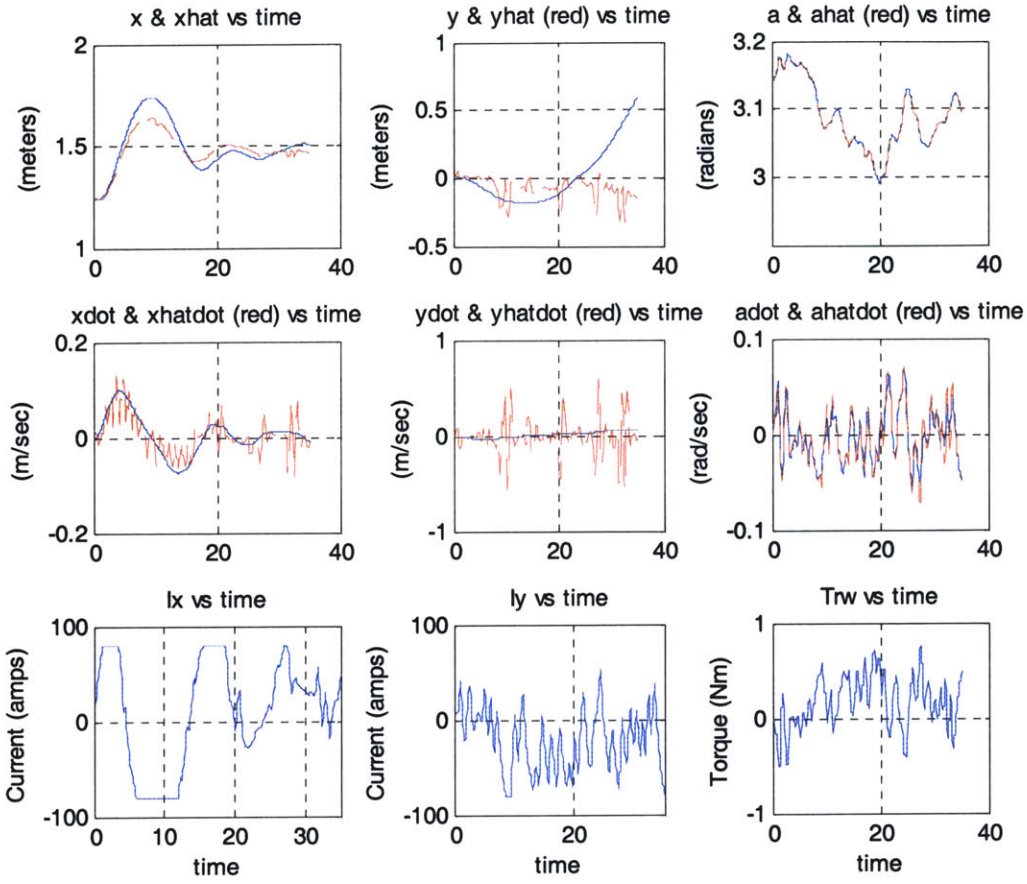

Figure B.6: Modified Model Fitted to Step Response in x using Cheap Control Original

Next, the data from the original run using expensive control is shown with its fitted model.

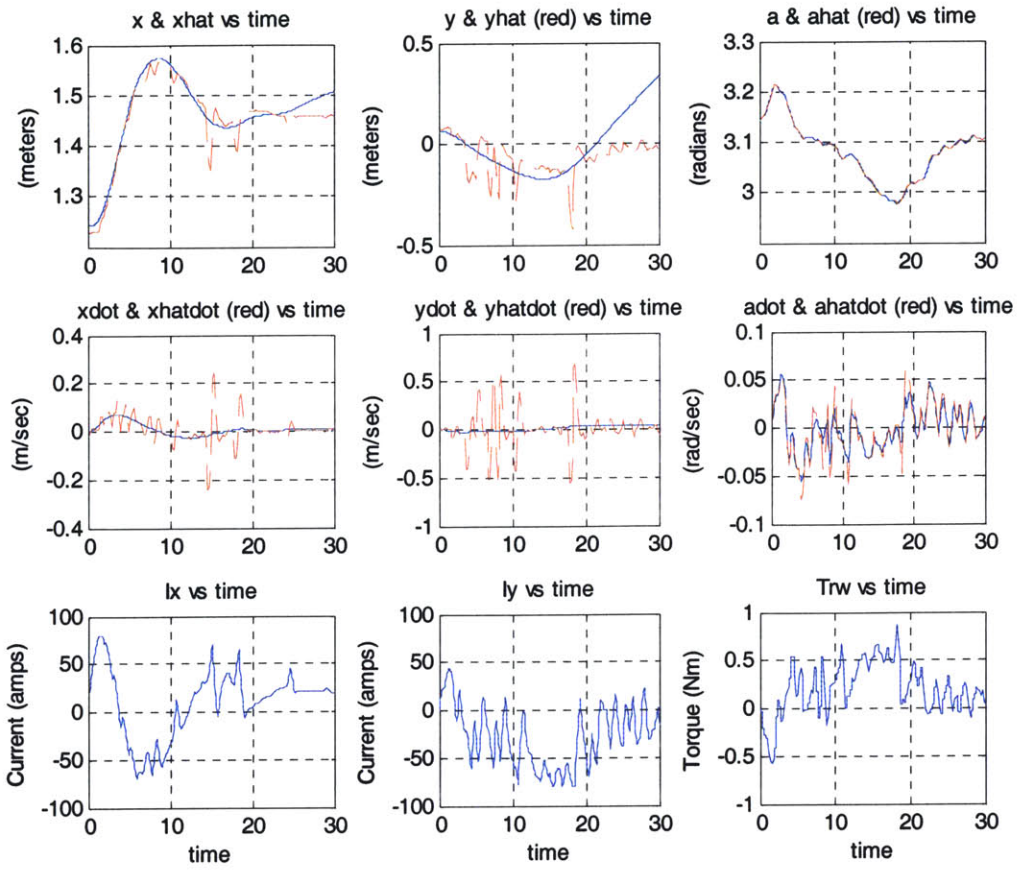

Figure B.7: Model Fitted to Step Response in x using Expensive Control Original

Figure B.7 shows the best fit model results, using the experimental metrology data as an input to the simulation. This test gave best results with a pole at 0.8 rad/sec and a near field scaling factor of 0.85. Since most sets of data implied that the true pole was at 0.8 rad/sec, but the scaling factor was 1, the same test was run assuming these values. The results are shown in Figure B.8 and one can notice that the fit is only slightly less accurate than the best fit results.

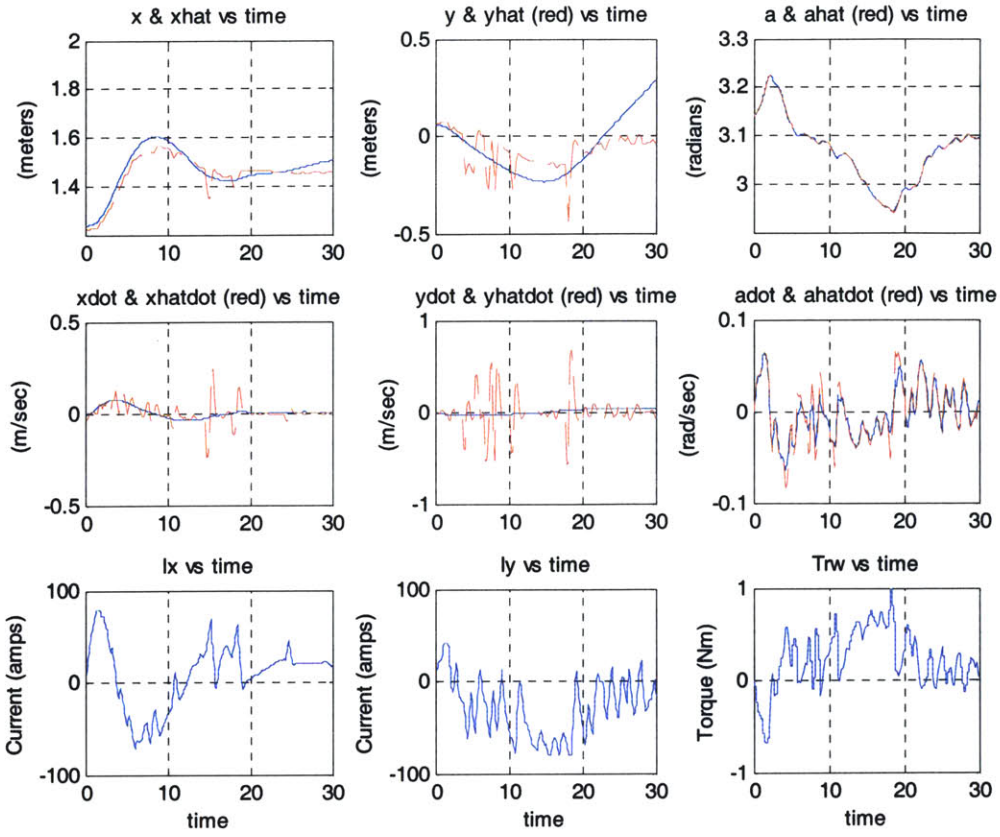

Figure B.8: Modified Model Fitted to Step Response in x using Expensive Control Original

The results for the test using modified cheap control were given in the main text of the thesis, so following in Figure B.9 are the results for modified expensive control.

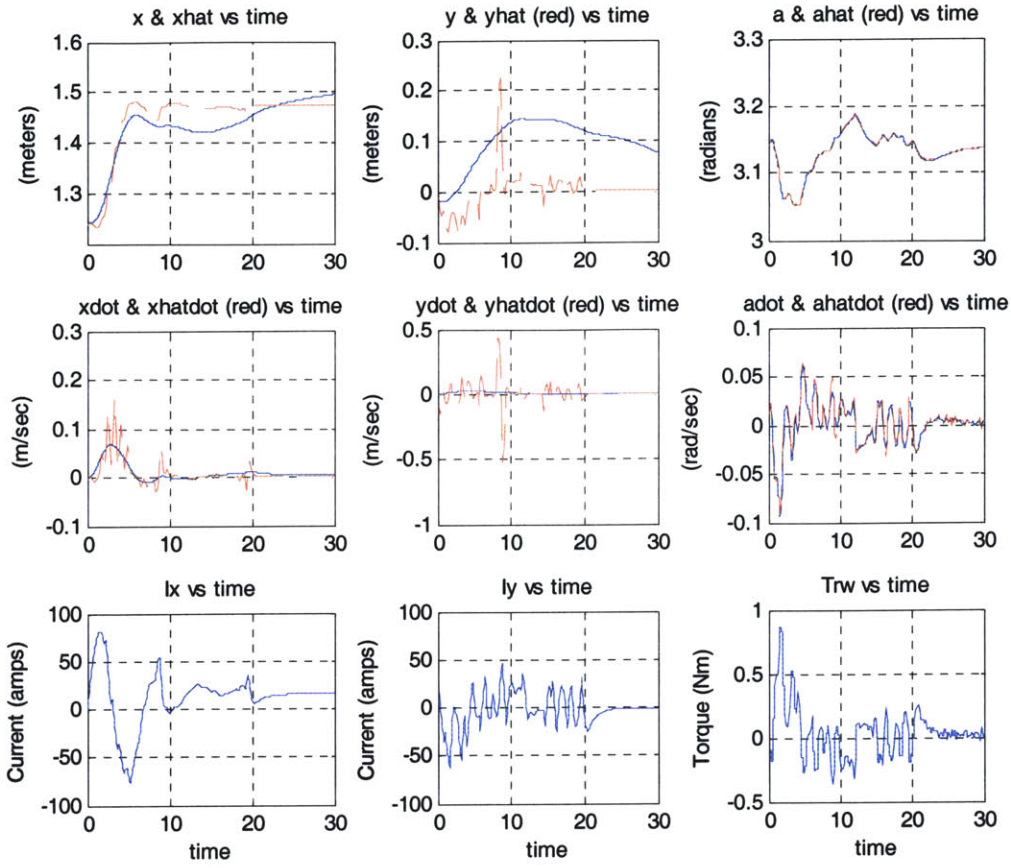

Figure B.9: Model Fitted to Step Response in x using Expensive Control Modified

Fitting the model to the modified expensive control metrology information yielded a pole at 0.8 rad/sec and a near field scaling factor of unity. These parameters were the ones used to update the dynamics model of the testbed to be used in simulation.

REFERENCES

[1] Bauer, Frank H., Hartman, Kate, How, Jonathan P., Bristow, John, Weidow, David, and Frank Busse, *Enabling Spacecraft Formation Flying through Spaceborne GPS and Enhanced Automation Technologies*, ION GPS-99, Nashville, TN, September 1999.

[2] Blackwood, Gary, Henry, Curt, Serabyn, Eugene, Dubovitsky, Serge, Aung, MiMi, and Steven M. Gunter, *Technology and Design of an Infrared Interferometer for the Terrestrial Planet Finder*, AIAA Conference SPACE 2003, Long Beach, California, 23-25 September 2003.

[3] Space Systems Laboratory, "SPHERES CDR Presentation," URL: http://ssl.mit.edu/spheres/library/SPHERES_CDR_Final.pdf [cited 20 March 2005]

[4] American superconductor, "Bi-2223 High Strength Wire," URL: http://www.amsuper.com/products/htsWire/index.html [cited 9 March 2005].

[5] EMFFORCE Design Document, MIT Space Systems Product Development Class, May 2003.

[6] Elias, Laila M, and Miller David W., *Dynamics of Multi-Body Space Interferometers Including Reaction Wheel Gyroscopic Stiffening Effects: Structurally Connected and Electromagnetic Formation Flying Architectures*, Ph.D. Thesis, Massachusetts Institute of Technology, SSL #5-04, March, 2004.

[7] Kwon, Daniel, and Miller, David W. *Electromagnetic Formation Flight of Satellite Arrays*, M.S. Thesis, Massachusetts Institute of Technology, SSL, February 2005.

[8] Franklin, Gene F., Powell, J. D., Emami-Naeini, A., *Feedback Control of Dynamic Systems,* Addison-Wesley, 1994.

[9] [17] Sedwick, Raymond. *Coordinatization of Ideal Magnetic Dipole-Dipole Interaction*, MIT Space Systems Lab Internal Document. August 9, 2002.

[10] This material was created by or adapted from material created by MIT faculty member, Jonathan How, Professor, Fall 2001. Copyright © 2001 Jonathan How.

[11] Slotine, J.-J. E., Li, W., *Applied Nonlinear Control,* Prentice-Hall, 1991.

[12] Van de Vegte, John, *Feedback Control Systems*, 3rd Edition, Prentice-Hall, 1994.